

University of Groningen

Visualization, classification and quantification of coronary atherosclerotic plaque using CT soft- and hardware phantom models

Kristanto, Wisnumurti

IMPORTANT NOTE: You are advised to consult the publisher's version (publisher's PDF) if you wish to cite from it. Please check the document version below.

Document Version

Publisher's PDF, also known as Version of record

Publication date:

2012

[Link to publication in University of Groningen/UMCG research database](#)

Citation for published version (APA):

Kristanto, W. (2012). Visualization, classification and quantification of coronary atherosclerotic plaque using CT soft- and hardware phantom models Groningen: s.n.

Copyright

Other than for strictly personal use, it is not permitted to download or to forward/distribute the text or part of it without the consent of the author(s) and/or copyright holder(s), unless the work is under an open content license (like Creative Commons).

Take-down policy

If you believe that this document breaches copyright please contact us providing details, and we will remove access to the work immediately and investigate your claim.

Downloaded from the University of Groningen/UMCG research database (Pure): <http://www.rug.nl/research/portal>. For technical reasons the number of authors shown on this cover page is limited to 10 maximum.

**Visualization, Classification and Quantification
of Coronary Atherosclerotic Plaque using CT
Soft- and Hardware Phantom Models**

Paranymphs: Astri Handayani
Volkan Tuncay

Cover image: The front cover shows a plush heart with a background of *Batik* ribbon. *Batik* is a traditional Indonesian patterned fabric, recently announced as an *Intangible Cultural Heritage* by UNESCO. The motif of the *Batik* ribbon here is to represent a coronary artery, with the red area as the coronary lumen and the adjacent relief as its plaque-burdened wall. The back cover shows the back side of the front cover, but with a “motion artefact”-induced false stenosis on the “coronary artery”, hidden from the front view.

Financial supports by University of Groningen, Graduate School of Medicine Groningen (GUIDE), and Pie Medical Imaging, B.V. for publication of this thesis are gratefully acknowledged.

Wisnumurti Kristanto

Visualization, Classification and Quantification of Coronary Atherosclerotic Plaque using CT Soft- and Hardware Phantom Models

PhD thesis with a summary in Dutch

ISBN: 978-90-367-5728-7

Layout & cover: Wisnumurti Kristanto

Printing: Offpage

Copyright © 2012 Wisnumurti Kristanto

All rights reserved. No part of this publication may be reproduced, stored in a retrieval system, or transmitted, in any form or by any means, electronic, mechanical, photocopying, recording, or otherwise, without the prior written permission of the publisher.



rijksuniversiteit
groningen

Visualization, Classification and Quantification of Coronary Atherosclerotic Plaque using CT Soft- and Hardware Phantom Models

Proefschrift

ter verkrijging van het doctoraat in de
Medische Wetenschappen
aan de Rijksuniversiteit Groningen
op gezag van de
Rector Magnificus, dr. E. Sterken,
in het openbaar te verdedigen op
maandag 1 oktober 2012
om 12.45 uur

door

Wisnumurti Kristanto

geboren op 5 mei 1979
te Surabaya, Indonesia

Promotor : Prof. dr. M. Oudkerk

Copromotor : Dr. ir. P.M.A. van Ooijen

Beoordelingscommissie : Prof. dr. ir. J.H.C. Reiber
Prof. dr. J.E. Wildberger
Prof. dr. ir. C.H. Slump

For Babe, Mama, Yuli, and Joshua

Contents

Chapter 1:	Introduction	1
	<i>Partly excerpted from Imaging in Medicine, 2010, vol. 2, no. 4, pp. 459-474</i>	
Chapter 2:	Quantitative image analysis for the detection of motion artefacts in coronary artery computed tomography	15
	<i>International Journal of Cardiovascular Imaging, 2010, vol. 26, no. 1, pp. 77-87</i>	
Chapter 3:	Small calcified coronary atherosclerotic plaque simulation model: Minimal size and attenuation detectable by 64-MDCT and microCT	31
	<i>International Journal of Cardiovascular Imaging, 2011, vol 28, no 4, pp 843-853</i>	
Chapter 4:	A systematic review and hierarchical classification of HU-based atherosclerotic plaque characterization criteria	49
	<i>Manuscript submitted</i>	
Chapter 5:	Non-calcified coronary atherosclerotic plaque visualization on CT: Effects of contrast-enhancement and lipid-content fractions	75
	<i>Manuscript submitted</i>	
Chapter 6:	Non-calcified coronary atherosclerotic plaque visualization on CT: Correction of lumen contrast-enhancement influence	95
	<i>Manuscript in preparation</i>	
Chapter 7:	Summary	111
Chapter 8:	Samenvatting	115
Chapter 9:	Acknowledgement	121
Chapter 10:	Curriculum vitae	125
Chapter 11:	List of publications	127

Chapter 1

Introduction

Partly excerpted from
Imaging in Medicine, 2010, vol. 2, no. 4, pp. 459-474
P.M.A. van Ooijen, G.J. de Jonge, W. Kristanto, A. Handayani, V. Tuncay,
and M. Oudkerk

Coronary artery disease

Coronary arteries are the blood vessels that supply oxygen- and nutrient-rich blood to the myocardium in order to keep it functional. Coronary artery disease (CAD) is a disease that reduces the function of the coronaries, caused by a build up of plaque in the coronary wall which eventually narrows the lumen in a gradual manner or acutely promotes blood clotting; either way will obstruct the blood flow to the myocardium and potentially lead to myocardial infarction. In western world, CAD became the leading cause of death [1]. In the Netherlands alone, 40.868 persons died of cardiovascular disease in 2008. Among those, 11.387 cases were ischemic heart disease of which 7.792 were caused by an acute heart infarct [2].

Atherosclerotic plaque progression

As described by the American Heart Association, an atherosclerotic plaque progresses in 6 types. The first three types are considered an early stage of atherosclerosis, where small groups of macrophages cells containing lipid droplets start to form within the vessel wall which then adaptively thickens (type I), and then the lipid containing macrophage cells start to proliferate, often forming fatty streaks (type II), and finally the lipid droplets start to form extracellularly (type III) [3].

The advance stage of atherosclerotic plaque is marked by the accumulation of lipid droplets forming a lipid core (type IV). The subsequent stage of the plaque progression is the growth of new fibrous tissue (type V), which may be accompanied by the presence of lipid core (type Va), calcification (type Vb) or mostly fibrotic (type Vc). The lesion may grow into a complicated lesion (type VI) by developing fissures (type VIa), hematoma or haemorrhage (type VIb), thrombus (type VIc), or all three features (type VIabc) [4].

Early visualization of atherosclerotic plaque

To be able to determine the severity and the stage of CAD, a reliable visualization and quantification of the atherosclerotic plaque is needed. Only then, a proper treatment can be determined in order to prevent or delay the progress of the disease.

Starting from type V, the progression of plaque often forces the vessel wall inward narrowing the lumen [4]. As the plaque grows further, the lumen can be severely narrowed to the point where it can not adequately supply the blood to the myocardium. X-ray angiography had been regarded as the gold standard imaging modality to quantify the severity of the lumen narrowing. However, it may fail to thoroughly quantify the narrowing due to its two dimensional projection. An incorrect projection angle can lead to foreshortening visualization of vessel. A lesion which should have been visible at one projection might not be visible at another projection.

However, not all plaque progression leads to narrowing of the lumen (negative remodelling). In fact, negative remodelling is associated with stable lesions and positive remodelling with unstable lesions [5]. Until a certain stage, the coronary undergoes a compensatory response to the plaque build up by growing outward causing a positive remodelling, while preserving lumen opening [6]. Moreover, plaque showing positive remodelling has been shown to contain more lipid than the ones showing negative remodelling [7]. It has been suggested that the plaque component and morphology is an important determinant of the disease severity. Three types of plaques are associated with acute coronary syndrome, i.e. plaque rupture, plaque erosion, and calcified nodule, with the plaque rupture as the most frequent [8]. X-ray angiography is limited to visualizing the coronary lumen. Even though it has also been shown that visualize the plaque surface morphology of a complex plaque, which has been associated with plaque rupture [9] and thrombus [10], x-ray angiography can not visualize the plaque itself. Intra vascular ultrasound (IVUS) has been regarded as the gold standard modality to visualize plaque component and morphology in vivo. However, IVUS is limited in not being able to reach the small vessels due to the fact that it is catheter based.

Both X-ray angiography and IVUS are invasive modalities which carries certain risks[11, 12] and certain level of discomfort to the patients. For these reasons, a non-invasive imaging modality is highly preferred to visualize coronary atherosclerotic plaque.

Computed tomography

Computed tomography (CT) makes use of multiple x-ray projections through patient's body to make a tomographic (cross section) of patient's body. CT was invented by Sir Godfrey Hounsfield in the 1970s, initially used for head scanning. The first generation of CT took hours to obtain a single slice thick image. After its introduction, CT showed a gradual technical development. The past decade, multi detector-row CT (MDCT) advance more rapidly resulting in the ability to obtain multiple slices at sub-millimeter resolution in a fraction of a second, enabling visualization of small fast moving objects, like coronary arteries.

The CT image pixel value is defined in Hounsfield Unit (HU) and it offers an advantage that is unique to CT as it is calibrated so the air will be -1000 HU value and water will be 0 HU. With this calibration, CT provides a possibility to characterize a tissue based on its HU value.

Coronary CT evaluation

(excerpted and adapted from van Ooijen, et al. [13])

Having the inherent technical advantages in image acquisition does not directly grant CT the ability to properly examine and visualize coronary arteries and atherosclerotic plaques. Further processing of the acquired images need to be performed in order to bring

out the useful information for the clinician to the fullest. A powerful software environment exhibiting powerful post-processing techniques is needed to enhance, localize, and analyze the images in order to produce meaningful information.

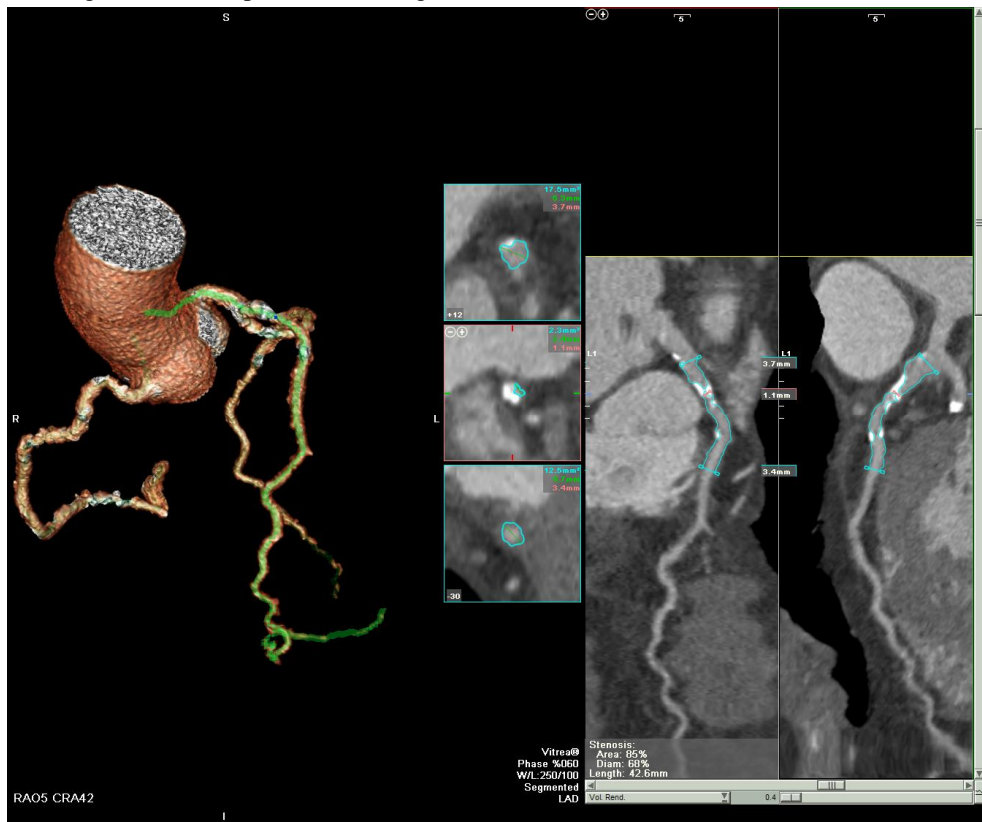


Figure 1-1. Automatic coronary stenosis measurement over a user defined part of the Left Anterior Descending artery.

Coronary stenosis measurement

Currently, the automatic segmentation of the coronary artery tree resulting in a display composed of curved multiplanar reformations (MPRs) along the centerline of the coronary arteries and orthogonal cross-sections is commonplace [14] and clinical implementation of advanced visualization is included in current guidelines [15] (figure 1-1). Reporting high sensitivity (89%) and specificity (100%), Busch *et al.* concluded that software supported CT-quantitative coronary angiography enables automatic quantitative analysis of significant coronary artery stenoses with area stenosis greater than 75% [16]. In many cases, the software will also identify the correct annotation of the coronary artery tree and will label the right coronary artery, left coronary artery and left circumflex branches automatically provided that the patient has a normal configuration of the coronary artery

tree. Maurer *et al.* showed in a survey that the vast majority of hospitals performing cardiac imaging using CT use these automatically generated curved MPRs for their interpretation [17].

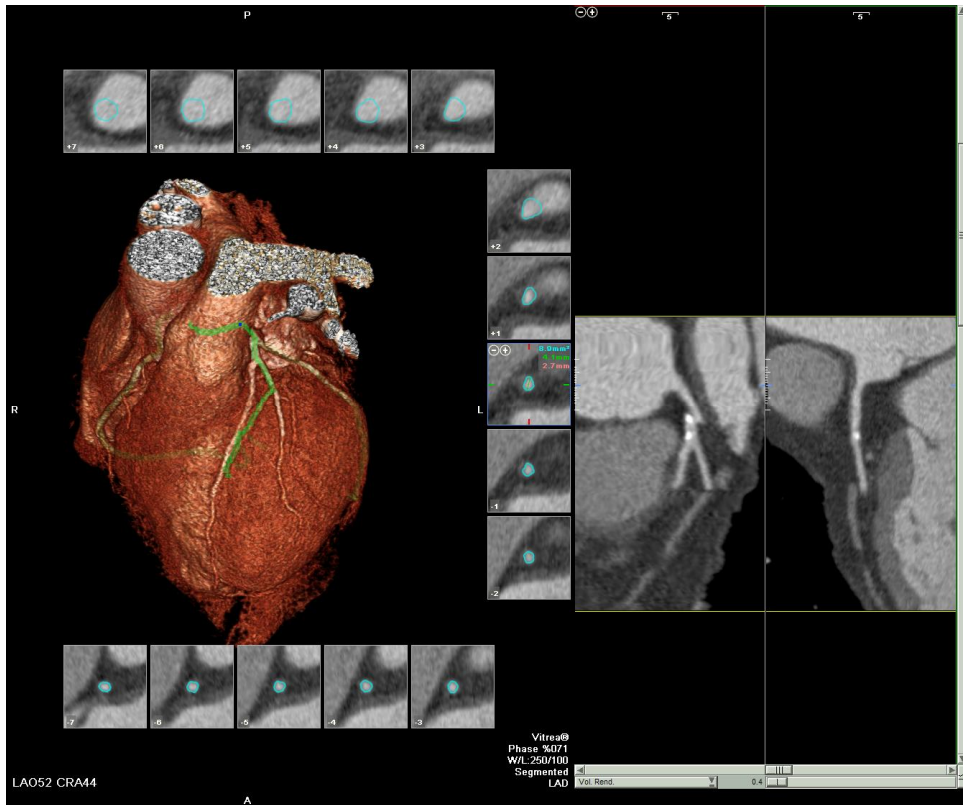


Figure 1-2. Example of missegmentation with the segmentation jumping from the First Diagonal of the Left Anterior Descending to the vein crossing over it.

However, reliability of the results of these automatically generated curved MPRs heavily depends on the algorithm used to extract the centerline of the artery and the amount of user interaction required for the segmentation [18] (figure 1-2). Furthermore, Dijkers *et al.* showed in a phantom study that manual stenosis measurements are significantly more accurate than automatic measurements, indicating that manual adjustments are still essential for the non-invasive assessment of coronary artery stenosis [19]. A more general approach promoted by other authors is to use axial MDCT images in combination with the (automatic generated) multiplanar reconstructions [20]. Ferencik *et al.* tested various image processing methods to determine hemodynamically significant stenoses of the coronary arteries and found various accuracy levels ranging from 73% to 91% [21]. Based on their results, they stated that the evaluation of MDCT coronary angiography with interactive image display methods, especially interactive oblique MPRs, permits higher diagnostic

accuracy than evaluation of prerendered images (curved MPR, curved maximum intensity projection [MIP], or volume rendering [VR] images).

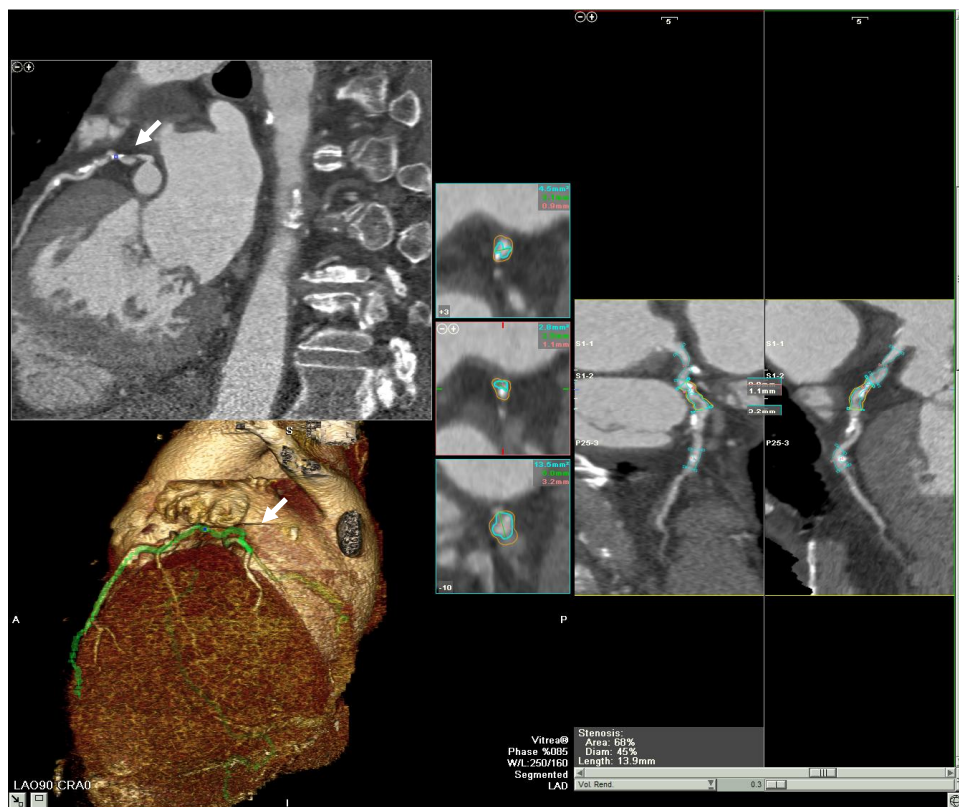


Figure 1-3. Example where a (significant) stenosis occurred at the same z-location as motion artefacts (white arrows). Careful steps must be taken in interpreting the validity of the finding.

The majority of reported studies support the use of multiple techniques in addition to the axial slices in an interactive fashion. The evaluation of MDCT coronary angiograms for the detection of coronary stenosis is frequently reported to be performed interactively on off-line workstations, by using a combination of transverse, MPR, MIP, and three-dimensional (3D) VR images [20, 22-29]. Some authors evaluated MDCT data sets initially by using MIP images or a prerendered slab of MPR images, and the findings were then confirmed by using MPR, curved MPR, or 3D VR images [30-32].

Regardless of the visualization technique used, careful steps must be taken to avoid the effect of motion artifacts, as they can lead to false stenoses [33] (figure 1-3). By retrospectively checking any plane parallel to the z-axis motion artifacts can be detected.

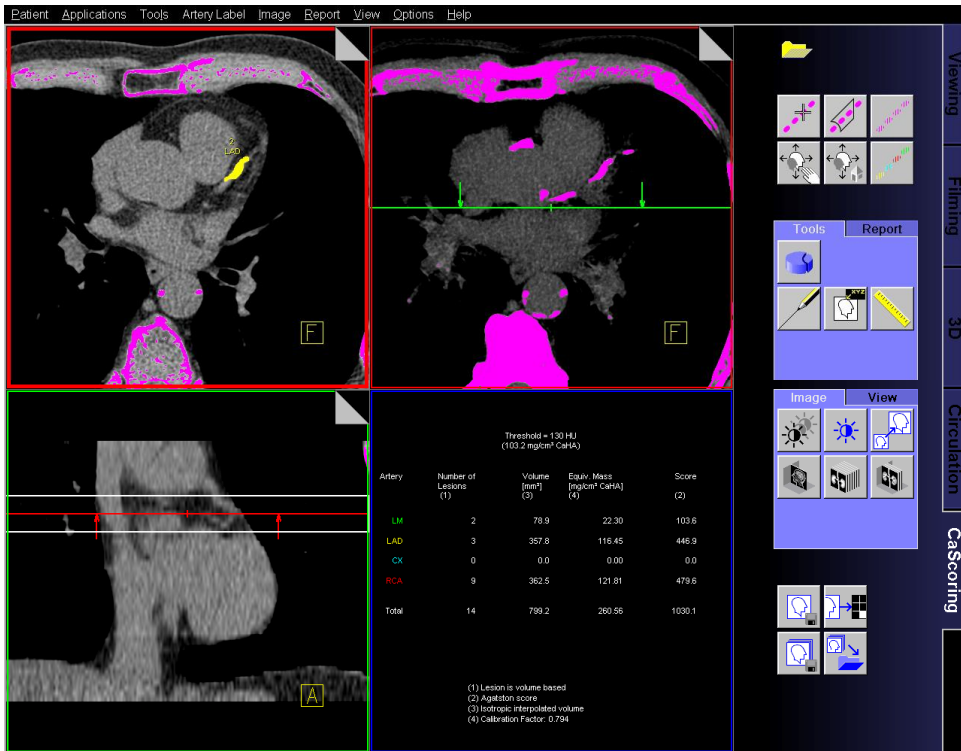


Figure 1-4. Non-enhanced cardiac CT dataset with at the top right marked calcified plaques in the trajectory of the left anterior descending artery. Color coding is used to color the regions above a certain threshold (typically 130 HU) after which the user indicates which regions are calcified regions inside a coronary artery and to which artery they belong

Coronary calcification

The amount of coronary calcification is considered to be a strong predictor of coronary events. [34] Current guidelines discuss the possible clinical application of coronary calcification quantification [35, 36].

Assessment of coronary calcification is performed on non-contrast-enhanced CT scans usually with a relatively large slice thickness of 3 mm. From the standard axial views of the heart, with high density structures which exceed certain threshold already marked by the software, coronary calcification can be manually selected and assigned to a vessel. The most commonly used threshold for the determination of coronary calcification is 130 HU [37].

Subsequently, the selected calcifications are automatically quantified based on the generally accepted scoring methods (Agatston, Volume or MASS) (figure 1-4).

However, the practical use of calcium scoring in serial studies for tracking the progression of disease is still hampered by the limited reproducibility of the calcium scores

currently in use both because of technical [38] and software issues [39]. Recently, Groen *et al.* proposed a way to reduce the susceptibility of calcium scoring to cardiac motion by adjusting the calcification threshold according to its maximum HU value, promoting an increase of accuracy of at least 10% [40].

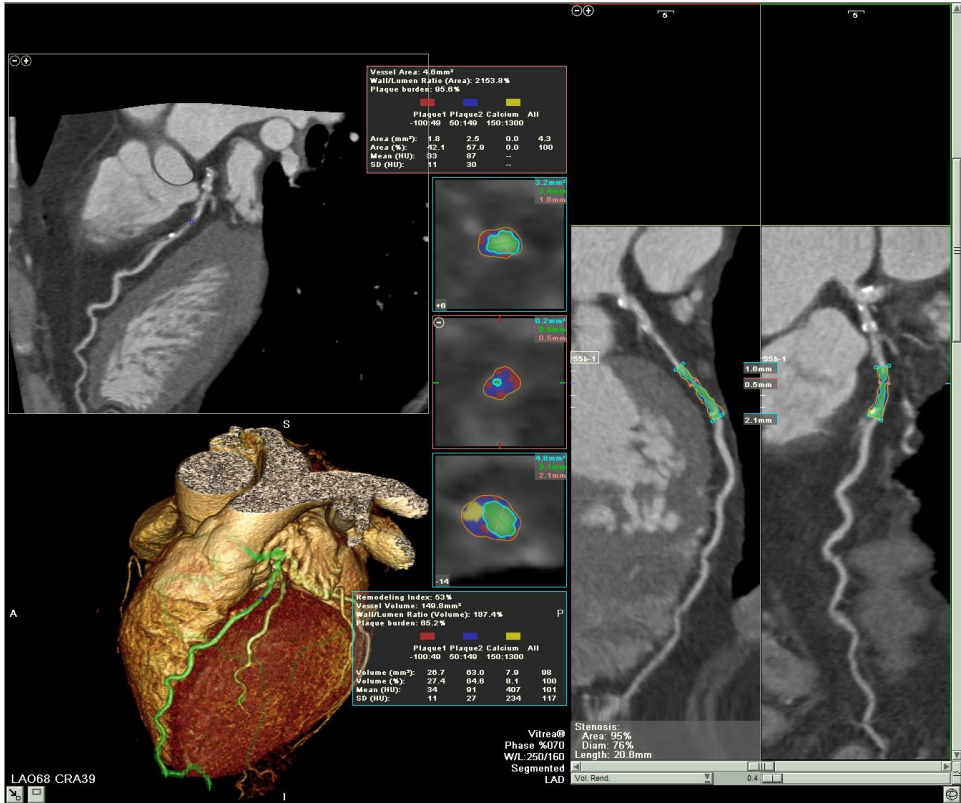


Figure 1-5. Automatic plaque morphology assessment. Box pointed by arrow 1 show the area and diameter stenosis grade at the most stenotic site, while boxes pointed by arrow 2 and 3 show plaque morphology at the most stenotic plaque cross-section and for the whole plaque volume, respectively

Analysis of plaque morphology

To analyze plaque morphology, MPRs orthogonal to the centerline of the (automatically segmented) coronary artery can be obtained resulting in a large number of cross-sections of the coronary artery for evaluation of stenotic and nonstenotic coronary atherosclerotic lesions [41]. The conventional way of analyzing plaque morphology is by manual visual evaluation. To assess maximum luminal narrowing, the optimal image display setting can be chosen on an individual basis, in general at a window between 600 and 900 HU and at a level between 40 and 250 HU. Structures with densities above the

adjacent vessel lumen are usually defined as calcified, and structures with densities below the vessel contrast as noncalcified plaques [42, 43]. Manual segmentation of outer vessel wall can also be done for assessment of vessel remodeling, as this parameter plays important role in determining plaque vulnerability [5]. The plaque composition can be determined by the mean HU value of manually placed regions of interest (ROI) at different areas inside the vessel wall. Of these ROIs, the mean HU value and standard deviation are then used to determine the plaque composition.

Currently, many software packages also provide an automatic determination of lumen and vessel borders in combination with color coding of certain ranges of HU values (figure 1-5). These ranges should then indicate the different types of plaque and result in an automatic determination of the volumetric measurement of each plaque type. Therefore, using this automated tool, a complete volumetric analysis of the plaque compositions and of the percentage vessel remodeling (remodeling index) can be obtained.

However, selection of the HU ranges should be made carefully as various claims are made by different authors about the HU values that correspond to certain types of plaques using intravascular ultrasound as the gold standard [43-45]. For example, Leber *et al.* [45] reported MDCT-derived density measurements within coronary lesions of 49 ± 22 HU for hypoechoic, 91 ± 22 HU for hyperechoic and 391 ± 156 HU for calcified plaques, while Carrascosa *et al.* [46] reported 71.5 ± 32.1 HU for soft and 116.3 ± 35.7 HU for fibrous, and 383.63 ± 186.1 HU for calcified plaques. They both reported these values to be significantly different.

Based on current reports, classification of coronary plaque into calcified and non-calcified plaque could be feasible, either by qualitative visual assessment, using a common threshold for calcification, or even using automatic vessel segmentation tools [47, 48]. However, sub classification between the different non-calcified plaque types, such as lipid and fibrous plaque, seems difficult owing to the variety in reported cut-off values and the overlap in HU ranges. Furthermore, various factors, such as the reconstruction kernel and the attenuation level of the contrast enhanced blood in the arteries, have been reported to significantly influence the HU value of plaques used for the determination of plaque composition [49, 50].

Purpose and outline

Despite having advanced technical developments, there are still limitations for CT in order to thoroughly visualize, analyze and quantify coronary arteries and atherosclerotic plaques. The purpose of this study is to investigate those limitations in order to provide more understanding in the field of coronary atherosclerosis visualization using MDCT.

The first topic is about the coronary lumen visualization. Despite the many success reports of CT in visualizing coronary tree due to its high subsecond spatial resolution, there

is still one inherent drawback, namely motion artefacts. The second chapter discusses the effect of motion artefact on coronary lumen visualization.

The second topic is about coronary calcification visualization. Despite the many success reports of CT ability in quantifying coronary calcifications and the sub-millimeter spatial resolution, there is a limitation on the size of calcification that can be detected by MDCT. The third chapter discusses about this in detail using a software simulation.

The third topic is about non-calcified coronary atherosclerotic plaque visualization. Many studies reported the ability of CT in characterizing non-calcified plaques by virtue of their HU values. However, the reported values vary considerably. The fourth chapter discusses a systematic analysis on those reported plaque-specific HU values. The fifth chapter discusses the influencing factors that may influence non-calcified coronary atherosclerotic plaque in detail in a software simulation. The sixth chapter discusses a newly developed correction algorithm for the most prominent influencing factor to non-calcified coronary atherosclerotic plaque visualization, i.e. lumen contrast-enhancement.

References

- [1] Heron MP, Smith BL. Deaths: leading causes for 2003. *Natl Vital Stat Rep* 2007; 55:1-92
- [2] Vaartjes I, van Dis I, Visseren FLJ, Bots ML (2010) Hart- en vaatziekten in Nederland, 2010. Cijfers over leefstijl- en risicofactoren, ziekte en sterfte. Nederlandse Hartstichting, Den Haag
- [3] Stary HC, Chandler AB, Glagov S, et al. A definition of initial, fatty streak, and intermediate lesions of atherosclerosis. A report from the Committee on Vascular Lesions of the Council on Arteriosclerosis, American Heart Association. *Circulation* 1994; 89:2462-78
- [4] Stary HC, Chandler AB, Dinsmore RE, et al. A definition of advanced types of atherosclerotic lesions and a histological classification of atherosclerosis. A report from the Committee on Vascular Lesions of the Council on Arteriosclerosis, American Heart Association. *Circulation* 1995; 92:1355-74
- [5] Schoenhagen P, Ziada KM, Kapadia SR, et al. Extent and direction of arterial remodeling in stable versus unstable coronary syndromes: an intravascular ultrasound study. *Circulation* 2000; 101:598
- [6] Glagov S, Weisenberg E, Zarins CK, Stankunavicius R, Kolettis GJ. Compensatory Enlargement of Human Atherosclerotic Coronary Arteries. *N Engl J Med* 1987; 316:1371-5
- [7] Varnava AM, Mills PG, Davies MJ. Relationship between coronary artery remodeling and plaque vulnerability. *Circulation* 2002; 105:939-43
- [8] Virmani R, Burke AP, Farb A, Kolodgie FD. Pathology of the vulnerable plaque. *J Am Coll Cardiol* 2006; 47:13-8

-
- [9] Rioufol G, Finet G, Ginon I, et al. Multiple atherosclerotic plaque rupture in acute coronary syndrome. *Circulation* 2002; 106:804-8
- [10] Alfonso F, Fernandez-Ortiz A, Goicolea J, et al. Angioscopic evaluation of angiographically complex coronary lesions. *American heart journal* 1997; 134:703-11
- [11] Wyman RM, Safian RD, Portway V, et al. Current complications of diagnostic and therapeutic cardiac catheterization. *Journal of the American College of Cardiology* 1988; 12:1400-6
- [12] De Bono D. Complications of diagnostic cardiac catheterisation: results from 34,041 patients in the United Kingdom confidential enquiry into cardiac catheter complications. The Joint Audit Committee of the British Cardiac Society and Royal College of Physicians of London. *British heart journal* 1993; 70:297-300
- [13] van Ooijen PMA, de Jonge GJ, Kristanto W, et al. Optimal postprocessing of images following cardiac examination using CT and MRI. *Imaging in Medicine* 2010; 2:459-74
- [14] Dewey M, Schnapauff D, Laule M, et al. Multislice CT coronary angiography: Evaluation of an automatic vessel detection tool. *Fortschr Rontgenstr* 2004; 176:478-83
- [15] Mark DB, Berman DS, Budoff MJ, et al. ACCF/ACR/AHA/NASCI/SAIP/SCAI/SCCT 2010 Expert Consensus Document on Coronary Computed Tomographic Angiography: A Report of the American College of Cardiology Foundation Task Force on Expert Consensus. *Circulation* 2010; 121:2509-43
- [16] Busch S, Johnson TR, Nikolaou K, et al. Visual and automatic grading of coronary artery stenoses with 64-slice CT angiography in reference to invasive angiography. *Eur Radiol* 2007; 17:1445-51
- [17] Maurer MH, Hamm B, Dewey M Survey regarding the clinical practice of cardiac CT in Germany: indications, scanning technique and reporting. Thieme, (2009): pp 1135-1143
- [18] Schaap M, Metz CT, van Walsum T, et al. Standardized evaluation methodology and reference database for evaluating coronary artery centerline extraction algorithms. *Medical Image Analysis* 2009; 13:701-14
- [19] Dikkers R, Willems TP, de Jonge GJ, et al. Accuracy of noninvasive coronary stenosis quantification of different commercially available dedicated software packages. *Journal of Computer Assisted Tomography* 2009; 33:505
- [20] Ropers D, Baum U, Pohle K, et al. Detection of coronary artery stenoses with thin-slice multi-detector row spiral computed tomography and multiplanar reconstruction. *Circulation* 2003; 107:664-6

- [21] Ferencik M, Ropers D, Abbara S, et al. Diagnostic Accuracy of Image Postprocessing Methods for the Detection of Coronary Artery Stenoses by Using Multidetector CT1. *Radiology* 2007; 243:696
- [22] Dewey M, Laule M, Krug L, et al. Multisegment and halfscan reconstruction of 16-slice computed tomography for detection of coronary artery stenoses. *Investigative radiology* 2004; 39:223
- [23] Hoffmann U, Moselewski F, Cury RC, et al. Predictive value of 16-slice multidetector spiral computed tomography to detect significant obstructive coronary artery disease in patients at high risk for coronary artery disease. *Circulation* 2004; 110:2638-43
- [24] Kuettner A, Beck T, Drosch T, et al. Diagnostic accuracy of noninvasive coronary imaging using 16-detector slice spiral computed tomography with 188 ms temporal resolution. *Journal of the American College of Cardiology* 2005; 45:123-7
- [25] Leber AW, Knez A, von Ziegler F, et al. Quantification of Obstructive and Nonobstructive Coronary Lesions by 64-Slice Computed Tomography:: A Comparative Study With Quantitative Coronary Angiography and Intravascular Ultrasound. *Journal of the American College of Cardiology* 2005; 46:147-54
- [26] Leschka S, Alkadhi H, Plass A, et al. Accuracy of MSCT coronary angiography with 64-slice technology: first experience. *European heart journal* 2005; 26:1482
- [27] Martuscelli E, Romagnoli A, D'Eliseo A, et al. Accuracy of thin-slice computed tomography in the detection of coronary stenoses. *European heart journal* 2004; 25:1043
- [28] Nieman K, Cademartiri F, Lemos PA, et al. Reliable noninvasive coronary angiography with fast submillimeter multislice spiral computed tomography. *Circulation* 2002; 106:2051-4
- [29] Raff GL, Gallagher MJ, O'Neill WW, Goldstein JA. Diagnostic accuracy of noninvasive coronary angiography using 64-slice spiral computed tomography. *Journal of the American College of Cardiology* 2005; 46:552-7
- [30] Mollet NR, Cademartiri F, Krestin GP, et al. Improved diagnostic accuracy with 16-row multi-slice computed tomography coronary angiography. *Journal of the American College of Cardiology* 2005; 45:128-32
- [31] Kefer J, Coche E, Legros G, et al. Head-to-head comparison of three-dimensional navigator-gated magnetic resonance imaging and 16-slice computed tomography to detect coronary artery stenosis in patients. *Journal of the American College of Cardiology* 2005; 46:92-100
- [32] Hoffmann MHK, Shi H, Schmitz BL, et al. Noninvasive coronary angiography with multislice computed tomography. *JAMA: the journal of the American Medical Association* 2005; 293:2471

-
- [33] Kristanto W, van Ooijen PM, Dijkers R, et al. Quantitative image analysis for the detection of motion artefacts in coronary artery computed tomography. *Int J Cardiovasc Imaging* 2010; 26:77-87
- [34] Arad Y, Goodman KJ, Roth M, Newstein D, Guerci AD. Coronary calcification, coronary disease risk factors, C-reactive protein, and atherosclerotic cardiovascular disease events the St. Francis Heart Study. *J Am Coll Cardiol* 2005; 46:158-65
- [35] Oudkerk M, Stillman AE, Halliburton SS, et al. Coronary artery calcium screening: current status and recommendations from the European Society of Cardiac Radiology and North American Society for Cardiovascular Imaging. *Int J Cardiovasc Imaging* 2008; 24:645-71
- [36] Oudkerk M, Stillman AE, Halliburton SS, et al. Coronary artery calcium screening: current status and recommendations from the European Society of Cardiac Radiology and North American Society for Cardiovascular Imaging. *Eur Radiol* 2008; 18:2785-807
- [37] Agatston AS, Janowitz WR, Hildner FJ, et al. Quantification of coronary artery calcium using ultrafast computed tomography. *J Am Coll Cardiol* 1990; 15:827-32
- [38] Naghavi M, Falk E, Hecht HS, et al. From vulnerable plaque to vulnerable patient--Part III: Executive summary of the Screening for Heart Attack Prevention and Education (SHAPE) Task Force report. *The American Journal of Cardiology* 2006; 98:2-15
- [39] van Ooijen PM, Vliegenthart R, Wittman JC, Oudkerk M. Influence of scoring parameter settings on Agatston and volume scores for coronary calcification. *Eur Radiol* 2005; 15:102-10
- [40] Groen JM, Dijkstra H, Greuter MJW, Oudkerk M. Threshold adjusted calcium scoring using CT is less susceptible to cardiac motion and more accurate. *Medical Physics* 2009; 36:438
- [41] Achenbach S, Ropers D, Hoffmann U, et al. Assessment of coronary remodeling in stenotic and nonstenotic coronary atherosclerotic lesions by multidetector spiral computed tomography. *Journal of the American College of Cardiology* 2004; 43:842-7
- [42] Leber AW, Knez A, White CW, et al. Composition of coronary atherosclerotic plaques in patients with acute myocardial infarction and stable angina pectoris determined by contrast-enhanced multislice computed tomography. *American Journal of Cardiology* 2003; 91:714-8
- [43] Schroeder S, Kopp AF, Baumbach A, et al. Noninvasive detection and evaluation of atherosclerotic coronary plaques with multislice computed tomography. *J Am Coll Cardiol* 2001; 37:1430-5
- [44] Cademartiri F, La Grutta L, Palumbo A, et al. Non-invasive visualization of coronary atherosclerosis: state-of-art. *Journal of Cardiovascular Medicine* 2007; 8:129

- [45] Leber AW, Knez A, Becker A, et al. Accuracy of multidetector spiral computed tomography in identifying and differentiating the composition of coronary atherosclerotic plaques A comparative study with intracoronary ultrasound. *J Am Coll Cardiol* 2004; 43:1241-7
- [46] Carrascosa PM, Capuñay CM, Garcia-Merletti P, Carrascosa J, Garcia MJ. Characterization of coronary atherosclerotic plaques by multidetector computed tomography. *Am J Cardiol* 2006; 97:598-602
- [47] Achenbach S, Moselewski F, Ropers D, et al. Detection of calcified and noncalcified coronary atherosclerotic plaque by contrast-enhanced, submillimeter multidetector spiral computed tomography a segment-based comparison with intravascular ultrasound. *Am Heart Assoc*, (2004): pp 14-17
- [48] Clouse ME, Sabir A, Yam CS, et al. Measuring noncalcified coronary atherosclerotic plaque using voxel analysis with MDCT angiography: a pilot clinical study. *American Journal of Roentgenology* 2008; 190:1553
- [49] Cademartiri F, Mollet NR, Runza G, et al. Influence of intracoronary attenuation on coronary plaque measurements using multislice computed tomography: observations in an ex vivo model of coronary computed tomography angiography. *Eur Radiol* 2005; 15:1426-31
- [50] Cademartiri F, La Grutta L, Runza G, et al. Influence of convolution filtering on coronary plaque attenuation values: observations in an ex vivo model of multislice computed tomography coronary angiography. *Eur Radiol* 2007; 17:1842-9

Chapter 2

Quantitative image analysis for the detection of motion artefacts in coronary artery computed tomography

International Journal of Cardiovascular Imaging, 2010, vol. 26, no. 1, pp. 77-87
**W. Kristanto, P.M.A. van Ooijen, R. Dijkers, M.J.W. Greuter, F. Zijlstra,
and M. Oudkerk**

Abstract

Multi detector-row CT (MDCT), the current preferred method for coronary artery disease assessment, is still affected by motion artefacts. To rule out motion artefacts, qualitative image analysis is usually performed. Our study aimed to develop a quantitative image analysis for motion artefacts detection as an added value to the qualitative analysis. An anthropomorphic moving heart phantom with adjustable heart-rate was scanned on 64-MDCT and dual-source-CT. A new software technique was developed which detected motion artefacts in the coronaries and also in the myocardium, where motion artefacts are more apparent; with direct association to the qualitative analysis. The new quantitative analysis managed to detect motion artefacts in phantom scans and relate them to artefact-induced vessel stenoses. Quantifying these artefacts at corresponding locations in the myocardium, artefact-induced vessel stenosis findings could be avoided. In conclusion, the quantitative analysis together with the qualitative analysis rules out artefact-induced stenosis.

Introduction

Coronary artery disease (CAD) is the leading cause of death in western countries [1, 2]. It can result in coronary vessels obstruction and eventually myocardial ischemia. Multi detector computed tomography (MDCT), a non-invasive imaging modality featuring large scan coverage up to 320 detector system rows, sub-millimetre spatial resolution up to 0.23 mm, and high temporal resolution up to 135 ms for a single source CT and 75 ms for a dual source CT (DSCT) system (with options for further increase using multi-segmental reconstruction techniques), is the current preferred method for CAD assessment.[3-6]

Because of patient movement, irregular heart rate, and insufficient temporal resolution for high heart rate, cardiac MDCT images are often hampered by motion artefacts. Although identification of motion artefacts in large structures such as the myocardium can be relatively easy, it is not always possible to identify motion artefacts in smaller structures like the coronary vessels. Motion artefacts in the vessel were acknowledged as discontinuity and/or blurring. [7] These artefacts could lead to misinterpretation in the coronary computed tomography angiography (CTA) analysis.

Motion artefacts are commonly evaluated qualitatively, either by visually determining their presence/absence [8] or by assigning a severity rating. [9, 10] However, this approach heavily depends on user experience and interpretation. Although qualitative analysis is not necessarily insufficient, a quantitative analysis can give more precise and objective information; and make the user aware of suspicious regions. Therefore, the purpose of this study was to develop an algorithm for quantitative image analysis for the detection of motion artefacts in coronary artery computed tomography as an added value to the qualitative analysis and test it in phantom scans of two different CT devices.

Material and methods

An anthropomorphic moving heart phantom (Limbs & Things, Bristol, UK), with an artificial coronary vessel was used. The movement of the heart phantom and the artificial coronary vessel have been shown to be comparable to the clinical setting.[10] The artificial coronary vessel was filled with a contrast agent (Ultravist-300, Schering, Switzerland) diluted to a concentration of about 250 HU. The phantom was scanned on a 64-row MDCT (64CT; Somatom Sensation 64, Siemens Medical Solutions, Forchheim, Germany) at 120 kV, 770 mAs and a DSCT (Somatom Definition, Siemens Medical Solutions, Forchheim, Germany) at 120 kV, 300 mAs/rot; both at 330ms rotation speed in cranio-caudal direction. The field of view (FOV) was set at 200 mm x 200 mm. The heart phantom was placed in supine position with its apex facing away from the bore hole. A respiratory device was connected to the phantom, which inflated and deflated the phantom at a programmed rate to simulate a beating heart and produced an ECG signal which was connected to the CT scanner.[10]. The phantom was scanned at rest and at 50 to 110 beats per minute (bpm) with 10 bpm intervals, without changing the phantom position. Twenty

preview series at intervals of 5% throughout the R-R interval were made, from which the phase in the RR interval with least motion artefacts was selected. For all dataset, 70% of the R-R interval was chosen as the optimal phase and datasets were reconstructed at 0.6/0.4 mm slice thickness/increment using kernel B25f and B26f for 64CT and DSCT, respectively. Figure 2-1 shows the scanned heart phantom, where motion artefacts were absent (left images) and present (right images).

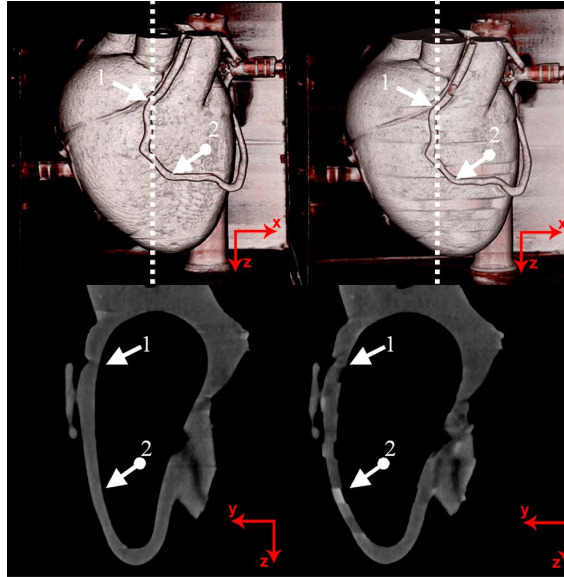


Figure 2-1. The phantom used for experiment

Images without motion artefacts (left) and with motion artefacts (right) are shown both in a volume reconstruction (top) and a sagittal reconstruction (bottom).

Arrow no. 1 and 2 denote start and end location of vessel analysis, respectively

Dotted white lines on the top row indicate the location of the sagittal slices

Two plexiglas tubes with reference/stenosis diameters of 6/4 mm and 4/2 mm (resulting in area stenosis of 56 and 75%, respectively) were also used. The lumen was filled with contrast agent (Visipaque 320, General Electric Healthcare) diluted to a concentration of about 250 HU. The vessel phantoms were scanned on the 64CT without motion at 120kV and 107 mAs. The images were reconstructed at 0.75/0.4 mm slice thickness/increment using kernel B35f.

A Siemens Syngo workstation (Siemens Medical Solutions, Erlangen, Germany) was used for visual three-dimensional observation. Software for quantitative mathematical analysis was developed using Matlab® software (Mathworks Inc, USA).

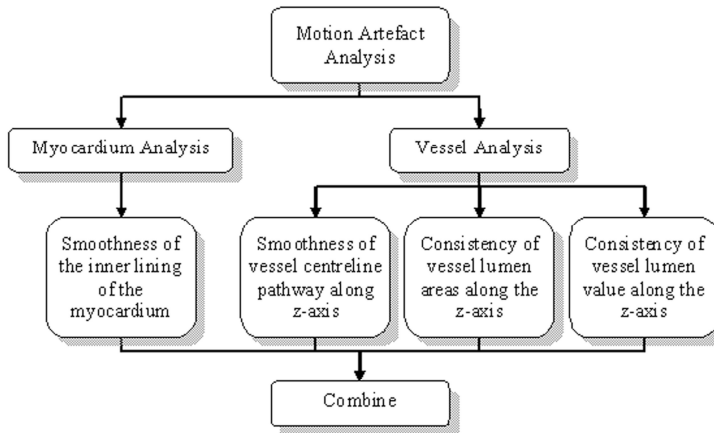


Figure 2-2. Diagram of the quantitative image analysis methods for the detection of motion artefacts in coronary artery computed tomography

Quantitative analysis

Quantitative analysis was performed in the myocardium and the coronary for each heart rate and both modalities. The analysis was performed as follows: (see figure 2-2 for the overview diagram)

I. Myocardium analysis

Due to the nature of the phantom's movement [10], motion artefacts in the myocardium were most apparent in the sagittal plane, especially in the anterior part of the myocardium. The sagittal cross-section images were taken at approximately the centre of the phantom (dotted line in figure 2-1). The anterior inner lining of the myocardium (green line at figure 2-3 left) was semi automatically extracted using a gradient vector flow (GVF) snake algorithm[11] by first placing several seed points for the initial contour which were then allowed to grow to match the inner lining. From the extracted line, the following parameter was determined:

I.a. Smoothness of the inner-lining of the myocardium

Smoothness of the inner-lining is determined by the presence of discontinuities, which was examined from its gradient. A second order polynomial line was fitted to the gradient to act as reference line. (figure 2-3 right) A Gaussian smoothing filter (width = 5; $\sigma = 4$) was applied to the gradient plot to remove possible noise. Locations with gradient deviating more than a preset threshold to the reference line were marked as motion artefacts. The threshold was set at twice the standard deviation at 0 bpm.

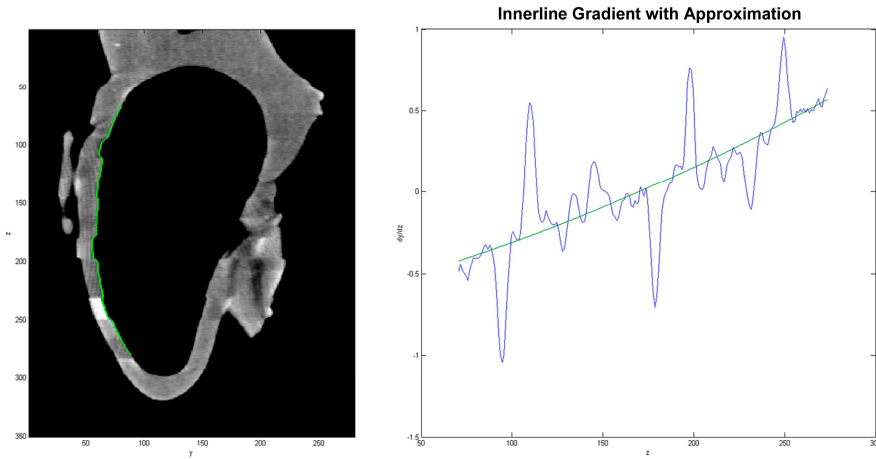


Figure 2-3. Illustration of myocardium analysis

From the sagittal cross section image of the phantom (left), the inner-lining if the myocardium was extracted (green line). The inner-lining was then analyzed for any discontinuities (right) by plotting the gradient along z-axis. Discontinuities were found at locations whose gradient deviate more than a certain threshold from the reference line.

Visual observations by two independent observers were performed. The observers were blinded to the results of the quantitative analysis. Each observer was asked to score the sagittal images for the presence of no, mild or severe motion artefacts resulting in scores of 0, 1 and 2 respectively. Consensus reading was used in case of any disagreements.

II. Vessel analysis

Because of the occurrence of motion artefacts along z-axis, the analysis was limited to the vessel segment which was relatively parallel to the z-axis. The vessel segment was predetermined and set equal for all heart rates (segment from arrow 1 to arrow 2 at figure 2-1 top). A vessel extraction algorithm based on GVF snake was developed. Started by manual selection of the vessel lumen in the axial view at location 1 of figure 2-1, a small (50 by 50 pixels) region of interest (ROI) was determined around the vessel lumen. The image inside the ROI was thresholded at level 41% of the lumen peak value.[12] Afterwards, using GVF snake algorithm, the lumen boundary was extracted and its centre of mass was determined as centre point. The detection was continued to the next slice without further user interaction, and repeated until the last slice. (figure 2-4 - top)

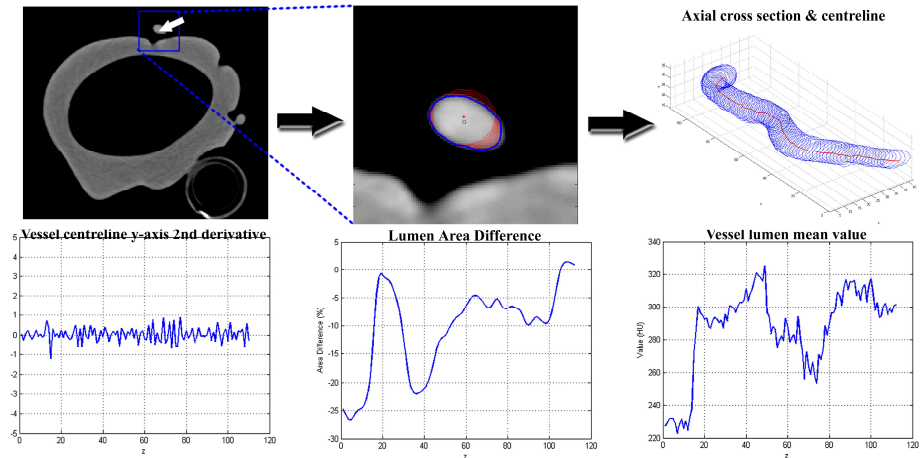


Figure 2-4. Illustration on vessel analysis

The vessel extraction algorithm (top images) is started by manual selection of the starting point (white arrow – top left) inside the vessel lumen at location 1 depicted at figure 2-1, from where an ROI (blue rectangle) was selected. Inside the ROI (top centre), the lumen boundary (bold blue line with centre point at blue circle) is detected using GVF snake algorithm. The vessel was constructed from the detected vessel boundaries and centre points (top right) along z-axis. Afterwards, the smoothness of vessel centreline (bottom left), the consistency of vessel lumen area (bottom centre) and the consistency of vessel lumen mean value (bottom right) along z-axis were analyzed.

Three parameters were determined from the extracted vessel:

- II.a. Smoothness of the vessel centreline pathway along the z-axis
The vessel centreline was constructed using the detected centre points. The smoothness of the centreline is also determined by the presence of discontinuities, which were analyzed from its second derivative in the y-direction (direction of phantom movement; see direction legends at figure 2-1-bottom) at each heart rate. Comparison to 0 bpm dataset was made.
- II.b. Consistency of vessel lumen areas along the z-axis
Blurring can smear out the vessel lumen pixels, which consequently changes the amount of pixels considered to be lumen. Therefore the consistency of lumen area along the vessel was examined. The axial lumen area on each position along the detected centreline points from each heart rate was analyzed and compared to the 0 bpm data set.
- II.c. Consistency of vessel lumen value along the z-axis
Blurring can also change the lumen intensity value. Therefore the consistency of the lumen value along the vessel was examined. The lumen mean value inside the detected lumen boundary on each position along the

detected centreline points from each heart rate was analyzed and compared to the 0 bpm data set. A mean-shift algorithm was performed to suppress noise while preserving large changes.[13]

The quantitative vessel lumen area and value consistency analysis was also applied to the second vessel phantom to see whether real stenosis would give any difference. Figure 2-4-bottom illustrates the vessel analysis methods.

The results of myocardium (I) and vessel (IIa-c) analysis were combined by correlating them side-by-side at the corresponding locations on z-axis, to determine whether there is coincidence of findings between the analysis results.

Association quantitative and qualitative analysis

A qualitative analysis was previously performed in the same dataset.[9] A direct comparison between the new quantitative method and the qualitative analysis was made.

Results

Quantitative analysis

The association between the qualitative and the developed quantitative analysis is listed on table 2-1 and 2-2, for 64CT and DSCT, respectively. The definition of quality scores are given by table 2-3.[9]

I.a. Smoothness of the inner-lining of the myocardium

The discontinuities threshold was set to 0.2. The visual observation of the two observers resulted in 38 individual motion artefacts, where 30 (79%) were identified by both observers, and eight (21%) by only one of both observers. 22 of 30 (73%) motion artefacts found by both observers were graded equal. From the 8 artefacts found only by either one of the observer, 4 were discarded after consensus. In total, the consensus resulted in 34 motion artefacts: 21 on 64CT (6 found to be severe) and 13 on DSCT (1 found to be severe). The quantitative analysis managed to find 29 out of the consented 34 motion artefacts (85%), of which all 7 (100%) severe artefacts and 22 out of 27 (81%) mild artefacts were found. None of the 4 consensus-discarded artefacts were found to be artefacts by the quantitative analysis.

Table 2-1 and 2-2 list the comparison of the true positive quantitative findings of myocardium inner-lining discontinuities artefacts versus the qualitative analysis. The qualitative findings scored DSCT with higher quality than 64CT, and the developed quantitative analysis concurred by finding more severe myocardium artefacts at 64CT. However, the same numbers of medium motion artefacts were found on both modalities. Therefore, only the severe myocardium artefacts can be related to the qualitative analysis.

Table 2-1. Qualitative[9] and quantitative motion artefact analysis on 64CT

64CT							
Quantitative Analysis							
Heart Rate (bpm)	Qualitative Analysis *)	Myocardium Inner-lining Discontinuities **)	Lumen area			Lumen value	
			Cumulative Area Differences (%)	Artefact-induced lumen area stenoses segments ***)		Lumen mean value change(s) ****)	
				Medium	Large	Medium	Large
0	4.0 ± 0	-	-	-	-	3	-
50	3.7 ± 0.8	-	-3.1	1	-	2	-
60	3.5 ± 0.5	-	-3.4	1	-	4	-
70	2.3 ± 0.5	3	-4.9	1	-	1	1(1)
80	3.8 ± 0.4	-	-3.5	1	-	2	-
90	3.0 ± 1.3	-	-4.1	1	-	1	-
100	1.3 ± 0.5	7(4)	-10.3	1(1)	2(2)	2(1)	1(1)
110	2.0 ± 0.6	7(2)	-5.1	3(3)	-	-	1(1)
Overall	3.0 ± 1.1	17(6)	-4.9	9(4)	2(2)	15(1)	3(3)

Note:

*) The value was taken from previous publication[9]. The value was given based on criteria listed in table 2-3

***) Amount of myocardium inner-lining discontinuities found by the quantitative analysis. The values between brackets indicate findings categorized as severe by visual observation.

****) Amount of vessel stenoses segments found by the quantitative analysis. The values between brackets indicate the amount of stenoses segments that coincide with myocardium artefacts.

*****) Amount of vessel lumen mean value changes found by the quantitative analysis. The values between brackets indicate the amount of the changes that coincide with myocardium artefacts.

Table 2-2. Qualitative[9] and quantitative motion artefact analysis on DSCT

DSCT							
Quantitative Analysis							
Heart Rate (bpm)	Qualitative Analysis *)	Myocardium Inner-lining Discontinuities **)	Lumen area			Lumen value	
			Cumulative Area Differences (%)	Artefact-induced lumen area stenoses segments***)		Lumen mean value change(s) ****)	
				Medium	Large	Medium	Large
0	4.3 ± 0.5	-	-	-	-	3	-
50	4.0 ± 0.6	2	-3.1	1	-	4	1
60	4.5 ± 0.5	1	0.4	-	-	3	-
70	3.8 ± 0.4	2(1)	-3.9	2(1)	-	3	1
80	4.3 ± 0.5	-	-4.8	1	-	2	-
90	4.5 ± 0.5	-	-3.4	-	-	1	-
100	4.3 ± 0.5	3	-2.7	1(1)	-	3(1)	1
110	3.8 ± 0.8	4	-6.8	2(2)	-	4	3(2)
Overall	4.2 ± 0.6	12(1)	-3.5	7(4)	-	23(1)	6(2)

Note:

*) The value was taken from previous publication[9]. The value was given based on criteria listed in table 2-3

***) Amount of myocardium inner-lining discontinuities found by the quantitative analysis. The values between brackets indicate findings categorized as severe by visual observation.

****) Amount of vessel stenoses segments found by the quantitative analysis. The values between brackets indicate the amount of stenoses segments that coincide with myocardium artefacts.

*****) Amount of vessel lumen mean value changes found by the quantitative analysis. The values between brackets indicate the amount of the changes that coincide with myocardium artefacts.

Table 2-3. Definition of image quality scores [9]

Score	Definition of image quality
1	Image with step artefacts and/or stripes throughout the image limiting evaluation of the coronary artery and pericardium
2	Image with step artefacts and/or stripes in part of the image that result in limited evaluation of the coronary artery and pericardium
3	Image with step artefacts and/or stripes which have minor implication on the evaluation of the coronary artery and pericardium
4	Image with minor motion artefacts not hampering the evaluation of the coronary artery and pericardium
5	Excellent image quality without motion artefacts

II.a. Smoothness of vessel centreline pathway along z-axis

The second derivatives of all heart rates have small absolute values below 1.5 indicating that no large discontinuities at the vessel pathway occurred and a student's t-test comparing the second derivatives of all heart rates to 0 bpm showed no significant differences ($p < 0.05$). The regular heart rate of the phantom and fixed selection of reconstruction phase in the R-R interval most probably caused the vessel to be always at the same position along the scan direction.

II.b. Consistency of vessel lumen areas along the z-axis

Comparing the lumen area of all heart rates to 0 bpm on each modality, consistent vessel volume (cumulative sum of lumen areas along the vessel) reduction was observed at all dataset, except at 60 bpm on DSCT (see table 2-1 and 2-2 under field "Cumulative Area Differences" for 64CT and DSCT, respectively). For the rest of this article, this lumen area reduction will be called stenosis (as opposed to the conventional definition of a stenosis, i.e. reduction of lumen area at certain location compared to the normal vessel proximal to it; which will be written in *italic* for the rest of the article). Although relatively small ($< 10\%$), this consistent stenosis implies that CT will always underestimate the vessel size and could thus underestimate *stenosis* severity in clinical settings. The stenoses occurred in segments, classified as medium (10 to 20%) and large ($> 20\%$) (see table 2-1 and 2-2 under field "Artefact-induced lumen area stenoses segments" for 64CT and DSCT, respectively). Small ($< 10\%$) lumen area stenoses segments were ignored because of their small significance.

Applying the algorithm to the vessel phantom, *stenoses* of $48 \pm 2\%$ and $73 \pm 3\%$ were detected for the designed *stenoses* of 56% and 75%, respectively.

Comparing to the qualitative results, the quantitative analysis concurred by finding larger overall cumulative stenosis on 64CT than on DSCT (4.9% versus 3.5%). Moreover, the largest cumulative stenosis and the presence of large stenoses segments concurred with

the lowest qualitative score at 100 bpm on 64CT. However, in the DSCT datasets qualitatively scored as ~4, medium stenoses segments were also found.

II.c. Consistency of vessel lumen value along the z-axis

Fluctuations on vessel lumen value along z-axis were observed both at 64CT and DSCT. The (absolute) changes were classified as medium (20-40HU), and large (>40HU) (see table 2-1 and 2-2 under field “Lumen mean value changes”, for 64CT and DSCT, respectively). Small (<20HU) changes were ignored because of their small significance.

Applying the algorithm to the vessel phantom, a small (10-20HU) lumen-mean value decrease and a medium (40HU) decrease were detected at the designed *stenoses* of 56% and 75%, respectively.

Comparing to the qualitative results, the quantitative analysis appears to show the opposite by finding more lumen value changes on DSCT than on 64CT. It is possible that these changes are not noticeable on the 3D VRT and curved MPR views used by the qualitative analysis.

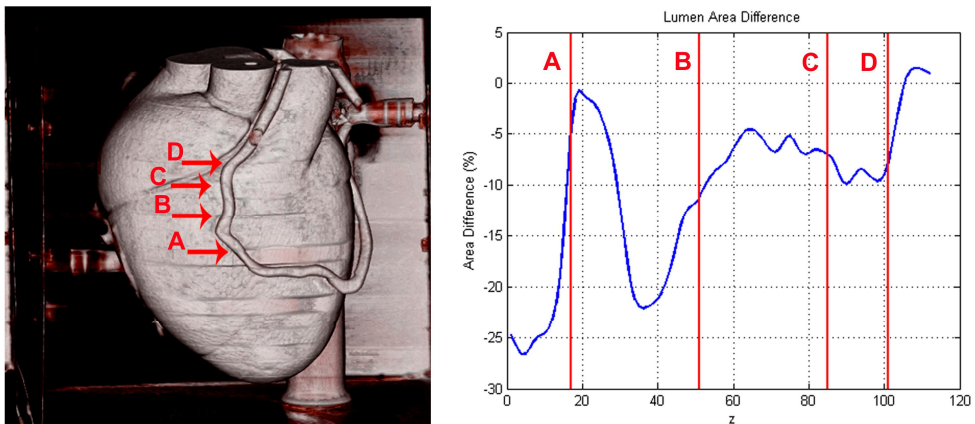


Figure 2-5. Combination of vessel (IIb) and myocardium (Ia) analysis.

The location of the detected myocardium artefacts are indicated by arrows A to D in the three-dimensional volume reconstruction view (left) and by red vertical lines A to D in the vessel lumen area consistency graph (right).

Combination of analysis

Combining the vessel lumen value (IIc) and area (IIb) analysis, one large negative lumen value change (-60HU) at 100 bpm on 64CT was found to coincide with the large lumen area stenosis (-30%). Combining the vessel lumen value (IIc) and myocardium (Ia) analysis, 2 out of 38 medium (5.3%) and 5 out of 9 (55.6%) large lumen value changes were found to coincide with the myocardium artefacts (see table 2-1 and 2-2 under field “Lumen mean value changes” - values shown between brackets). From these findings, we

can derive that motion could blur the vessel, reducing the attenuation value. From the experiment with the second vessel phantom, similar finding of a large lumen mean value decrease at the 75%-stenosis phantom was also observed, but not at the 56%-stenosis phantom. This result indicated that a large stenosis decreases the amount of lumen pixels to be significantly influenced by partial volume effect. Therefore, it is hard to distinguish artefact-induced- and real stenosis based on lumen mean value decrease alone.

Combining the vessel lumen area (IIb) and myocardium (Ia) analysis, ten out of 29 myocardium artefacts were found to correlate with lumen area stenoses, of which two were severe stenoses at 100 bpm on 64CT. Figure 2-5 shows the combined analysis at this dataset. We can directly correlate the sharp change at point A with the qualitative step artefact observation, but not at point B. Nevertheless, there is more than 20% lumen area reduction close to it. Without apparent step artefacts on the plot, this lumen area reduction could be regarded as a true *stenosis*. However, by finding a myocardial motion artefact at the corresponding location, this lumen area reduction could be marked as artefact-induced. Although, as can be seen also in point C and D in figure 2-5, the presence of motion artefacts does not always have enough effect on the vessel visualization to result in apparent stenosis. Therefore, it is useful to check for the presence of motion artefacts in corresponding location in myocardium, if a stenosis is found. However, it might not be necessary if no stenosis is detected, although those areas will still be suspicious. This recommendation is summarized by table 2-4.

Table 2-4. Recommendation to interpret findings

Type of findings		Meaning
Vessel Stenosis	Myocardial artefact	
-	-	Normal vessel
+	-	True <i>stenosis</i>
-	+	Suspicious area of motion artefact
+	+	Possible artefact-induced <i>stenosis</i>

Discussion

The developed quantitative analysis managed to detect the motion artefacts in the phantoms scans at 64CT and DSCT. Moreover, it explored into more details the effect of motion artefacts on vessel visualization, even the ones that were missed by qualitative analysis.

When evaluating the coronary arteries, the proposed procedure could warn the radiologist for suspicious areas where motion artefacts are present that could hamper the evaluation of *stenoses* in the coronary arteries. This especially holds in the case that a radiologist is reviewing segmented and stretched views of the coronary arteries in which *stenotic* lesions could easily be misinterpreted. Detection of areas of motion artefacts could help to avoid false positive findings in coronary CTA *stenoses* evaluation. A false positive finding could direct the patients into unnecessary treatment which could pose another risk such as the possible risks related to percutaneous transluminal coronary angioplasty (PTCA). Meanwhile, a false negative finding could leave patients untreated. However, on the other side, patients with undetected coronary problems could live a long time without any problem, provided the patients were not subjected to excessive physical or emotional stress.[14]

This study used 64-MDCT and DSCT, two modalities with similar characteristics except for their respective temporal resolution. DSCT has twice the temporal resolution of 64-MDCT, due to the two perpendicular x-ray tubes inside its gantry rotating simultaneously. The qualitative analysis had shown the superiority of DSCT over 64-MDCT in avoiding motion artefacts.[9] However, the quantitative analysis managed to reveal some artefacts on both modalities that would otherwise be missed.

Ferencik, et al [15] attempted to quantitatively analyze motion artefacts in coronary arteries, using two variables. The first variable is the percentage of coronary-length that is imaged without artefact, which nicely described the effect of motion to the coronaries. However, the detection of the motion artefact was performed qualitatively. In fact, our proposed method could be used for the motion artefact detection for this variable. The second variable is the contrast to noise ratio (CNR), which was calculated from the contrast of the vessel lumen mean attenuation value to the surrounding soft tissues, compared to the noise in the aorta. The consistency of vessel lumen value along z-axis measurement is similar to this variable, without comparison to surrounding soft tissue but with the advantage of location-specific depiction of motion artefacts. Otero et al [16] reported their finding of lumen mean value decrease at *stenoses* larger than 20% based on patient study. This is consistent with our finding of lumen mean value decrease at large stenosis area. However, their study excluded dataset suffering from motion artefact which makes a direct comparison with our finding not possible.

The limitation of this study is the use of phantom data instead of patients' data. Lack of real myocardium and vessel tissue of the phantom, and of surrounding pericardial fat tissue and chest cavity environment are factors that separate our phantom study to those of clinical patient examinations. Some adjustments can be made to apply our proposed method to the clinical examinations, such as: the parameters controlling GVF snake to extract myocardium boundaries, as in clinical examination, the heart chambers will be filled with contrast-enhanced blood instead of air. Other algorithm can be directly applicable to clinical examinations, such as: the lumen peak value-dependent lumen

thresholding as this method was taken from a clinical study.[12] The pre-processing step of GVF snake should be able to handle the additional noises from scattering and attenuation inside the chest cavity.

Because of radiation dose concern, an examination with lower kV is desired. However, scans with different kV will affect HU values of materials, especially ones with high atomic number such as the contrast agent. The proposed method does not use a fixed HU threshold in any of the algorithms, which should make them also applicable to such examinations. In general, this phantom experiment has its advantage in the ability to adjust the heart rate in a controlled manner. The effects of heart rates in a large interval, from low until very high, can be individually studied.

We conclude that the developed quantitative analysis adds to the diagnostic value of a qualitative analysis. The quantitative analysis allows for the detection of suspicious regions of the coronary arteries thus reducing the false positive *stenosis* rate. Several publications reported an almost perfect score of negative predictive value of MDCT in detecting *stenosis*, but lower values were reported for positive predictive value.[17-19] The quantitative analysis proposed in this study could improve the positive predictive value by reducing the number of false positive finding. Future work applying the method into clinical data still needs to be conducted. Such study would involve patients examined by MDCT with x-ray angiography as *stenosis* reference. An adjusted version of the proposed method will be applied to the data to detect and quantify motion artefacts. The interpretation recommendation listed by table 2-4 will be used to examine the images with reference to x-ray angiography findings.

References

- [1] Zheng ZJ, Croft JB, Giles WH, Mensah GA. Sudden cardiac death in the United States, 1989 to 1998. *Circulation* 2001; 104:2158-63
- [2] Heron MP, Smith BL. Deaths: leading causes for 2003. *Natl Vital Stat Rep* 2007; 55:1-92
- [3] Fan J, Dong F, Sainath P, et al Image quality evaluation of a lightspeed CT750 HD computed tomography system. In: Samei E, Hsieh J (eds) *Medical Imaging 2009: Physics of Medical Imaging*. (2009): pp 72584S-1-72584S-8
- [4] Rybicki FJ. Lower radiation dose coronary CT angiography with new imaging technologies. *The International Journal of Cardiovascular Imaging (formerly Cardiac Imaging)*1-3
- [5] Rybicki FJ, Otero HJ, Steigner ML, et al. Initial evaluation of coronary images from 320-detector row computed tomography. *The international journal of cardiovascular imaging* 2008; 24:535-46

- [6] Walker MJ, Olszewski ME, Desai MY, Halliburton SS, Flamm SD. New radiation dose saving technologies for 256-slice cardiac computed tomography angiography. *The international journal of cardiovascular imaging* 2009; 25:189-99
- [7] Leschka S, Wildermuth S, Boehm T, et al. Noninvasive coronary angiography with 64-section CT: effect of average heart rate and heart rate variability on image quality. *Radiology* 2006; 241:378-85
- [8] Dodd JD, Kalva S, Pena A, et al. Emergency cardiac CT for suspected acute coronary syndrome: qualitative and quantitative assessment of coronary, pulmonary, and aortic image quality. *AJR Am J Roentgenol* 2008; 191:870-7
- [9] Dijkers R, Greuter MJ, Kristanto W, et al. Assessment of image quality of 64-row Dual Source versus Single Source CT coronary angiography on heart rate: A phantom study. *Eur J Radiol* 2008; 70:61-8
- [10] Greuter MJ, Dorgelo J, Tukker WG, Oudkerk M. Study on motion artifacts in coronary arteries with an anthropomorphic moving heart phantom on an ECG-gated multidetector computed tomography unit. *Eur Radiol* 2005; 15:995-1007
- [11] Xu C, Prince JL. Snakes, Shapes, and Gradient Vector Flow. *IEEE Trans on Image Process* 1998; 7:359-69
- [12] Shimamoto R, Suzuki J, Yamazaki T, et al. A new method for measuring coronary artery diameters with CT spatial profile curves. *Radiography* 2007; 13:44-50
- [13] Comaniciu D, Meer P. Mean shift: A robust approach toward feature space analysis. *Ieee Transactions on Pattern Analysis and Machine Intelligence* 2002; 24:603-19
- [14] Strike PC, Perkins-Porras L, Whitehead DL, McEwan J, Steptoe A. Triggering of acute coronary syndromes by physical exertion and anger: clinical and sociodemographic characteristics. *Heart* 2006; 92:1035-40
- [15] Ferencik M, Nomura CH, Maurovich-Horvat P, et al. Quantitative parameters of image quality in 64-slice computed tomography angiography of the coronary arteries. *Eur J Radiol* 2006; 57:373-9
- [16] Otero HJ, Mitsouras D, Steigner ML, et al Contrast Opacification Gradients between Normal and Stenotic Coronary Arteries Obtained from 320-Detector Row CT Coronary Angiography. (2008): p 471
- [17] Oncel D, Oncel G, Tastan A, Tamci B. Detection of significant coronary artery stenosis with 64-section MDCT angiography. *Eur J Radiol* 2007; 62:394-405
- [18] Leber AW, Johnson T, Becker A, et al. Diagnostic accuracy of dual-source multi-slice CT-coronary angiography in patients with an intermediate pretest likelihood for coronary artery disease. *Eur Heart J* 2007; 28:2354-60
- [19] Oncel D, Oncel G, Tastan A. Effectiveness of dual-source CT coronary angiography for the evaluation of coronary artery disease in patients with atrial fibrillation: initial experience. *Radiology* 2007; 245:703-11

Chapter 3

**Small calcified coronary atherosclerotic
plaque simulation model:
Minimal size and attenuation detectable by
64-MDCT and microCT**

International Journal of Cardiovascular Imaging, 2011, vol. 28, no. 4, pp. 843-853
W. Kristanto, P.M.A. van Ooijen, J.M. Groen, R. Vliegenthart, and M. Oudkerk

Abstract

Zero calcium score may not reflect the absence of calcifications as small calcifications could be missed. This study aimed to evaluate minimal size and minimal attenuation of coronary calcifications detectable by computed tomography (CT) and to determine the minimal spatial resolution required for detecting calcification onset. Using open source CT simulation software, CTSim©, several 50%-stenotic coronary artery phantoms were designed with 5 μ m resolution, realistic morphology and tissue-specific Hounsfield Unit (HU) values. The plaque had an attenuation resembling fibrous plaque and contained a single calcification. X-ray projections were simulated with settings resembling non-contrast-enhanced 64 multi detector-row CT (64-MDCT). Scanning and reconstruction were simulated with spatial resolution of a 64-MDCT (0.4mm) and of a MicroCT (48 μ m). Starting from a single calcium granule, the calcification was simulated to grow in size and attenuation until it could be detected using clinically accepted calcium determination scheme on MicroCT and 64-MDCT images. The smallest coronary calcifications detectable at MicroCT and 64-MDCT, which had a realistic attenuation (-1024 to 3072HU), were of 25 μ m and 215 μ m diameter, respectively. The area was overestimated 7.7 and 8.8 times , respectively. Calcifications with smaller size need to have an unrealistically high attenuation to be detectable by 64-MDCT. In conclusion, 64-MDCT is only able to detect coronary calcifications with minimal diameter of 215 μ m. Consequently, early onset of calcification in coronary plaque will remain invisible when using CT and a zero calcium score can not exclude the presence of coronary calcification.

Introduction

Computed tomography (CT) is highly sensitive for the detection of coronary calcification, due to the high attenuation value of calcium. Using this property, it has been shown in multiple large prospective studies that the amount of coronary calcification, expressed as a calcium score [1], is a strong predictor of coronary events [2-4]. Therefore, the calcium score is considered a promising method to improve cardiovascular risk stratification [5-7]. Furthermore, the occurrence of coronary heart disease and mortality is extremely unlikely in asymptomatic individuals with a zero or very low calcium score [8, 9].

However, whether the absence of coronary calcium can also exclude the presence of obstructive plaque in patients with symptoms suggesting underlying coronary artery disease (CAD) is a matter of debate. In different studies with differing CT systems, the presence of significant stenosis on CT angiography in case of a zero calcium score ranged from 0 to 7% [10-14]. Although some authors have suggested that the zero calcium score can reliably exclude the presence of obstructive disease, others advise to be careful with patients with zero calcium score due to the inability to rule out CAD [13-15]. It should be proven that a zero calcium score on CT indeed means that coronary calcification is absent and that significant CAD can be safely excluded. The inability to detect small and less dense calcifications was shown in a recent phantom study, in which coronary calcification quantifications were compared between multiple 64 multidetector-row CT (MDCT) scanners from two different vendors [16].

The current MDCT technology has limited spatial resolution to detect small calcifications. Therefore, by using a software simulation model, we investigated the smallest calcification which can be detected by current CT technology and the spatial resolution needed to detect significant calcifications based on the commonly accepted HU-based threshold for calcification measurement in non-contrast-enhanced CT.

Material and methods

The simulation was conducted using an open source CT simulation software package, CTSim© 3.0 [17, 18]. The simulation was started by generating a custom-made phantom. Hereafter, x-ray projections on the phantom were simulated, and the resulting sinogram was reconstructed to make the final CT image.

Phantom generation

The phantom depicts an axial cross-section of a coronary vessel and was generated at 5 μm resolution to facilitate the smallest size of a single calcium granule, found in histopathology [19]. Realistic morphological features of the vessel and attenuation values of the tissues and materials were used [20-28]. All three layers (intima, media, and

adventitia) of a coronary vessel and the surrounding epicardial fat tissue were incorporated into the design of the phantom. Published attenuation values of carotid plaques were chosen. Although the studies reporting these values used contrast-enhanced CT scans, carotid plaques are generally large enough to be less influenced by partial volume effects, either from the lumen contrast-enhancement or the surrounding fat tissue. The lumen was simulated to be blood-filled, while both the normal and plaque-infested parts of the vessel were fibrous. The plaque was designed to build up in the intima area causing 50% area stenosis with a single calcification inside. The construction and dimension of the phantom is presented in figure 3-1A.

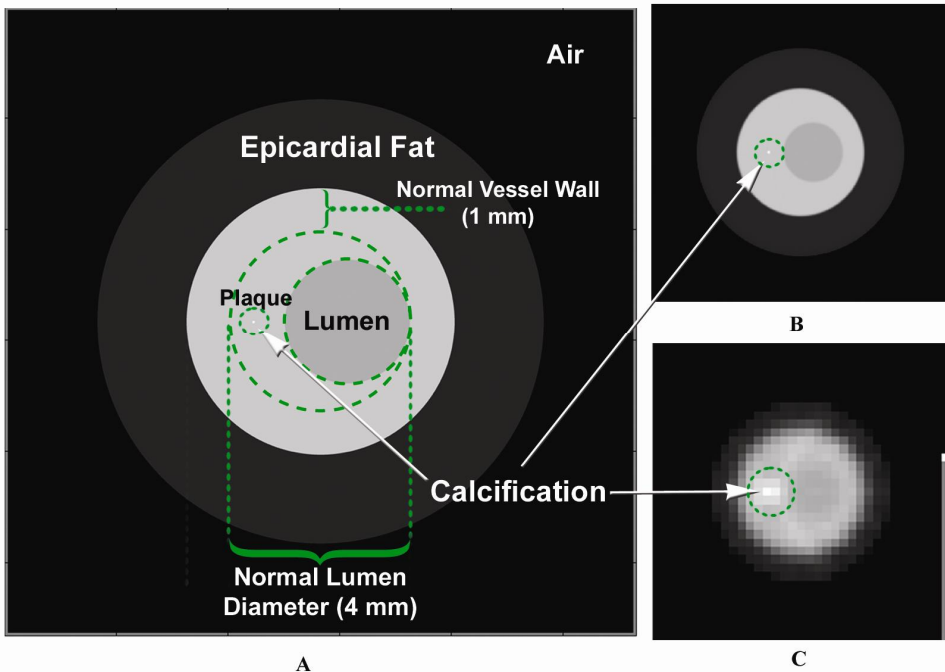


Figure 3-1. The vessel phantom (A) with fibrotic plaque and a single calcification was generated at 5 μm resolution. CT scanning simulation was conducted, generating images at MicroCT (B) and 64-MDCT (C) resolution.

Scanning simulation

X-ray projections were simulated on the generated phantom and performed with settings based on the technical specifications of a commercially available 64-MDCT scanner (Somatom Sensation 64, Siemens Medical Solution, Forchheim, Germany). This scanner was considered to be an appropriate representative of the current clinical CT systems used in cardiac imaging. The scan settings of 64-MDCT adapted to the simulation were: the scanning voltage, amount of projections to make one image slice, and spatial resolution. The generally used 120 kV voltage setting for coronary CT calcium scoring

Table 3-1. Parameters used for simulation**Phantom:**

1. Element size: 5 μm
2. Vessel morphology
 - a. Normal wall thickness: 1 mm (intima + media + adventitia); 0.5 mm (adventitia only) ¹⁾
 - b. Normal lumen diameter: 4 mm ²⁾
 - c. Vessel shape: eccentric thickening with round lumen ³⁾
3. Tissue attenuation value:
 - a. Air: -1024 HU
 - b. Blood: 50 HU ⁴⁾
 - c. Epicardial fat: -100 HU ⁵⁾
 - d. Fibrous plaque: 65 HU ⁶⁾

Scanning / X-ray Projection:

1. Detector geometry: Parallel
2. Detector size: 48 μm / 0.4 mm (MicroCT / 64-MDCT)
3. Number of projections: 1151

Reconstruction:

1. Type of reconstruction: filtered back projection (FBP)
2. Type of filter: Hanning
3. Interpolation: Linear
4. Pixel size: 48 μm / 0.4 mm (MicroCT / 64-MDCT)

Note:

- 1) Normal coronary wall layers (for all three layers and for adventitia layer only)[23], and then rounded for simplification
- 2) Normal lumen diameter.[20]
- 3) The most common plaque-burdened vessel shape.[20]
- 4) Arbitrarily chosen from the normal range of the reported value for blood. [25]
- 5) Arbitrarily chosen from the normal range used for epicardial fat.[22, 27]
- 6) Average of published carotid fibrous plaque values [21, 24, 26, 28], and then rounded for simplification

examinations was not directly simulated by the scanning parameters. Instead, since voltage settings affect the HU values of the scanned materials, it was simulated by taking the HU values for plaque tissues in the phantom construction from studies which used 120 kV scanning voltage setting. Per 180° rotation, 1151 projections were made, resembling the number of projections made by 64-MDCT at 330 ms rotation time. Due to the limitation of the software, the geometry of the detectors was set to be parallel instead of equiangular (i.e.

equal to fan beam geometry) to mimic the configuration of 64-MDCT x-ray source-detector. However, because of the relatively small size of the phantom in comparison to the distance between x-ray source and detector, a fan-beam ray passes through the phantom in a similar way as a parallel beam ray would and thus this will not influence the results. The detector array element size was set to be 0.4 mm, the spatial resolution of a 64-MDCT. The same projections were repeated with similar settings but with the detector array element size changed to 48 μm , the spatial resolution of a MicroCT system (Kristanto et al, European Society of Cardiac Radiology, Porto 2008). Inapplicable scan settings of 64-MDCT were the pitch and scanning time because the phantom was stationary, and the slice width because the phantom was two dimensional.

Two other variables of clinical scans which were indirectly incorporated in the simulation were the scan current and the scanning environment inside a thorax cage. Both are known to be related to noise, affecting image quality. Adhering to this fact, an artificial noise comparable to noise in clinical scans was incorporated at the later stage of the simulation.

Reconstruction parameters

From the resulting sinograms of the x-ray projections, images were reconstructed using the filtered back projection (FBP) method with a Hanning filter and linear interpolation. The Hanning filter was selected because of its smoothing characteristics, comparable to a medium or smooth kernel, usually applied for coronary CT calcium scoring examinations. The reconstructed image pixel size was set to 48 μm and 0.4 mm to match the MicroCT and 64-MDCT spatial resolutions, respectively (figure 3-1B and 3-1C).

The parameters used for simulation are summarized in table 3-1.

Analysis

Since a calcification grows as several calcium granules aggregate [29], the calcification was systematically simulated to grow, starting from a single calcium granule, until it was detected by either 64-MDCT or MicroCT. The growth was simulated either by altering the attenuation value (by increasing the HU value) or the size (by increasing the diameter, assuming the granules aggregate in a circular shape), thus changing the physical properties of the calcification in the phantom images. Two parameters were investigated:

1. Minimal attenuation value of detectable calcification

The diameters of the calcifications were fixed into several predefined sizes: 1-, 2-, 3-, 5-, and 10-pixel (with 1 pixel = 5 μm = 1 calcium granule). At each fixed diameter, the attenuation value was increased from 130 HU until it was detected by either CT system.

2. Minimal size of detectable calcification

The second simulation assumed that calcium granules have a specific attenuation value. The attenuation value of an area will be the average of the attenuation value of all

components in that area. As calcium granules aggregate and fill an entire pixel area, the attenuation value of the area will reflect the attenuation value of a single calcium granule. The attenuation value of this area will also be the highest since calcium is the densest plaque component. The maximum reported coronary calcification attenuation value was found to be approximately 2000 HU [30]. Therefore, the attenuation value of the calcification was fixed at 2000 HU, and then the diameter was increased starting from 1 pixel (with 1 pixel increments) until it was detected by either CT system.

The position of the calcification relative to the reconstructed image pixel borders may influence its detectability as a calcification at the center of an image pixel is blurred less than a calcification at the border of two image pixels. Therefore, additional investigation was conducted by varying the position of the calcification relative to the reconstructed image pixel(s), both for 64-MDCT and MicroCT images, into three variations: at the center of an image pixel, at the border between two image pixels, and at the border between four image pixels. (see figure 3-2).

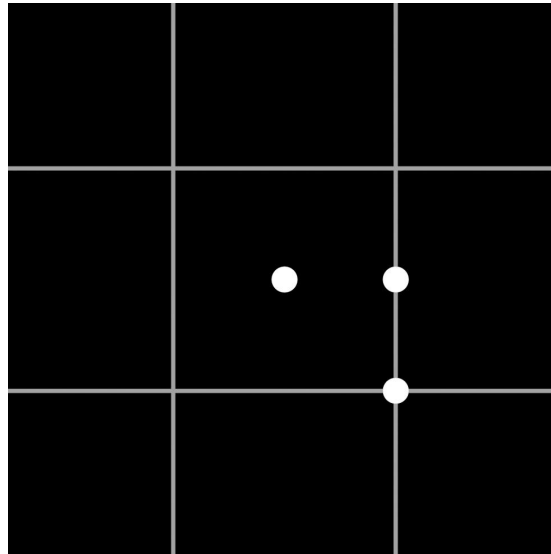


Figure 3-2. The different positioning of calcification, at the image center (1), at the border between two image pixels (2), and at the border between four image pixels (3).

Noise could hamper the image quality and subsequently the calcification's detectability. Artificial noise was incorporated into the simulation according to the method described in a previous publication, [31] by adding Gaussian noise with zero mean and sigma (σ) standard deviation to the sinograms. The σ was set to a certain value so that the noise in the reconstructed image matched the noise in normal clinical CT images used for calcium scoring application. The normal clinical CT image sample was taken from a thorax phantom scan (QRM, Möhrendorf, Germany; see figure 3-3), scanned on a 64-MDCT

scanner in sequential mode at 120 kV and 50 mAs; reconstructed using B35f kernel at 3 mm slice thickness. The noise was defined as the standard deviation inside an ROI over a homogenous area with attenuation equivalent to water. To achieve correct noise simulation in the micro CT simulation the noise has to be increased by a factor of $N\sqrt{N}$, where N corresponds to the increase in resolution when compared to 64MDCT [32]. The resolution of MicroCT was 8.3 times the 64-MDCT. Therefore, the noise in the MicroCT images is approximately 24 times the noise in the 64-MDCT images.



Figure 3-3. The photograph (left) and CT image (right) of the thorax phantom.

Each time the calcification's size, attenuation value, or position was changed, a new phantom was generated and a new simulation was conducted. Based on the known plaque area on the phantom image, a region of interest (ROI) was defined on all MicroCT and 64-MDCT images, enclosing the whole plaque area. Two calcification detection criteria were defined according to the clinically accepted threshold of 130 HU for the detection of calcified plaque regions in non-contrast-enhanced 64-MDCT: firstly, when there was 1 pixel and secondly, when there were more than (>) 1 pixel inside the plaque ROI exceeding the 130 HU threshold. The second criterion was based on the generally used suggestion in calcium scoring schemes, that a threshold of more than 1 pixel for calcification is necessary to avoid false calcium detection due to noise [1].

Results

No noise

1. Minimal attenuation value of detectable calcifications

The required attenuation value of 1, 2, 3, 5, and 10 pixel (5, 10, 15, 25, and 50 μm , respectively) diameter calcium granule(s) to be detectable by MicroCT and 64-MDCT is presented in table 3-2A and 3-2B, respectively (fixed diameter \emptyset rows). From all the detected calcium granule(s), only calcium granules with a diameter of at least 5 pixels (25 μm) which were detected by MicroCT, had an attenuation value within normal CT values

range (-1024 until +3072 HU). Smaller calcifications required an unrealistically high attenuation value beyond this range to be detected. The simulation was stopped when a calcification with attenuation value >300000 HU was still not detected.

2. Minimal size of detectable calcification

The required size of 2000 HU calcium granule(s) to be detectable by MicroCT and 64-MDCT is presented in table 3-2A and 3-2B, respectively (fixed attenuation rows). Using 1 pixel threshold, the smallest calcification detected by MicroCT and 64-MDCT were the ones positioned at the image pixel center with 20 and 175 μm diameter, respectively, with area overestimation of 5.8 and 6.7 times, respectively. Using >1 pixel threshold, the smallest calcification detected by MicroCT and 64-MDCT were the ones positioned at the border between two image pixels with 25 and 215 μm diameter, respectively, with area overestimation of 7.7 and 8.8 times, respectively.

The requirement of a calcification to be detected as 1 pixel, either by 64-MDCT or MicroCT, was constantly lower for calcification positioned at the image pixel center than the one positioned at the borders. However, to be detected as >1 pixel, the calcifications positioned at the image pixel center need the highest requirements.

With noise

The noise measured at the clinical 64-MDCT image sample was approximately 10 HU. If the same scan would have been performed at MicroCT spatial resolution without additional radiation dose, the noise level would have been at approximately 240 HU, which is too high for a diagnostic image. Inserting noise of that level to the Micro CT images will practically obscure any details, let alone the visualization of a small calcification. Therefore, the noise insertion was only performed to 64-MDCT images. Introduction of noise in the simulated 64-MDCT images changed the number of the detected calcification pixels, either by reducing the HU value of the detected calcification pixel so it went below the 130 HU threshold or by increasing the HU value of non-calcification pixel so it went above the 130 HU threshold. (see table 3-3)

One way to avoid being eliminated by the noise, the calcification pixel HU value needed to be above the noise level from the current threshold. Thus, the calcification needed to be at least 140 HU. Increasing the detection threshold accordingly, the detection requirements were updated as in table 3-4.

Table 3-2.A. Detection prerequisites for MicroCT with no noise present

Fixed	Detection prerequisites of a calcification located at						
	Center		Border 2 pixels		Border 4 pixels		
	as 1 pixel	as >1 pixel	as 1 pixel	as >1 pixel	as 1 pixel	as >1 pixel	
Diameter Ø	1 pixel	32000 HU	65000 HU	42000 HU	44000 HU	50000 HU	52000 HU
	2 pixels	8000 HU	16500 HU	10500 HU	11000 HU	12500 HU	13500 HU
	3 pixels	3500 HU	7000 HU	4700 HU	5000 HU	5600 HU	5900 HU
	5 pixels	1300 HU	2500 HU	1800 HU	1900 HU	2100 HU	2200 HU
	10 pixels	430 HU	800 HU	500 HU	600 HU	570 HU	600 HU
Attenuation	2000 HU	4 pixel Ø	6 pixel Ø	N.A.	5 pixel Ø	N.A.	6 pixel Ø

Table 3-2.B. Detection prerequisites for 64-MDCT with no noise present

Fixed	Detection prerequisites of a calcification located at						
	Center		Border 2 pixels		Border 4 pixels		
	as 1 pixel	as >1 pixel	as 1 pixel	as >1 pixel	as 1 pixel	as >1 pixel	
Diameter Ø	1 pixel	>300000 HU	>300000 HU	>300000 HU	>300000 HU	>300000 HU	>300000 HU
	2 pixels	>300000 HU	>300000 HU	>300000 HU	>300000 HU	>300000 HU	>300000 HU
	3 pixels	210000 HU	>300000 HU	>300000 HU	>300000 HU	>300000 HU	>300000 HU
	5 pixels	75000 HU	130000 HU	125000 HU	135000 HU	160000 HU	170000 HU
	10 pixels	18000 HU	30000 HU	32000 HU	35000 HU	40000 HU	41000 HU
Attenuation	2000 HU	35 pixel Ø	49 pixel Ø	40 pixel Ø	43 pixel Ø	N.A.	45 pixel Ø

Note: N.A.: data were not available since with the 1 pixel increment step, the calcification was directly detected as >1 pixel.

Table 3-3. The change of detected calcification pixels at 64-MDCT with noise present

Fixed	Change in the detected pixels						
	Center		Border 2 pixels		Border 4 pixels		
	as 1 pixel	as >1 pixel	as 1 pixel	as >1 pixel	as 1 pixel	as >1 pixel	
Diameter Ø	1 pixel	N.A.	N.A.	N.A.	N.A.	N.A.	N.A.
	2 pixels	N.A.	N.A.	N.A.	N.A.	N.A.	N.A.
	3 pixels	0	N.A.	N.A.	N.A.	N.A.	N.A.
	5 pixels	0	0	-1	-1	+1	1
	10 pixels	0	-1	-1	-1	+1	0
Attenuation	2000 HU	-1	-1	0	0	N.A.	-1

Note: N.A.: data were not available since the simulation was not performed at this setting.

Table 3-4. Detection prerequisites for 64-MDCT with noise present

Fixed	Detection prerequisites of a calcification located at						
	Center		Border 2 pixels		Border 4 pixels		
	as 1 pixel	as >1 pixel	as 1 pixel	as >1 pixel	as 1 pixel	as >1 pixel	
Diameter Ø	1 pixel	>300000 HU	>300000 HU	>300000 HU	>300000 HU	>300000 HU	>300000 HU
	2 pixels	>300000 HU	>300000 HU	>300000 HU	>300000 HU	>300000 HU	>300000 HU
	3 pixels	250000 HU	>300000 HU	>300000 HU	>300000 HU	290000 HU	>300000 HU
	5 pixels	85000 HU	150000 HU	145000 HU	155000 HU	185000 HU	190000 HU
	10 pixels	20000 HU	35000 HU	37000 HU	39000 HU	46000 HU	47000 HU
Attenuation	2000 HU	38 pixel Ø	53 pixel Ø	43 pixel Ø	46 pixel Ø	45 pixel Ø	48 pixel Ø

Discussion

In this software simulation study, the attenuation value and size requirement of small calcifications necessary to be detectable by current clinical CT systems (represented by 64-MDCT), were systematically investigated. Very small calcifications ($\leq 50 \mu\text{m}$ diameter) needed an unrealistically high attenuation value, while calcifications of a realistic attenuation value had to have at least a $215 \mu\text{m}$ (0.215 mm) diameter. Calcifications with a size or attenuation value below these requirements would simply be blurred out due to partial volume effects.

Contrast-enhanced coronary CT angiography examinations have been widely used for coronary artery disease examination, both for coronary lumen and wall assessment [33-38]. However, coronary calcification quantification based on non-contrast-enhanced coronary CT remains a solid assessment tool for predicting coronary event risk [2-4]. It has been associated with total plaque burden [39]. Although extensive calcifications are associated with more stable plaques [40-42], they are frequently found in ruptured plaques according to a histopathology study on victims of sudden coronary death [43]. However, speckled calcifications are more commonly associated with ruptured and vulnerable plaques than diffuse calcification [44]. Above all, mixed plaques with predominantly non-calcifying component are associated with acute coronary syndromes [40]. Some studies have shown that absence of coronary calcium can 100% rule out the presence of significant CAD on CT angiography in symptomatic patients [10, 12]. Other studies have found contradicting results, with significant stenoses in up to 7% of patients with zero or very low calcium score [11, 13, 14]. The sensitivity of the CT technique applied may play an important role. Furthermore, dependency of coronary calcification quantification on acquisition mode, quantification algorithm, and vendor were reported [45]. A study comparing coronary calcification quantifications by multiple 64-MDCT scanners from two different vendors addressed the inability to detect all small and less dense calcifications by all 64-MDCT scanners [16]. One pathological study reported a few missed calcifications by MDCT [46]. Another pathological study supports our findings, describing the limitations of 64-MDCT in detecting small calcifications and also the overestimation of the detected calcifications area [47]. A recent clinical study reported missed small calcifications by contrast-enhanced MDCT and confirmed the limited spatial resolution as the main cause instead of the lumen contrast-enhancement influence [48].

Stary et al noted that calcifications could be observed at the same time as the plaques reached an advanced stage [49]. However, a recent finding shows that micro-calcifications (sized $1\text{-}10 \mu\text{m}$) are already present in an early type of atherosclerotic plaque, indicating the possibility of calcium to be a marker for early development hereof atherosclerosis [50]. Vengrenyuk et al. hypothesized that micro-calcifications in the thin fibrous cap covering a lipid pool could destabilize the plaque to the point of becoming rupture-prone [51]. However, for these micro-calcifications to be detectable by 64-MDCT,

an unrealistically high attenuation value is needed. A MicroCT is necessary to detect these micro-calcifications, while a macro CT, such as the 64-MDCT, is limited to larger coronary calcifications. Langheinrich et al. showed that MicroCT with 12 μm spatial resolution could visualize small ($<100\mu\text{m}^2$ or $\sim 10\mu\text{m}$ diameter) and very dense iron deposits [52]. However, as the spatial resolution decreased, these iron deposits became blurred out and at a spatial resolution of around 50 μm , they started to be completely blurred out. This concurred with our results in a MicroCT of similar spatial resolution (48 μm), in which calcification of a similar size (2-pixel or $10\mu\text{m}$ diameter) and a similar attenuation value as the iron deposits started to be detected (see table 3-2A).

The presence of noise influenced the detectability of small calcifications, affecting more than half of the detected calcifications by 64-MDCT. The effect of noise may be avoided by setting a higher HU threshold for calcification detection. However, it will also mean that only larger and denser calcification can be detected, while smaller and less dense calcification will be missed. No noise evaluation was performed for the MicroCT images as the increased noise level will severely limit further evaluation.

The current developments in CT, in term of spatial resolution, are marked by the introduction of a new 230 μm -spatial resolution CT system [53] and the emerging technology of a 200 μm -spatial resolution flat panel CT system [47]. Higher spatial resolution may allow CT systems to detect smaller calcifications, but the main challenge lies in dealing with the accompanying higher noise level while keeping the radiation dose comparable to clinical settings [32, 52]. Technological advances such as the iterative reconstruction algorithm may offer a solution to this problem [53]. So far in-vivo modalities that may visualize ultrasmall calcifications are invasive modalities such as intravascular ultrasound (IVUS) and optical coherence tomography (OCT) [54]. However, invasive modalities can only be applied in selected high-risk patient groups.

The calcification quantification method used in this study follows the commonly accepted threshold-based calcification quantification method [1]. The method is simple yet effective, as has been shown in many studies. However, the usage of a fixed threshold to quantify coronary calcification may not properly take into account the true volume of calcification. Advanced new image post-processing techniques may improve the current established calcification quantification method.

This study does not simulate different types of vessel remodeling as the type of remodeling should not have any influence on the visualization of small calcifications. However, it is of importance in non-calcified plaque attenuation value measurements as plaque, which causes positive remodeling, had a low attenuation value, which is associated with higher vulnerability [55]. The lack of physical CT scanning properties in this study is compensated by the fact that software simulation can systematically adjust individually influencing factors while mimicking the technical settings of a CT system as closely as possible. Due to the simulation software limitation, however, some parameters, such as the x-ray source-detector geometry, can only be approximated. This also applies to properties

such as the reconstruction filter details, since these are not always disclosed by the CT vendor. The analysis is limited to two dimensional (2D) images also because of the limitation of the simulation software. However, since calcification measurement is commonly assessed based on its area [1, 39, 47], our result should sufficiently show 64-MDCT limitations in detecting calcification. Also it should be noted that calcification is a three-dimensional (3D) object and its volume comparison to the image voxel size can play a role in the partial volume effect. Although cardiac motion has been reported to affect the coronary calcium score [56], the effect of motion on the detection of small calcifications was excluded in this current study. However, it is expected that including motion will increase the size and attenuation value requirement of a small calcification to be detectable by 64-MDCT. The ideal noiseless and motionless environment gave us the opportunity to focus our study on the relation between spatial resolution and the detectability of a small calcification. Future work should incorporate all these considerations to provide even more solid proof on how small calcifications may be missed by 64-MDCT or current clinical CT systems in general.

In conclusion, 64-MDCT is only able to detect coronary calcifications with minimal diameter of 215 μm , which is approximately 40 times the smallest reported calcium granule size. Consequently, early onset of calcification in coronary plaque indicating early progression of disease and increased coronary risk to the patient will go undetected when using a clinical CT system; and a zero calcium score can not exclude the presence of coronary calcification.

Acknowledgements

The authors acknowledge the contribution of Estelle Noach for providing extensive remarks on the manuscript; also the contribution of Arjen van Hulzen and Marcel Greuter for providing advice regarding noise simulation.

References

- [1] Agatston AS, Janowitz WR, Hildner FJ, et al. Quantification of coronary artery calcium using ultrafast computed tomography. *J Am Coll Cardiol* 1990; 15:827-32
- [2] Arad Y, Goodman KJ, Roth M, Newstein D, Guerci AD. Coronary calcification, coronary disease risk factors, C-reactive protein, and atherosclerotic cardiovascular disease events the St. Francis Heart Study. *J Am Coll Cardiol* 2005; 46:158-65
- [3] Greenland P, LaBree L, Azen SP, Doherty TM, Detrano RC. Coronary artery calcium score combined with Framingham score for risk prediction in asymptomatic individuals. *Jama* 2004; 291:210-5
- [4] Vliegenthart R, Oudkerk M, Hofman A, et al. Coronary calcification improves cardiovascular risk prediction in the elderly. *Circulation* 2005; 112:572

- [5] Greenland P, Bonow RO, Brundage BH, et al. Coronary artery calcium scoring: ACCF/AHA 2007 Clinical Expert Consensus Document on coronary artery calcium scoring by computed tomography in global cardiovascular risk assessment and in evaluation of patients with chest pain. *J Am Coll Cardiol* 2007; 49:378-402
- [6] Oudkerk M, Stillman AE, Halliburton SS, et al. Coronary artery calcium screening: current status and recommendations from the European Society of Cardiac Radiology and North American Society for Cardiovascular Imaging. *Int J Cardiovasc Imaging* 2008; 24:645-71
- [7] Oudkerk M, Stillman AE, Halliburton SS, et al. Coronary artery calcium screening: current status and recommendations from the European Society of Cardiac Radiology and North American Society for Cardiovascular Imaging. *Eur Radiol* 2008; 18:2785-807
- [8] Blaha M, Budoff MJ, Shaw LJ, et al. Absence of coronary artery calcification and all-cause mortality. *JACC: Cardiovascular Imaging* 2009; 2:692-700
- [9] Sarwar A, Shaw LJ, Shapiro MD, et al. Diagnostic and prognostic value of absence of coronary artery calcification. *JACC: Cardiovascular Imaging* 2009; 2:675-88
- [10] Cheng VY, Lepor NE, Madyoon H, et al. Presence and severity of noncalcified coronary plaque on 64-slice computed tomographic coronary angiography in patients with zero and low coronary artery calcium. *Am J Cardiol* 2007; 99:1183-6
- [11] Choi EK, Choi SI, Rivera JJ, et al. Coronary computed tomography angiography as a screening tool for the detection of occult coronary artery disease in asymptomatic individuals. *J Am Coll Cardiol* 2008; 52:357
- [12] Ho JS, FitzGerald SJ, Stolfus LL, et al. Relation of a coronary artery calcium score higher than 400 to coronary stenoses detected using multidetector computed tomography and to traditional cardiovascular risk factors. *Am J Cardiol* 2008; 101:1444-7
- [13] Kelly JL, Thickman D, Abramson SD, et al. Coronary CT angiography findings in patients without coronary calcification. *Am J Roentgenol* 2008; 191:50
- [14] Rubinshtein R, Gaspar T, Halon DA, et al. Prevalence and extent of obstructive coronary artery disease in patients with zero or low calcium score undergoing 64-slice cardiac multidetector computed tomography for evaluation of a chest pain syndrome. *Am J Cardiol* 2007; 99:472-5
- [15] Greenland P, Bonow RO. How Low-Risk Is a Coronary Calcium Score of Zero?: The Importance of Conditional Probability. *Circulation* 2008; 117:1627
- [16] Dijkstra H, Greuter MJW, Groen JM, et al. Coronary calcium mass scores measured by identical 64-slice MDCT scanners are comparable: a cardiac phantom study. *Int J Cardiovasc Imaging* 2010; 26:89-98
- [17] Olszewski ME, Wahle A, Khullar D, Subramanyan K, Sonka M. A study investigating automated quantitative analyses of coronary multidetector computed tomography images. *Proceedings of SPIE* 2005; 5746:214

- [18] Rosenberg K. CTSim-The Open Source Computed Tomography Simulator. URL <http://www.ctsim.org/>[accessed 14 May 2009] 2001;
- [19] Stary HC. The development of calcium deposits in atherosclerotic lesions and their persistence after lipid regression. *Am J Cardiol* 2001; 88:16E-9E
- [20] Berglund H, Luo H, Nishioka T, et al. Highly localized arterial remodeling in patients with coronary atherosclerosis: an intravascular ultrasound study. *Circulation* 1997; 96:1470-6
- [21] de Weert TT, Ouhlous M, Meijering E, et al. In vivo characterization and quantification of atherosclerotic carotid plaque components with multidetector computed tomography and histopathological correlation. *Arterioscler Thromb Vasc Biol* 2006; 26:2366-72
- [22] Gorter PM, van Lindert ASR, de Vos AM, et al. Quantification of epicardial and peri-coronary fat using cardiac computed tomography; reproducibility and relation with obesity and metabolic syndrome in patients suspected of coronary artery disease. *Atherosclerosis* 2008; 197:896-903
- [23] Gradus-Pizlo I, Bigelow B, Mahomed Y, et al. Left anterior descending coronary artery wall thickness measured by high-frequency transthoracic and epicardial echocardiography includes adventitia. *Am J Cardiol* 2003; 91:27-32
- [24] Haraguchi K, Houkin K, Koyanagi I, Nonaka T, Baba T. Evaluation of carotid plaque composition by computed tomographic angiography and black blood magnetic resonance images. *Minim Invasive Neurosurg* 2008; 51:91-4
- [25] Noguchi K, Seto H, Kamisaki Y, et al. Comparison of fluid-attenuated inversion-recovery MR imaging with CT in a simulated model of acute subarachnoid hemorrhage. *Am J Neuroradiol* 2000; 21:923-7
- [26] Walker LJ, Ismail A, McMeekin W, et al. Computed tomography angiography for the evaluation of carotid atherosclerotic plaque: correlation with histopathology of endarterectomy specimens. *Stroke* 2002; 33:977-81
- [27] Wheeler GL, Shi R, Beck SR, et al. Pericardial and Visceral Adipose Tissues Measured Volumetrically With Computed Tomography Are Highly Associated in Type 2 Diabetic Families. *Invest Radiol* 2005; 40:97
- [28] Wintermark M, Jawadi SS, Rapp JH, et al. High-resolution CT imaging of carotid artery atherosclerotic plaques. *Am J Neuroradiol* 2008; 29:875-82
- [29] Stary HC. Natural history of calcium deposits in atherosclerosis progression and regression. *Z Kardiol* 2000; 89 Suppl 2:28-35
- [30] Galonska M, Ducke F, Kertesz-Zborilova T, et al. Characterization of atherosclerotic plaques in human coronary arteries with 16-slice multidetector row computed tomography by analysis of attenuation profiles. *Acad Radiol* 2008; 15:222-30
- [31] Joemai RMS, Geleijns J, Veldkamp WJH. Development and validation of a low dose simulator for computed tomography. *Eur Radiol* 2010; 20:958-66

- [32] Brooks RA, Di Chiro G. Statistical limitations in x-ray reconstructive tomography. *Med Phys* 1976; 3:237
- [33] Achenbach S, Ulzheimer S, Baum U. Noninvasive coronary angiography by retrospectively ECG-gated multislice spiral CT. *Circulation* 2000; 102:2823
- [34] Achenbach S, Giesler T, Ropers D, et al. Detection of coronary artery stenoses by contrast-enhanced, retrospectively electrocardiographically-gated, multislice spiral computed tomography. *Circulation* 2001; 103:2535-8
- [35] Inoue F, Sato Y, Matsumoto N, Tani S, Uchiyama T. Evaluation of plaque texture by means of multislice computed tomography in patients with acute coronary syndrome and stable angina. *Circ J* 2004; 68:840-4
- [36] Moselewski F, Ropers D, Pohle K, et al. Comparison of measurement of cross-sectional coronary atherosclerotic plaque and vessel areas by 16-slice multidetector computed tomography versus intravascular ultrasound. *Am J Cardiol* 2004; 94:1294-7
- [37] Nikolaou K, Becker CR, Muders M, et al. Multidetector-row computed tomography and magnetic resonance imaging of atherosclerotic lesions in human ex vivo coronary arteries. *Atherosclerosis* 2004; 174:243-52
- [38] Schoenhagen P, Murat Tuzcu E, Stillman AE, et al. Non-invasive assessment of plaque morphology and remodeling in mildly stenotic coronary segments: comparison of 16-slice computed tomography and intravascular ultrasound. *Coron Artery Dis* 2003; 14:459-62
- [39] Sangiorgi G, Rumberger JA, Severson A, et al. Arterial calcification and not lumen stenosis is highly correlated with atherosclerotic plaque burden in humans: a histologic study of 723 coronary artery segments using nondecalcifying methodology. *J Am Coll Cardiol* 1998; 31:126-33
- [40] Feuchtnner G, Postel T, Weidinger F, et al. Is there a relation between non-calcifying coronary plaques and acute coronary syndromes? A retrospective study using multislice computed tomography. *Cardiology* 2008; 110:241-8
- [41] Pundziute G, Schuijff JD, Jukema JW, et al. Evaluation of plaque characteristics in acute coronary syndromes: non-invasive assessment with multi-slice computed tomography and invasive evaluation with intravascular ultrasound radiofrequency data analysis. *Eur Heart J* 2008; 29:2373-81
- [42] Schuijff JD, Beck T, Burgstahler C, et al. Differences in plaque composition and distribution in stable coronary artery disease versus acute coronary syndromes; non-invasive evaluation with multi-slice computed tomography. *Acute Card Care* 2007; 9:48-53
- [43] Burke AP, Taylor A, Farb A, Malcom GT, Virmani R. Coronary calcification: insights from sudden coronary death victims. *Z Kardiol* 2000; 89:49-53
- [44] Burke AP, Weber DK, Kolodgie FD, et al. Pathophysiology of calcium deposition in coronary arteries. *Herz* 2001; 26:239-44

- [45] Greuter MJ, Dijkstra H, Groen JM, et al. 64 slice MDCT generally underestimates coronary calcium scores as compared to EBT: a phantom study. *Med Phys* 2007; 34:3510-9
- [46] Becker CR, Nikolaou K, Muders M, et al. Ex vivo coronary atherosclerotic plaque characterization with multi-detector-row CT. *Eur Radiol* 2003; 13:2094-8
- [47] Sarwar A, Rieber J, Mooyaart EAQ, et al. Calcified Plaque: Measurement of Area at Thin-Section Flat-Panel CT and 64-Section Multidetector CT and Comparison with Histopathologic Findings. *Radiology* 2008; 249:301
- [48] van der Giessen A, Gijssen F, Wentzel J, et al. Small coronary calcifications are not detectable by 64-slice contrast enhanced computed tomography. *Int J Cardiovasc Imaging* 2010; [Epub ahead of print]:
- [49] Stary HC, Chandler AB, Dinsmore RE, et al. A definition of advanced types of atherosclerotic lesions and a histological classification of atherosclerosis. A report from the Committee on Vascular Lesions of the Council on Arteriosclerosis, American Heart Association. *Circulation* 1995; 92:1355-74
- [50] Roijers RB, Dutta RK, Cleutjens JP, et al. Early calcifications in human coronary arteries as determined with a proton microprobe. *Anal Chem* 2008; 80:55
- [51] Vengrenyuk Y, Carlier S, Xanthos S, et al. A hypothesis for vulnerable plaque rupture due to stress-induced debonding around cellular microcalcifications in thin fibrous caps. *Proc Natl Acad Sci U S A* 2006; 103:14678-83
- [52] Langheinrich AC, Kampschulte M, Crömann C, et al. Role of Computed Tomography Voxel Size in Detection and Discrimination of Calcium and Iron Deposits in Atherosclerotic Human Coronary Artery Specimens. *J Comput Assist Tomogr* 2009; 33:517-22
- [53] Fan J, Dong F, Sainath P, et al. Image quality evaluation of a lightspeed CT750 HD computed tomography system. In: Samei E, Hsieh J (eds) *Medical Imaging 2009: Physics of Medical Imaging*. (2009): pp 72584S-1-72584S-8
- [54] Weinbaum S, Vengrenyuk Y, Cardoso L, et al. SYSTEM AND METHOD FOR IN VIVO IMAGING OF BLOOD VESSEL WALLS TO DETECT MICROCALCIFICATIONS. United States: Google Patents, (2007):
- [55] Schmid M, Pfloderer T, Jang IK, et al. Relationship between degree of remodeling and CT attenuation of plaque in coronary atherosclerotic lesions: An in-vivo analysis by multi-detector computed tomography. *Atherosclerosis* 2008; 197:457-64
- [56] Funabashi N, Koide K, Mizuno N, et al. Influence of heart rate on the detectability and reproducibility of multislice computed tomography for measuring coronary calcium score using a pulsating calcified mock-vessel in comparison with electron beam tomography. *Int J Cardiol* 2006; 113:113-7

Chapter 4

A systematic review and hierarchical classification of HU-based atherosclerotic plaque characterization criteria

Manuscript submitted

**W. Kristanto, P.M.A. van Ooijen, M.C. Jansen-van der Weide, R. Vliegenthart,
and M. Oudkerk**

Abstract

BACKGROUND: Many computed tomography (CT) studies have reported that lipid-rich, presumably rupture-prone atherosclerotic plaques can be characterized according to their Hounsfield Unit (HU) value. However, the published HU-based characterization criteria vary considerably. The present study aims to systematically analyze these values and empirically derive a hierarchical classification of the HU-based criteria which can be referred in clinical situation.

MATERIAL AND METHODS: A systematic search in Pubmed and Embase for publications with HU-criteria to characterize lipid-rich and fibrous atherosclerotic plaques resulted in 36 publications, published between 1998 and 2011. The HU-criteria were systematically analyzed based on the characteristics of the reporting study. Significant differences between HU-criteria were checked using student's t-test. Subsequently, a hierarchical classification of HU-criteria was developed based on the respective study characteristics.

RESULTS: No correlation was found between HU-criteria and the reported lumen contrast-enhancement. Significant differences were found for HU-criteria when pooled according to the respective study characteristics: examination type, vessel type, CT-vendor, detector-rows, voltage-setting, and collimation-width. The hierarchical classification resulted in 21 and 22 CT attenuation value categories, for lipid-rich and fibrous plaque, respectively. More than 50% of the hierarchically classified HU-criteria were significantly different.

CONCLUSION: In conclusion, variations in the reported CT attenuation values for lipid-rich and fibrous plaque are so large that generalized values are unreliable for clinical use. The proposed hierarchical classification can be used to determine reference CT attenuation values of lipid-rich and fibrous plaques for the local setting.

Introduction

Multi-detector-row computed tomography (MDCT) is currently the preferred non-invasive modality to assess the extent of coronary artery disease (CAD) [1], MDCT can reliably exclude the presence of obstructive CAD [2]. Furthermore, contrast-enhanced MDCT shows potential for differentiating types of atherosclerotic plaques, including calcified and non-calcified plaques [3]. MDCT can accurately quantify calcified plaque burden [4-6] and potentially non-calcified plaque volume [3]. However, quantitatively characterizing non-calcified plaque components has been found more challenging [7].

Characterizing the lipid-rich component of non-calcified plaques has become of increasing interest as lipid-rich, thin-capped plaques are considered to have an increased risk of rupture, with the potential sequel of an acute cardiovascular event [8, 9]. Early CT studies reported that non-calcified plaque components can be characterized based on their CT attenuation values, expressed in Hounsfield Unit (HU) [10, 11]. Since then, a number of studies on this topic has emerged, using new generations of the rapidly evolving MDCT technology [12, 13]. However, a reliable and consistent non-calcified plaque characterization based on its HU values is yet to be achieved. The reported plaque-specific HU values vary considerably. Several factors influencing non-calcified plaque HU values have been identified, among others lumen contrast-enhancement and reconstruction kernel [14, 15]. However, the fact that each study investigating HU-based non-calcified plaque characterization has different characteristics may also contribute to the considerable variation. Examples of those characteristics are examination type, vessels of interest, and CT-system. The aim of this study is to systematically investigate the published HU-based criteria to characterize non-calcified plaques, and empirically derive a hierarchical classification of the HU-based criteria, in order to assist CT determination of non-calcified components in atherosclerotic plaques in a clinical setting.

Material and methods

In this study, we systematically searched and collected publications which reported HU-criteria to characterize lipid-rich and fibrous plaques. Subsequently, the HU-criteria were systematically analyzed based on the specific characteristics of each study.

Literature study

With the guidance of a librarian and using denominator terms for several relevant publications obtained beforehand, a computerized search was performed per April 22nd, 2011 to identify relevant publications in Pubmed, using MeSH terms and free text keywords: ("Ultrasonography, Interventional"[Mesh] OR "Coronary Artery Disease"[Mesh] OR "Carotid Artery Diseases"[Mesh]) AND plaque* AND "Tomography, X-Ray Computed"[Mesh] NOT "Review "[Publication Type]; and in Embase, using the keywords: ('endoscopic echography'/exp OR 'coronary artery disease'/exp OR 'carotid

artery disease'/exp) AND 'plaque' AND 'computer assisted tomography'/exp NOT 'review'/exp/. Inclusion criteria for publication selection were: 1) original publication; 2) characterization of non-calcified plaques into lipid-rich and fibrous plaques, and report of their specific HU values; 3) using human derived materials; and 4) using other an imaging modality as plaque composition reference. Publications meeting one or more of the defined exclusion criteria were excluded (figure 4-1).

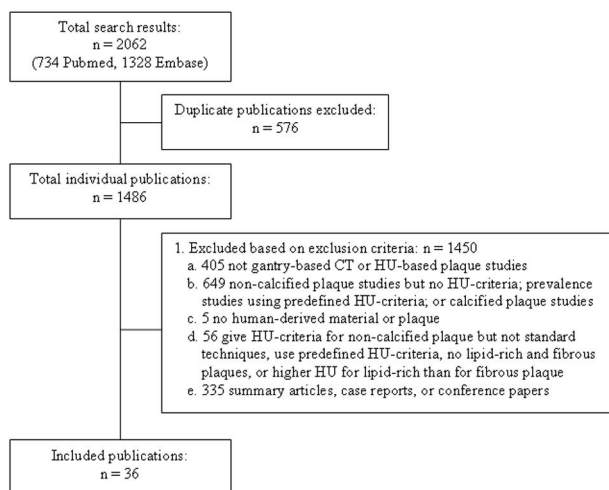


Figure 4-1. Search strategy and result.

The search yielded 2062 publications. After removing 576 duplicates (either overlaps between Pubmed and Embase results or repetitions in each database results), 1486 individual publications were screened by one reviewer (WK) based initially on the title and abstract, and when inclusion was still unclear, on the full-text of the article. In case of doubt about inclusion of a publication, arbitration was performed in a consensus meeting with a second reviewer (PvO). Finally, 1450 out of the remaining 1486 publications were excluded based on the exclusion criteria. No language or publication date related exclusions were made. In total, 36 publications were included in this study [7, 10-13, 16-46] (figure 4-1, table 4-1). A preliminary check was performed to evaluate whether one study which used two different CT modalities could be regarded as two separate studies [46] and whether another study which used four different kV settings could be regarded as four separate studies [44]. The preliminary check involved pooling all HU-criteria and pooling all HU-criteria minus one of the aforementioned studies, repeated for all six studies in question. As no significant difference in outcome was found when splitting up these studies, the two studies were treated as six studies resulting in total 40 studies for our systematical analysis obtained from the 36 publications.

Table 4-1. Characteristics of the included publications

No	Publication		Modality		Scan Settings		LC (HU)	Subject					Ref	Plaque				Ref#
	First Author	Year	Brd	DR	kV	CW (mm)		Population			SD	Ves		Lipid-rich		Fibrous		
								N	Male (%)	Age				N	Value	N	Value	
1	Becker	2003	SIE	4	120	0.5	250	11	45	(34-87)	Ex	Cor	PA	15	47±9	16	104±28	[16]
2	Brodofel	2008	SIE	64	120	0.6	NA	13	92	65±7	In	Cor	IV	NA	(-10-66)	NA	(67-153)	[17]
3	Carrascosa	2003	PHI	4	120	1	NA	30	NA	NA	In	Cor	IV	105	75.73±44.3	14	148.61±36.54	[18]
4	Carrascosa	2006	PHI	4	120	1	NA	40	80	52 (33-86)	In	Cor	IV	188	71.5±32.1	45	116.3±35.7	[19]
5	Caussin	2004	SIE	16	NA	NA	NA	21	52	58±13 (39-77)	In	Cor	IV	12	12±38*	4	63.8±18.9*	[20]
6	Chopard	2010	PHI	64	120	0.625	NA	21	NA	NA	Ex	Cor	PA	20	70±41	42	83±35	[21]
7	de Weert	2005	SIE	16	140	0.75	0	21	81	64.7 (41-81)	Ex	Car	PA	35	45±21	28	79±20	[22]
8	de Weert	2006	SIE	16	120	0.75	~400	15	40	70.3 (62-84)	In	Car	PA	31	25±19	53	88±18	[23]
9	Estes	1998	SIE	1	NA	3	150-300	20	80	74 (57-85)	In	Car	PA	NA	39±12	NA	90±24	[10]
10	Ferencik	2006	SIE	16	120	0.75	250	6	67	77±1	Ex	Cor	OC	41	29±43	40	101±21	[24]

11	Galonska	2008	GE	16	120	0.625	308	30	67	61.5± 13.4	Ex	Cor	PA	33	(26-67) med: 44	21	(37- 124) med: 67	[25]
12	Hur	2009	SIE	64	120	0.6	NA	39	72	59 (45- 74)	In	Cor	IV	10	54±13	11	82±17	[26]
13	Iriart	2007	SIE	16	120	0.75	NA	20	85	53± 12 (38- 83)	In	Cor	IV	NA	38±33	NA	94±44	[27]
14	Jin	2006	SIE	16	120	NA	NA	49	55	NA	In	Car	DU	NA	6±28	NA	51±19	[28]
15	Kim	2009	GE	64	120	0.625	NA	42	48	66±9	In	Cor	IV	28	52.9± 24.6	43	98.6± 34.9	[29]
16	Kitagawa	2007	GE	64	120	0.625	~350	21	76	66±9	In	Cor	IV	25	18±17	13	67±21	[30]
17	Kopp	2001	SIE	4	120	1	NA	6	67	60±8	In	Cor	IV	2	0.5± 7.8*	2	67± 22.6*	[11]
18	Leber	2004	SIE	16	120	0.75	NA	37	NA	NA	In	Cor	IV	62	49±22	87	91±22	[31]
19	Leschka	2010	SIE	64	120	0.6	300	25	72	72± 13 (38- 85)	Ex	Cor	PA	91	40± 17*	43	91±16	[32]
20	Marwan	2011	SIE	64	120	0.6	NA	40	75	59± 10 (52- 85)	In	Cor	IV	15	67±31	40	96±40	[33]
21	Motoyama	2007	TOS	16	135	0.5	258± 43 (174- 384)	37	84	66± 12	In	Cor	IV	18	10.6± 11.6	40	78.1± 20.8	[34]
22	Nikolaou	2004	SIE	4	120	0.5	250	17	65	(38- 86)	Ex	Cor	PA	16	45±16	21	97±31	[36]
23	Nikolaou	2004	SIE	4	120	0.5	242± 28	13	62	(34- 87)	Ex	Cor	PA	10	47±13	11	87±29	[35]
24	Pohle	2007	SIE	16	120	0.75	NA	32	72	59±8	In	Cor	IV	84	58±43	42	121±34	[12]
25	Qiu	2006	PHI	64	120 - 140	0.625	NA	6	67	77.5± 9.3	In	Cor	IV	2	-21.5± 36.6	4	85.3± 14.3	[37]

26	Sakakura	2006	TOS	16	135	0.5	NA	16	69	63±12 (42-80)	In	Cor	IV	6	50.6±14.8	11	131±21	[38]
27	Schroeder	2001	SIE	4	140	1	NA	15	87	58±10 (44-71)	In	Cor	IV	12	14±26	5	91±21	[39]
28	Schroeder	2004	SIE	4	140	1	182±34	12	NA	63±17	Ex	Cor	PA	6	42±22	6	70±21	[41]
29	Schroeder	2004	SIE	16	120	0.75	237±17	9	NA	NA	Ex	Pop	PA	13	51±20*	18	126±99	[40]
30	Shen	2010	GE	64	120	0.6	NA	91	58.2	64.78±9.19 (38-79)	In	Cor	IV	6	52.52±15.71	36	108.32±43.44	[42]
31	Soeda	2011	SIE	64	120	0.6	NA	17	82.4	63.5±8.4	In	Cor	OC	78	28.9±30.6	42	77.5±25.7	[43]
32	Sun	2008	TOS	64	120-135-80	0.5	398±74	26	65	56	In	Cor	IV	NA	79±34	NA	90±27	[13]
33	Tanami	2010	GE	32	100-120-140	0.625	0	15	73.3	72±9	Ex	Cor	PA	39	20.5±6.5 21.8±7.3 23.1±7.2 23.9±7.2	30	28.1±4.3 27.8±4.7 27.1±5 27.3±5.1	[44]
34	Wintermark	2008	GE	16	120	0.625	NA	8	100	61 (55-69)	In	Car	PA	NA	32.6±20	NA	46.4±19.9	[7]
35	Wu	2007	GE	16	120	1.25	NA	30	73	58 (43-75)	In	Cor	IV	16	23±18	19	69±21	[45]
36	Xiao	2007	GE TOS	16 64	120 120	0.625 0.5	NA	25	NA	(50-72)	Ex	Cor	PA	13	53±12 51±13	10	106±17 110±19	[46]

Notes:

1. Values in the columns Lumen Contrast, Age, and Plaque Values are in means, with the range in brackets.
2. *: Values were self-calculated
3. NA: data were not available
4. DR: Detector rows amount
5. CW: Collimation width
6. LC: Lumen contrast-enhancement
7. Brd (Manufacturer Brand):
 - a. GE: General Electric
 - b. PHI: Philips
 - c. SIE: Siemens
 - d. TOS: Toshiba
8. SD (Study Design):
 - a. Ex: Ex-vivo
 - b. In: In-vivo
9. Ves (Vessel Type):
 - a. Cor: Coronary
 - b. Car: Carotid
 - c. Pop: Popliteal
10. Ref (Reference Modality):
 - a. DU: Doppler ultrasound (DUS)
 - b. IV: Intravascular ultrasound (IVUS)
 - c. OC: Optical Coherence Tomography (OCT)
 - d. PA: Pathology

HU-criteria were collected for lipid-rich plaques (synonyms used: soft, hypoechoic, lipid, lipid-rich, hypodense, or lipid-rich necrotic core) and for fibrous plaques (synonyms used: intermediate, hyperechoic, fibrous, fibrous-rich, or connective tissue), as has been characterized by each study based on each chosen reference modality. When only the raw or partial data were presented in the publications, the plaque value (mean \pm standard deviation [SD]) was calculated [11, 20, 32, 40].

Systematic analysis of published HU-criteria

First, all published HU-criteria were pooled. Next, the correlation between published HU-criteria and the reported lumen contrast-enhancement was investigated. Finally, the published HU-criteria were pooled based on similarity of the studies concerning: 1) examination type (in-vivo or ex-vivo), 2) vessel type (coronary or other arteries), 3) CT-system brand, 4) detector-rows, 5) voltage-setting, and 6) collimation-width. Studies using a dual-source CT (DSCT) [26, 32, 33, 43] were grouped with 64-row MDCT studies because of the similarity in number of detector-rows. For the remainder of this article, DSCT was regarded as equal to 64-row MDCT. Pooling was performed by the pooled statistics, using the following formulas:

$$mean_{pooled} = \frac{N_1 mean_1 + N_2 mean_2 + \dots + N_k mean_k}{N_1 + N_2 + \dots + N_k} \quad (1)$$

$$stdev_{pooled} = \sqrt{\frac{(N_1 - 1)stdev_1^2 + (N_2 - 1)stdev_2^2 + \dots + (N_k - 1)stdev_k^2}{N_1 + N_2 + \dots + N_k - k}} \quad (2)$$

Note:

N : amount of plaques region of interests (ROIs), segments, or squares used to make the mean \pm SD

k : number of studies included

Not all information to compute the pooled statistics was available in 8 studies. Contact information of corresponding authors was used to contact them in 7 of these studies. Of these, one author replied but was not able to provide the requested missing information. Only those studies providing all the necessary information for pooling (table 4-1) were included in each pooling calculation.

Hierarchical classification

The analysis was extended by systematically classifying the HU-criteria by the following hierarchy: examination type, vessel type, CT-system brand, detector-rows, voltage-setting, and collimation width. Comparisons were made between criteria at the lowest tree branches. HU-criteria which were not significantly different were pooled.

Statistical analysis

The correlation between the published HU-criteria and the reported lumen contrast-enhancement was analyzed using linear regression analysis and was expressed as the coefficient of determination (r^2), ranging from 0 to 1 with $r^2 = 1$ indicating perfect correlation. Significant differences between the pooled HU-criteria were determined using custom-made unpaired student's t-test with unequal variances assumed in Microsoft Excel 2003 (Microsoft Corp., Redmond, Washington) at two-tailed probability $p \leq 0.05$.

Results

Preliminary analysis on the 40 analyzed studies showed that:

1. Sixteen were ex-vivo studies and 24 in-vivo studies;
2. In 34 coronary arteries were studied and in 6 other arteries (i.e. carotid and popliteal arteries);
3. Eleven studies were performed on General Electric (GE) CT-systems, 4 on Philips systems, 21 on Siemens systems, and 4 on Toshiba systems;
4. One study was performed on a 1 detector-row CT-system, 8 on 4-row MDCT, 15 on a 16-row MDCT, 4 on a 32-row MDCT, and 12 on a 64-row MDCT;
5. Two used the voltage setting <120 kV, 28 studies used 120kV, 6 studies used >120 kV, and 2 studies used variable kV settings. In 2 studies, the kV setting was not reported;
6. The collimation width applied in the CT-system in 7 studies was <0.6 mm, 17 studies applied 0.6-0.7 mm, 7 studies applied 0.7-0.8 mm., and 7 studies applied >0.8 mm collimation width In 2 studies, the collimation width was not reported.
7. Thirty eight studies reported the plaque HU values in mean \pm SD format, 1 study reported plaque median HU value and the range, and 1 study only HU value range.
8. Out of 20 in-vivo studies that examined the coronaries, 19 studies used intra-vascular ultrasound (IVUS) and 1 study used optical coherence tomography (OCT) as plaque composition reference. Out of 4 in-vivo study that examined the carotid arteries, 3 used histopathology and 1 used Doppler ultrasound (DUS) as plaque composition reference.
9. Out of 14 ex-vivo studies that examined coronaries, 13 studies used histopathology and 1 study used OCT as plaque composition reference. One ex-vivo study that examined carotid arteries and another that examined popliteal arteries used histopathology as plaque composition reference.

Systematic Analysis of Published HU-criteria

Pooling all published HU-criteria, the values for lipid-rich and fibrous plaques were: 47 ± 29 HU and 86 ± 29 HU, respectively. The published mean HU-criteria showed a low correlation with lumen contrast-enhancement, for lipid-rich ($r^2 = 0.0054$) and fibrous plaques ($r^2 = 0.0304$) (figure 4-2).

Results of the pooled HU-criteria based on similar study characteristics are shown in table 4-2. Significant differences were found for the HU-criteria for lipid-rich plaques in studies with different examination types, vessel types, CT-system brands (except General Electric (GE) versus Toshiba), detector-rows (except 16 versus 64 detector-rows), voltage-settings, and collimation-widths. In case of fibrous plaques, significant differences were found for the HU-criteria in studies with different examination types, CT-system brands (except GE versus Toshiba; and Siemens versus Toshiba), detector-rows (except 16 versus 64 detector-rows), voltage-settings, and collimation-widths (except <0.6 mm versus 0.7-0.8 mm).

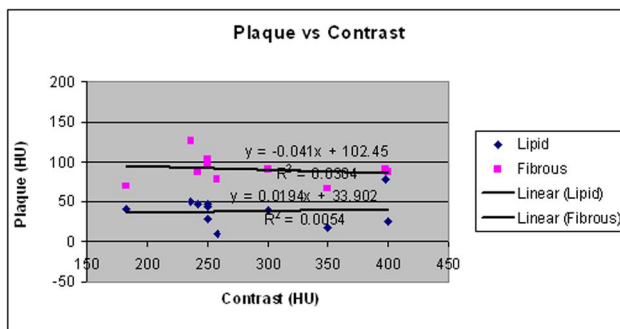


Figure 4-2. HU criteria for lipid-rich and fibrous plaques versus the reported lumen contrast-enhancement.

Table 4-2. Pooled HU-criteria

Characteristics		Ns	Lipid		Fibrous	
			Np	Mean \pm stdev	Np	Mean \pm stdev
Study design	Ex-vivo	15	429	36 \pm 20	365	73 \pm 30
	In-vivo	18	701	53 \pm 33	511	96 \pm 29
Vessel Type	Coronary	30	1051	47 \pm 29	777	85 \pm 27 [‡]
	Larger Arteries	3	79	38 \pm 20	99	92 \pm 45 [‡]
Brands	GE	9	244	28 \pm 13*	241	61 \pm 24 [§]
	Philips	4	315	72 \pm 37	105	106 \pm 35
	Siemens	17	534	41 \pm 29	469	94 \pm 32
	Toshiba	3	37	31 \pm 13*	61	93 \pm 21 ^{§,}
Rows	4	8	354	67 \pm 35	120	108 \pm 32
	16	11	332	42 \pm 31 [†]	352	95 \pm 31 [#]
	32	4	156	22 \pm 7	120	28 \pm 5
	64	9	288	41 \pm 25 [†]	284	91 \pm 32 [#]
Voltage (kV)	<120	2	78	21 \pm 7	60	28 \pm 5
	120	23	921	52 \pm 31	688	94 \pm 32
	>120	6	116	29 \pm 17	120	71 \pm 18
Collimation width (mm)	<0.6	6	78	39 \pm 13	109	95 \pm 25**
	0.6-0.7	14	444	34 \pm 21	404	72 \pm 27
	0.7-0.8	6	266	46 \pm 33	268	98 \pm 34**
	>0.8	6	329	67 \pm 36	91	106 \pm 32

Note:

1. Ns: total amount of studies included in the pooling calculation. There were studies excluded because of incomplete data needed for pooling calculation or unclear characteristics needed for classification.
2. Np : total amount of plaques ROIs, segments, or squares of the studies of similar characteristic used to make the mean \pm stdev
3. All comparisons between groups' HU-criteria within one type of characteristics were significantly different ($p \leq 0.05$) except the 7 pairs marked with the same symbols (*, †, ‡, §, ||, #, and **).

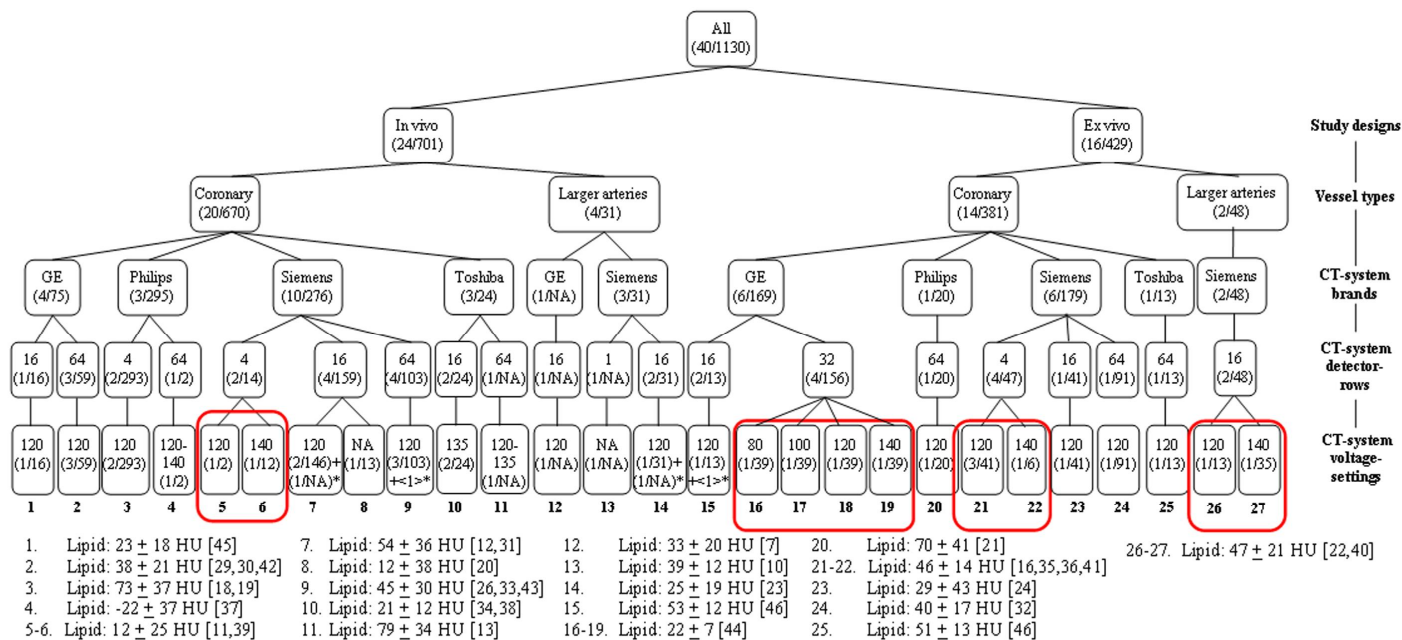


Figure 4-3. Hierarchical classification of HU-criteria for lipid-rich plaques. Values inside brackets (x/y) indicate the number of studies/plaques included, respectively. Values inside angle brackets $\langle x \rangle$ indicate the number of studies which did not report HU-criteria in mean \pm SD. NA means data were not available. Studies marked with asterisk (*) were not included in the calculation of HU-criteria of the corresponding group (group 7[27], 9[17], 14[28], and 15[25]). Bold red rounded-boxes bind groups whose criteria are not significantly different.

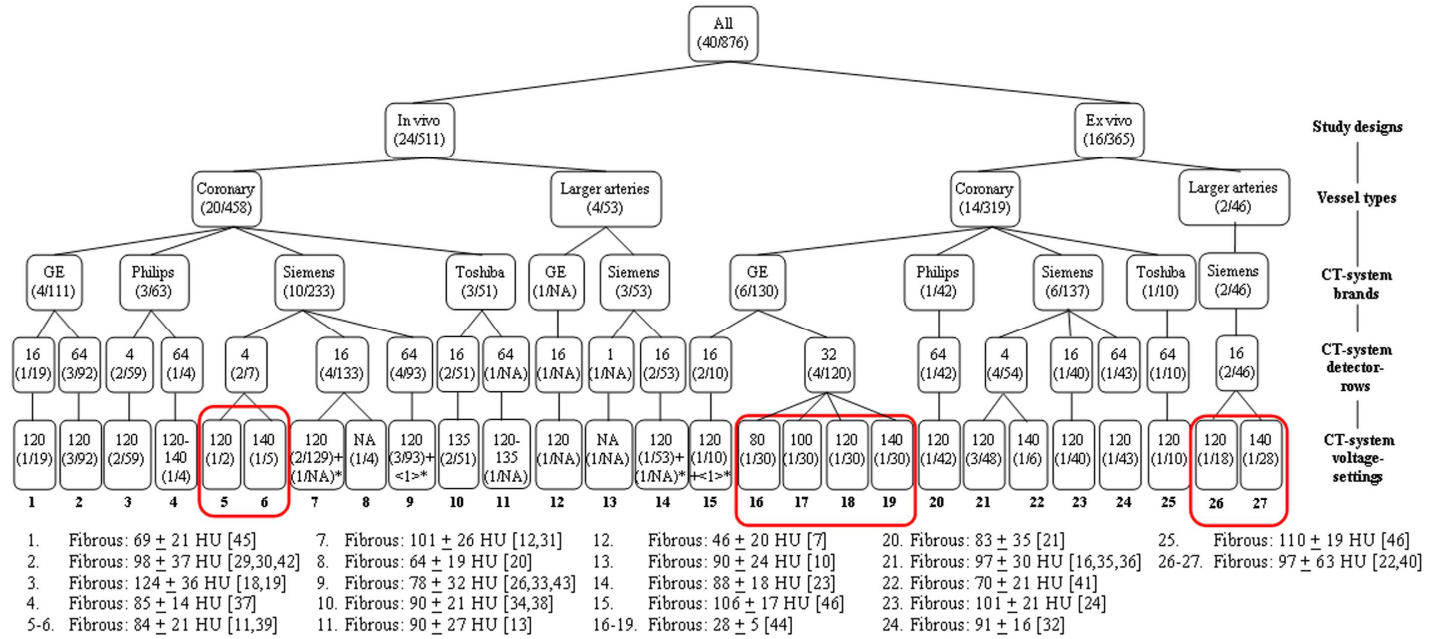


Figure 4-4. Hierarchical classification of HU-criteria for fibrous plaques. Values inside brackets (x/y) indicate the number of studies/plaques included, respectively. Values inside angle brackets <z> indicate the number of studies which did not report HU-criteria in mean ± SD. NA means data were not available. Studies marked with asterisk (*) were not included in the calculation of HU-criteria of the corresponding group (group 7[27], 9[17], 14[28], and 15[25]). Bold red rounded-boxes bind groups whose criteria are not significantly different.

Table 4-3. Comparison of HU-criteria for lipid-rich plaque between hierarchical-classified groups

		Group																					
		1	2	3	4	5-6	7	8	9	10	11	12	13	14	15	16-19	20	21-22	23	24	25	26-27	
Group	1		2	1	3	3	1	3	1	3	*	*	*	3	1	3	1	1	3	2	1	1	
	2	2		1	3	2	1	2	3	1	*	*	*	2	2	1	2	2	3	3	2	2	
	3	1	1		3	1	1	1	1	1	*	*	*	1	1	1	3	1	1	1	1	1	
	4	3	3	3		3	3	3	3	3	*	*	*	3	3	3	3	3	3	3	3	3	
	5-6	3	2	1	3		1	3	1	3	*	*	*	3	1	3	1	2	3	2	1	1	
	7	1	1	1	3	1		2	2	1	*	*	*	1	3	1	3	2	2	1	3	3	
	8	3	2	1	3	3	2		2	3	*	*	*	3	2	3	2	2	3	2	2	2	
	9	1	3	1	3	1	2	2		1	*	*	*	1	3	1	2	3	2	3	3	3	
	10	3	1	1	3	3	1	3	1		*	*	*	3	1	3	1	1	3	1	1	1	
	11	*	*	*	*	*	*	*	*	*		*	*	*	*	*	*	*	*	*	*	*	*
	12	*	*	*	*	*	*	*	*	*	*		*	*	*	*	*	*	*	*	*	*	*
	13	*	*	*	*	*	*	*	*	*	*	*		*	*	*	*	*	*	*	*	*	*
	14	3	2	1	3	3	1	3	1	3	*	*	*		1	3	1	1	3	1	1	1	
	15	1	2	1	3	1	3	2	3	1	*	*	*	1		1	3	3	2	2	3	3	
	16-19	3	1	1	3	3	1	3	1	3	*	*	*	3	1		1	1	3	1	1	1	
	20	1	2	3	3	1	3	2	2	1	*	*	*	1	3	1		2	2	2	3	2	
	21-22	1	2	1	3	2	2	2	3	1	*	*	*	1	3	1	2		2	2	3	3	
	23	3	3	1	3	3	2	3	2	3	*	*	*	3	2	3	2	2		3	2	2	
	24	2	3	1	3	2	1	2	3	1	*	*	*	1	2	1	2	2	3		2	3	
	25	1	2	1	3	1	3	2	3	1	*	*	*	1	3	1	3	3	2	2		3	
26-27	1	2	1	3	1	3	2	3	1	*	*	*	1	3	1	2	3	2	3	3			

Note:

- 1 Significantly different at $p < 0.001$
- 2 Significantly different at $p \leq 0.05$
- 3 Not significantly different
- * Comparison can not be made due to lack of data, i.e. amount of plaque

Table 4-4. Comparison of HU-criteria for fibrous plaque between hierarchical-classified groups

		Group																							
		1	2	3	4	5-6	7	8	9	10	11	12	13	14	15	16-19	20	21	22	23	24	25	26-27		
Group	1		1	1	3	3	1	3	3	2	*	*	*	1	1	1	3	1	3	1	1	1	2		
	2	1		1	3	3	3	2	1	3	*	*	*	2	3	1	2	3	2	3	3	3	3		
	3	1	1		2	2	1	2	1	1	*	*	*	1	2	1	1	1	1	1	1	1	3	2	
	4	3	3	2		3	3	3	3	3	*	*	*	3	3	2	3	3	3	3	3	3	2	3	
	5-6	3	3	2	3		3	3	3	3	*	*	*	3	2	1	3	3	3	3	3	3	2	3	
	7	1	3	1	3	3		2	1	2	*	*	*	1	3	1	2	3	2	3	2	3	3	3	
	8	3	2	2	3	3	2		3	3	*	*	*	3	2	2	3	2	3	2	3	2	2	2	
	9	3	1	1	3	3	1	3		2	*	*	*	2	1	1	3	1	3	1	2	1	3	3	
	10	2	3	1	3	3	2	3	2		*	*	*	3	2	1	3	3	3	2	3	2	3	3	
	11	*	*	*	*	*	*	*	*	*		*	*	*	*	*	*	*	*	*	*	*	*	*	*
	12	*	*	*	*	*	*	*	*	*	*		*	*	*	*	*	*	*	*	*	*	*	*	*
	13	*	*	*	*	*	*	*	*	*	*	*		*	*	*	*	*	*	*	*	*	*	*	*
	14	1	2	1	3	3	1	3	2	3	*	*	*		2	1	3	3	3	2	3	2	3	3	
	15	1	3	2	3	2	3	2	1	2	*	*	*	2		1	2	3	2	3	2	3	3	3	
	16-19	1	1	1	2	1	1	2	1	1	*	*	*	1	1		1	1	2	1	1	1	1	1	
	20	3	2	1	3	3	2	3	3	3	*	*	*	3	2	1		2	3	2	3	2	3	3	
	21	1	3	1	3	3	3	2	1	3	*	*	*	3	3	1	2		2	3	3	3	3	3	
	22	3	2	1	3	3	2	3	3	3	*	*	*	3	2	2	3	2		2	3	2	2	2	
	23	1	3	1	3	3	3	2	1	2	*	*	*	2	3	1	2	3	2		2	3	3	3	
	24	1	3	1	3	3	2	3	2	3	*	*	*	3	2	1	3	3	3	2		2	3	3	
	25	1	3	3	2	2	3	2	1	2	*	*	*	2	3	1	2	3	2	3	2		3	3	
	26-27	2	3	2	3	3	3	2	3	3	*	*	*	3	3	1	3	3	2	3	3	3		3	

Note:

- 1 Significantly different at $p < 0.001$
- 2 Significantly different at $p \leq 0.05$
- 3 Not significantly different
- * Comparison can not be made due to lack of data, i.e. amount of plaque

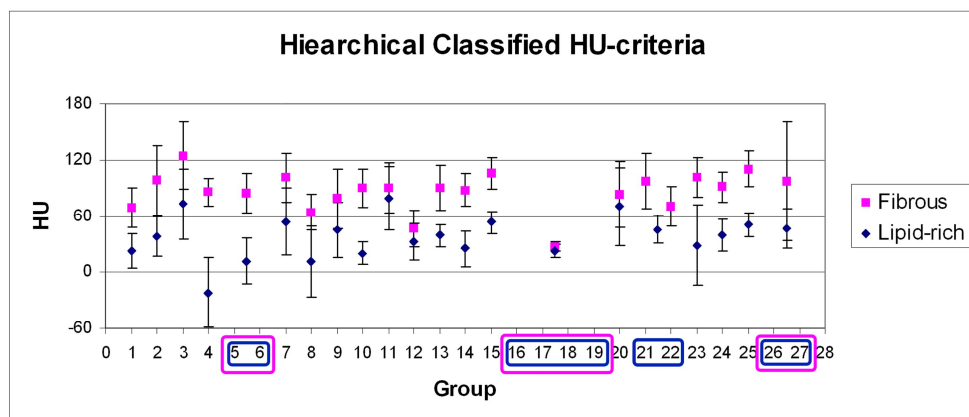


Figure 4-5. The hierarchically grouped HU-criteria for lipid-rich and fibrous plaques along with their ± 1 standard deviation range. The blue and purple rounded-boxes bound the groups that give non-significant different HU-criteria and therefore pooled, for lipid-rich and fibrous plaque, respectively.

Hierarchical classification of the published HU-criteria

Extending the analysis, a hierarchical classification of the published HU-criteria was performed, resulting in 27 distinct HU-criteria groupings (figures 4-3 and 4-4). No further classification based on collimation-width was performed because the studies included in each of these 27 groups had the same collimation-width or did not provide the collimation-width information. The criteria at the lowest tree branches, which were not significantly different, were pooled (boxed groups in figures 4-3 and 4-4), resulting in 21 and 22 distinct HU-criteria groupings for lipid-rich and fibrous plaques, respectively. Comparing the HU-criteria for lipid-rich plaque of each group to each other, 60.1% (92 out of 153 comparisons) were significantly different, of which 60.9% (56 out of 92 comparisons) were significantly different at $p < 0.001$ (table 4-3). For fibrous plaque, 52% (89 out of 171 comparisons) of the HU-criteria were significantly different, of which 46.1% (41 out of 89 comparisons) were significantly different at $p < 0.001$ (table 4-4). A visual representation of the hierarchically grouped HU-criteria along with their range (± 1 standard deviation) is given in figure 4-5.

Discussion

Plaque rupture has been identified as the most prevalent feature at sudden coronary death cases [9]. A thin fibrous cap ($<65\mu\text{m}$) and a relatively large lipid-rich content are associated to plaque's vulnerability to rupture [47]. Also, plaques showing positive remodeling are reported to contain more lipid-rich components [48, 49]. It has been suggested that MDCT should be able to measure plaque volume [50], to detect and measure positive remodeling [51] and to even follow the change of plaque characteristics after lipid-

lowering therapy [52, 53], using a simple HU-based approach. Patients having low attenuation value coronary plaques as detected by MDCT were shown to be at higher risk of an acute coronary syndrome (ACS) [54].

Direct use of HU-criteria to quantify lipid-rich plaque is not trivial as considerable variability exists in the reported HU values of lipid plaque. Over the years, CT technology has advanced rapidly from producing a thick slab image during a rather long scan time to producing submillimeter thin images in subsecond scan time, allowing for accurate coronary imaging. Due to its calibration, HU value of a material or a tissue should be equal irrespective of how or with which CT system it was acquired. However, it is advised to be extra cautious in applying absolute HU-criteria when characterizing plaques as CT attenuation values were found to differ in case of different reconstruction settings [14, 55]. The present study identified 36 publications, published between 1998 and 2011, each giving HU-criteria for lipid-rich and fibrous plaque. Specific patterns were found when the HU-criteria were pooled according to the reporting studies' characteristics. Both HU-criteria for lipid-rich and fibrous plaques were significantly lower for ex-vivo studies compared to in-vivo studies, presumably due to lack of movement during scanning. HU-criteria of coronary lipid-rich plaques were significantly higher than those of other arteries (carotid and popliteal arteries). This may be caused by more partial volume effect from the surrounding fibrous tissue and lumen contrast-enhancement due to smaller plaque size and more movement during scanning. The specific way in which each CT-vendor processes scan data may cause the significant differences in HU-criteria for different CT-systems. HU-criteria for lipid-rich plaques decreased as the number of detector-rows increased and collimation-widths of the scanner decreased. This might be explained by the fact that improvements in scanner technology with higher spatial resolution result in less partial volume effect, especially from the lumen contrast-enhancement. Materials' x-ray attenuation values depend on the x-ray photon energy, a principle behind the material decomposition with dual energy CT [56]. Our results concurred with this fact by showing that the HU-criteria for both lipid-rich and fibrous plaques were significantly higher for studies using 120 kV voltage settings than those using higher voltage settings. The significantly lower HU-criteria for studies using lower than 120 kV voltage settings is caused by the fact that the scan was performed without lumen contrast-enhancement. Lumen contrast-enhancement is one of the most frequently identified influencing sources to the non-calcified plaques' HU value [15, 57-60]. However, no direct correlation between the reported lumen contrast-enhancements and plaque HU-criteria were found in this study result. Besides by the different characteristics of the reporting studies, this lack of association may also be explained by one aspect of the measurement, i.e. the distance of the measurement ROI from the lumen border, which has been reported to affect plaque HU values [15]. Unfortunately, none of the analyzed publications reported this particular information on ROI placement which prohibits further analysis. Potential differences in patient characteristics or in tube current were not analyzed. Patient characteristics may

influence the composition of plaque [47, 61]. However, it should not have affected the HU value of the plaque as such. The tube current will mainly affect image quality and not the HU value of the plaque.

The investigated HU-criteria in this study were of the lipid-rich and fibrous plaque. However, more complex division of tissues is attributed to non-calcified plaque. The American Heart Association (AHA) has classified the atherosclerotic plaque into 6 types according to its composition, progression, and complexity [62, 63]. In several of the included CT studies, non-calcified plaque has been characterized according to the AHA classification [32, 35, 36, 40]. One study managed to characterize one other type of tissue, i.e. hemorrhage, on carotid atherosclerotic plaques [7]. However, due to the limitation of CT in spatial resolution to characterize each individual plaque component, most of the studies characterize non-calcified plaque into two categories only: low and high attenuation value, of which the previous attributed to lipid-rich plaque and the latter to fibrous plaque. Even then, the HU-criteria of lipid-rich and fibrous plaque still overlap largely. Some of the included studies proposed a HU-threshold or -range to characterize different plaque components [7, 17, 19, 22, 23, 25, 29, 30, 34, 39, 42]. Receiver operating characteristic (ROC) analysis was used to determine some threshold, showing promising accuracies (sensitivity ranged from 82% to 92%) [19, 25, 29, 30, 42].

A HU-based plaque characterization approach was used to quantify non-calcified plaques in patients in a number of studies [64-67]. However, sometimes, HU-criteria coming from studies with different characteristics than their own were applied, ranging from small differences, e.g. the generation of the CT-system used [64], to larger differences, e.g. the brand and detector-rows[53, 65]; the brand and vessel type [68]. As has been shown in the present study, HU-criteria for non-calcified plaque derived from studies with different study characteristics may be significantly different. This could result in considerably different measurements of non-calcified plaque components. Since obtaining the correct amount of lipid-rich plaques is of importance in determining the extent of vulnerable plaque [9], it is theoretically preferable to characterize plaques using criteria which match one's specific study characteristics.

Some reviews exist on non-calcified plaque characterization by CT [69, 70]. We managed to extend the discussion by systematically investigating the published HU-criteria based on specific characteristics of each study. By hierarchically grouping the HU-criteria based on the study characteristics, the effect of each characteristic was separately analyzed. As a result, 21 and 22 distinct HU-criteria were obtained from lipid-rich and fibrous plaque, respectively. Two post-mortem studies with histopathological correlation and an in-vitro validation study without reference standard reported non-significant differences in HU-criteria when using different CT-system brands [46] and voltage-settings [44, 46, 71]. In our study, some of the pooled and grouped HU-criteria comparisons were also not significantly different, but more than 50% were, indicating that specific HU-criteria correspond to specific characteristics of each study. This warrants a careful selection of the

HU-criteria, should non-calcified plaque characterization be desired. Therefore, the proposed hierarchical diagram may be consulted for using the HU-criteria in clinical practice (figures 4-3 and 4-4). The most suitable HU-criteria for lipid and fibrous plaque for a specific clinical situation can be traced, e.g. when an in-vivo examination of coronary plaque should be done on a Siemens 64-row MDCT at 120 kV, the HU-criteria of group 9 in the diagram should be used.

A limitation of our study is that the provided HU-criteria hierarchical diagram is not 100% complete as not every combination of characteristics is currently available in literature. Moreover, with the advent of more advanced CT-systems, such as the 320-MDCT and 0.23 mm spatial resolution, new HU-criteria can emerge. Not every HU-criterion presented in the diagram has the same accuracy due to unequal number of supporting studies or samples and therefore, clinical application still leaves room for improvements. Further research should provide more input for the proposed diagrams involving phantoms or arterial specimens with known plaque compositions scanned using multiple CT-systems at different settings and a clinical validation to establish a clinically useful guide with which HU-criteria can be applied per study set-up.

Conclusions

Criteria to characterize non-calcified plaques based on CT attenuation value are non-uniform, due to differences in examination type, vessels of interest, and CT scanning. Therefore, generalized values are unreliable for clinical use. The proposed hierarchical classification can be used to determine reference CT attenuation value values of lipid-rich and fibrous plaques for the local setting.

Acknowledgements

The authors acknowledge the contribution of Xie Xueqian and Zhao Yingru in translating publications from Chinese; and Estelle Noach for providing extensive remarks on the manuscript.

References

- [1] Taylor A, Cerqueira M, Hodgson J, et al. ACCF/SCCT/ACR/AHA/ASE/ASNC/NASCI/SCAI/SCMR 2010 Appropriate Use Criteria for Cardiac Computed Tomography. A Report of the American College of Cardiology Foundation Appropriate Use Criteria Task Force, the Society of Cardiovascular Computed Tomography, the American College of Radiology, the American Heart Association, the American Society of Echocardiography, the American Society of Nuclear Cardiology, the North American Society for Cardiovascular Imaging, the Society for Cardiovascular Angiography and

- Interventions, and the Society for Cardiovascular Magnetic Resonance. *J Cardiovasc Comput Tomogr* 2010; 4:407.e1-e33
- [2] Korosoglou G, Mueller D, Lehrke S, et al. Quantitative assessment of stenosis severity and atherosclerotic plaque composition using 256-slice computed tomography. *Eur Radiol* 2010; 20:1841-50
- [3] Leber AW, Becker A, Knez A, et al. Accuracy of 64-slice computed tomography to classify and quantify plaque volumes in the proximal coronary system: a comparative study using intravascular ultrasound. *J Am Coll Cardiol* 2006; 47:672-7
- [4] Leber AW, Johnson T, Becker A, et al. Diagnostic accuracy of dual-source multi-slice CT-coronary angiography in patients with an intermediate pretest likelihood for coronary artery disease. *Eur Heart J* 2007; 28:2354-60
- [5] Miralles M, Merino J, Busto M, et al. Quantification and characterization of carotid calcium with multi-detector CT-angiography. *Eur J Vasc Endovasc Surg* 2006; 32:561-7
- [6] Oudkerk M, Stillman AE, Halliburton SS, et al. Coronary artery calcium screening: current status and recommendations from the European Society of Cardiac Radiology and North American Society for Cardiovascular Imaging. *Int J Cardiovasc Imaging* 2008; 24:645-71
- [7] Wintermark M, Jawadi SS, Rapp JH, et al. High-resolution CT imaging of carotid artery atherosclerotic plaques. *Am J Neuroradiol* 2008; 29:875-82
- [8] Gao T, Zhang Z, Yu W, Zhang Z, Wang Y. Atherosclerotic carotid vulnerable plaque and subsequent stroke: a high-resolution MRI study. *Cerebrovasc Dis* 2009; 27:345-52
- [9] Virmani R, Burke AP, Farb A, Kolodgie FD. Pathology of the vulnerable plaque. *J Am Coll Cardiol* 2006; 47:13-8
- [10] Estes JM, Quist WC, Lo GFW, Costello P. Noninvasive characterization of plaque morphology using helical computed tomography. *J Cardiovasc Surg* 1998; 39:527-34
- [11] Kopp AF, Schroeder S, Baumbach A, et al. Non-invasive characterisation of coronary lesion morphology and composition by multislice CT: first results in comparison with intracoronary ultrasound. *Eur Radiol* 2001; 11:1607-11
- [12] Pohle K, Achenbach S, MacNeill B, et al. Characterization of non-calcified coronary atherosclerotic plaque by multi-detector row CT: Comparison to IVUS. *Atherosclerosis* 2007; 190:174-80
- [13] Sun J, Zhang Z, Lu B, et al. Identification and quantification of coronary atherosclerotic plaques: a comparison of 64-MDCT and intravascular ultrasound. *Am J Roentgenol* 2008; 190:748-54
- [14] Cademartiri F, La Grutta L, Runza G, et al. Influence of convolution filtering on coronary plaque attenuation values: observations in an ex vivo model of multislice computed tomography coronary angiography. *Eur Radiol* 2007; 17:1842-9

- [15] Suzuki S, Furui S, Kuwahara S, et al. Accuracy of attenuation measurement of vascular wall in vitro on computed tomography angiography: Effect of wall thickness, density of contrast medium, and measurement point. *Invest Radiol* 2006; 41:510-5
- [16] Becker CR, Nikolaou K, Muders M, et al. Ex vivo coronary atherosclerotic plaque characterization with multi-detector-row CT. *Eur Radiol* 2003; 13:2094-8
- [17] Brodoefel H, Reimann A, Heuschmid M, et al. Characterization of coronary atherosclerosis by dual-source computed tomography and HU-based color mapping: a pilot study. *Eur Radiol* 2008; 18:2466-74
- [18] Carrascosa PM, Capuñay CM, Parodi JC, et al. General utilities of multislice tomography in the cardiac field. *Herz* 2003; 28:44-51
- [19] Carrascosa PM, Capuñay CM, Garcia-Merletti P, Carrascosa J, Garcia MJ. Characterization of coronary atherosclerotic plaques by multidetector computed tomography. *Am J Cardiol* 2006; 97:598-602
- [20] Caussin C, Ohanessian A, Ghostine S, et al. Characterization of vulnerable nonstenotic plaque with 16-slice computed tomography compared with intravascular ultrasound. *Am J Cardiol* 2004; 94:99-104
- [21] Chopard R, Boussel L, Motreff P, et al. How reliable are 40 MHz IVUS and 64-slice MDCT in characterizing coronary plaque composition? An ex vivo study with histopathological comparison. *Int J Cardiovasc Imaging* 2010; 26:373-83
- [22] de Weert TT, Ouhlous M, Zondervan PE, et al. In vitro characterization of atherosclerotic carotid plaque with multidetector computed tomography and histopathological correlation. *Eur Radiol* 2005; 15:1906-14
- [23] de Weert TT, Ouhlous M, Meijering E, et al. In vivo characterization and quantification of atherosclerotic carotid plaque components with multidetector computed tomography and histopathological correlation. *Arterioscler Thromb Vasc Biol* 2006; 26:2366-72
- [24] Ferencik M, Chan RC, Achenbach S, et al. Arterial wall imaging: evaluation with 16-section multidetector CT in blood vessel phantoms and ex vivo coronary arteries. *Radiology* 2006; 240:708-16
- [25] Galonska M, Ducke F, Kertesz-Zborilova T, et al. Characterization of atherosclerotic plaques in human coronary arteries with 16-slice multidetector row computed tomography by analysis of attenuation profiles. *Acad Radiol* 2008; 15:222-30
- [26] Hur J, Kim YJ, Lee HJ, et al. Quantification and Characterization of Obstructive Coronary Plaques Using 64-Slice Computed Tomography: A Comparison With Intravascular Ultrasound. *J Comput Assist Tomogr* 2009; 33:186
- [27] Iriart X, Brunot S, Coste P, et al. Early characterization of atherosclerotic coronary plaques with multidetector computed tomography in patients with acute coronary syndrome. *Eur Radiol* 2007; 17:2581-8

- [28] Jin S, Cui SM, Tian C, et al. Study on 16-section spiral CT angiography in the evaluation of carotid artery stenosis and comparison with imaging diagnosis. *Chinese J Contemp Neurol Neurosurg* 2006; 6:398-403
- [29] Kim SY, Kim KS, Lee YS, et al. Assessment of Non-Calcified Coronary Plaques Using 64-Slice Computed Tomography: Comparison With Intravascular Ultrasound. *Korean Circ J* 2009; 39:95-9
- [30] Kitagawa T, Yamamoto H, Ohhashi N, et al. Comprehensive evaluation of noncalcified coronary plaque characteristics detected using 64-slice computed tomography in patients with proven or suspected coronary artery disease. *Am Heart J* 2007; 154:1191-8
- [31] Leber AW, Knez A, Becker A, et al. Accuracy of multidetector spiral computed tomography in identifying and differentiating the composition of coronary atherosclerotic plaques A comparative study with intracoronary ultrasound. *J Am Coll Cardiol* 2004; 43:1241-7
- [32] Leschka S, Seitun S, Dettmer M, et al. Ex vivo evaluation of coronary atherosclerotic plaques: characterization with dual-source CT in comparison with histopathology. *J Cardiovasc Comput Tomogr* 2010; 4:301-8
- [33] Marwan M, Taher MA, El Meniawy K, et al. In vivo CT detection of lipid-rich coronary artery atherosclerotic plaques using quantitative histogram analysis: A head to head comparison with IVUS. *Atherosclerosis* 2011; 215:110-5
- [34] Motoyama S, Kondo T, Anno H, et al. Atherosclerotic Plaque Characterization by 0.5-mm-Slice Multislice Computed Tomographic Imaging: Comparison With Intravascular Ultrasound. *Circ J* 2007; 71:363-6
- [35] Nikolaou K, Becker CR, Muders M, et al. Multidetector-row computed tomography and magnetic resonance imaging of atherosclerotic lesions in human ex vivo coronary arteries. *Atherosclerosis* 2004; 174:243-52
- [36] Nikolaou K, Becker CR, Wintersperger BJ, et al. Evaluierung der Mehrzeilendetektorcomputertomographie zur Darstellung der koronaren Atherosklerose. *Radiologe* 2004; 44:130-9
- [37] Qiu JX, Wang JC, Sun XW, et al. Detection of coronary atherosclerosis by 64-slice spiral CT: Comparison with intravascular ultrasound. *Chinese J Med Imaging Technol* 2006; 22:1456-9
- [38] Sakakura K, Yasu T, Kobayashi Y, et al. Noninvasive tissue characterization of coronary arterial plaque by 16-slice computed tomography in acute coronary syndrome. *Angiology* 2006; 57:155-60
- [39] Schroeder S, Kopp AF, Baumbach A, et al. Noninvasive detection and evaluation of atherosclerotic coronary plaques with multislice computed tomography. *J Am Coll Cardiol* 2001; 37:1430-5

- [40] Schroeder S, Kuettner A, Wojak T, et al. Non-invasive evaluation of atherosclerosis with contrast enhanced 16 slice spiral computed tomography: results of ex vivo investigations. *Heart* 2004; 90:1471-5
- [41] Schroeder S, Kuettner A, Leitritz M, et al. Reliability of differentiating human coronary plaque morphology using contrast-enhanced multislice spiral computed tomography: a comparison with histology. *J Comput Assist Tomogr* 2004; 28:449-54
- [42] Shen Y, Qian JY, Wang MH, et al. Quantitative and qualitative assessment of non-obstructive left main coronary artery plaques using 64-multislice computed tomography compared with intravascular ultrasound. *Chin Med J* 2010; 123:827-33
- [43] Soeda T, Uemura S, Morikawa Y, et al. Diagnostic accuracy of dual-source computed tomography in the characterization of coronary atherosclerotic plaques: Comparison with intravascular optical coherence tomography. *Int J Cardiol* 2011; 148:313-8
- [44] Tanami Y, Ikeda E, Jinzaki M, et al. Computed tomographic attenuation value of coronary atherosclerotic plaques with different tube voltage: an ex vivo study. *J Comput Assist Tomogr* 2010; 34:58-63
- [45] Wu WH, Lu B, Jiang SL, et al. Noninvasive detection and evaluation of coronary atherosclerotic plaques with multi-slice spiral CT: A comparative study with intravascular ultrasonography. *Chinese J Radiol* 2007; 41:1027-31
- [46] Xiao XG, Xie DX, Shen BZ, et al. Value of multi-slice computed tomography in diagnosis of coronary plaque characterization. *Zhonghua yi xue za zhi* 2007; 87:3247-50
- [47] Burke AP, Farb A, Malcom GT, et al. Coronary risk factors and plaque morphology in men with coronary disease who died suddenly. *N Engl J Med* 1997; 336:1276-82
- [48] Schmid M, Pflederer T, Jang IK, et al. Relationship between degree of remodeling and CT attenuation of plaque in coronary atherosclerotic lesions: An in-vivo analysis by multi-detector computed tomography. *Atherosclerosis* 2008; 197:457-64
- [49] Varnava AM, Mills PG, Davies MJ. Relationship between coronary artery remodeling and plaque vulnerability. *Circulation* 2002; 105:939-43
- [50] Brodoefel H, Burgstahler C, Heuschmid M, et al. Accuracy of dual-source CT in the characterization of non-calcified plaque: use of a colour-coded analysis compared with virtual histology intravascular ultrasound. *Brit J Radiol* 2009;
- [51] Schoenhagen P, Murat Tuzcu E, Stillman AE, et al. Non-invasive assessment of plaque morphology and remodeling in mildly stenotic coronary segments: comparison of 16-slice computed tomography and intravascular ultrasound. *Coron Artery Dis* 2003; 14:459-62
- [52] Sato Y, Inoue F, Yoshimura A, et al. Regression of an atherosclerotic coronary artery plaque demonstrated by multislice spiral computed tomography in a patient with stable angina pectoris. *Heart Vessels* 2003; 18:224-6

- [53] Kunita E, Fujii T, Urabe Y, et al. Coronary plaque stabilization followed by Color Code Plaque analysis with 64-slice multidetector row computed tomography. *Circ J* 2009; 73:772-5
- [54] Motoyama S, Sarai M, Harigaya H, et al. Computed tomographic angiography characteristics of atherosclerotic plaques subsequently resulting in acute coronary syndrome. *J Am Coll Cardiol* 2009; 54:49-57
- [55] Achenbach S, Boehmer K, Pflederer T, et al. Influence of Slice Thickness and Reconstruction Kernel on the CT Attenuation of Coronary Atherosclerotic Plaque. *J Cardiovasc Comput Tomogr* 2010; 4:110-5
- [56] Johnson TR, Krauss B, Sedlmar M, et al. Material differentiation by dual energy CT: initial experience. *Eur Radiol* 2007; 17:1510-7
- [57] Cademartiri F, Mollet NR, Runza G, et al. Influence of intracoronary attenuation on coronary plaque measurements using multislice computed tomography: observations in an ex vivo model of coronary computed tomography angiography. *Eur Radiol* 2005; 15:1426-31
- [58] Fei X, Du X, Yang Q, et al. 64-MDCT Coronary Angiography: Phantom Study of Effects of Vascular Attenuation on Detection of Coronary Stenosis. *Am J Roentgenol* 2008; 191:43-9
- [59] Halliburton SS, Schoenhagen P, Nair A, et al. Contrast enhancement of coronary atherosclerotic plaque: a high-resolution, multidetector-row computed tomography study of pressure-perfused, human ex-vivo coronary arteries. *Coron Artery Dis* 2006; 17:553-60
- [60] Horiguchi J, Fujioka C, Kiguchi M, et al. Soft and intermediate plaques in coronary arteries: how accurately can we measure CT attenuation using 64-MDCT? *Am J Roentgenol* 2007; 189:981-8
- [61] Kitagawa T, Yamamoto H, Horiguchi J, et al. Characterization of noncalcified coronary plaques and identification of culprit lesions in patients with acute coronary syndrome by 64-slices computed tomography. *JACC Cardiovascular Imaging* 2009; 2:153-60
- [62] Sary HC, Chandler AB, Glagov S, et al. A definition of initial, fatty streak, and intermediate lesions of atherosclerosis. A report from the Committee on Vascular Lesions of the Council on Arteriosclerosis, American Heart Association. *Circulation* 1994; 89:2462-78
- [63] Sary HC, Chandler AB, Dinsmore RE, et al. A definition of advanced types of atherosclerotic lesions and a histological classification of atherosclerosis. A report from the Committee on Vascular Lesions of the Council on Arteriosclerosis, American Heart Association. *Circulation* 1995; 92:1355-74
- [64] Gaudio C, Mirabelli F, Pelliccia F, et al. Early detection of coronary artery disease by 64-slice multidetector computed tomography in asymptomatic hypertensive high-risk patients. *Int J Cardiol* 2009; 135:280-6

- [65] Hammer-Hansen S, Kofoed KF, Kelbæk H, et al. Volumetric evaluation of coronary plaque in patients presenting with acute myocardial infarction or stable angina pectoris--a multislice computerized tomography study. *Am Heart J* 2009; 157:481-7
- [66] Motoyama S, Kondo T, Sarai M, et al. Multislice computed tomographic characteristics of coronary lesions in acute coronary syndromes. *J Am Coll Cardiol* 2007; 50:319-26
- [67] Rozie S, de Weert TT, De Monyé C, et al. Atherosclerotic plaque volume and composition in symptomatic carotid arteries assessed with multidetector CT angiography; relationship with severity of stenosis and cardiovascular risk factors. *Eur Radiol* 2009; 19:2294-301
- [68] Saba L, Montisci R, Sanfilippo R, Mallarini G. Multidetector row CT of the brain and carotid artery: a correlative analysis. *Clin Radiol* 2009; 64:767-78
- [69] Foster G, Shah H, Sarraf G, Ahmadi N, Budoff M. Detection of noncalcified and mixed plaque by multirow detector computed tomography. *Expert Rev Cardiovasc Ther* 2009; 7:57-64
- [70] Springer I, Dewey M. Comparison of multislice computed tomography with intravascular ultrasound for detection and characterization of coronary artery plaques: A systematic review. *Eur J Radiol* 2009; 71:275-82
- [71] Horiguchi J, Fujioka C, Kiguchi M, et al. In vitro measurement of CT density and estimation of stenosis related to coronary soft plaque at 100kV and 120kV on ECG-triggered scan. *Eur J Radiol* 2011; 77:294-8

Chapter 5

**Non-calcified coronary atherosclerotic
plaque visualization on CT:**

**Effects of contrast-enhancement and lipid-
content fractions**

Manuscript submitted

**W. Kristanto, P.M.A. van Ooijen, M.J.W. Greuter, J.M. Groen, R. Vliegenthart,
and M. Oudkerk**

Abstract

Computed tomography (CT) may characterize lipid-rich and presumably rupture-prone non-calcified coronary atherosclerotic plaque based on its Hounsfield-Unit (HU), but still inconclusively. This study aimed to evaluate factors influencing the HU-value of non-calcified plaque using software simulation. Several realistic virtual plaque-burdened coronary phantoms were constructed at 5 μ m resolution. CT scanning was simulated with settings resembling a 64-row multi-detector CT (64-MDCT) and reconstructed at 64-MDCT (0.4mm) and MicroCT (48 μ m) resolutions. Influences of lumen contrast-enhancement, stenosis-grades, and plaque compositions on plaque visualization were analyzed. Lumen contrast-enhancement and mean plaque HU-value were positively correlated ($R^2 > 0.92$), with approximately the same slopes for all plaque compositions. Percentage lipid-content and mean plaque HU-value were negatively correlated ($R^2 > 0.98$). Stenosis-grade and noise had minimal influence on the correlations. Influence of lumen contrast-enhancement on plaque HU-value was following a specific exponentially declining pattern ($y = Ae^{-\lambda x} + c$) from the lumen border until 2-pixel radius. Outside 2-pixel radius, plaque HU-values deviated maximally 5HU from non-contrast-enhanced reference. Thus, to avoid lumen contrast-enhancement influence, plaques should be measured outside 2-pixel radius from the lumen border. Based on the patterns found, a lumen influence correction algorithm may be developed. HU-based plaque percentage lipid-content determination might serve as an alternative plaque characterization method. However, its applicability is still hindered by many inherent limitations.

Introduction

Computed-tomography (CT) is currently the preferred modality to assess the extent of coronary artery disease (CAD) in a non-invasive manner. CT not only excels in stenosis detection [1, 2] but also in measurement of calcified plaque burden [3-5]. The amount of coronary calcification quantified by CT is a strong predictor of coronary heart disease [6-8], although it does not accurately predict the site of stenosis [9]. In contrast, non-calcified plaque characterization and quantification by CT so far has been anything but conclusive. Differentiation between types of non-calcified plaques may allow identification of plaques which are more vulnerable to rupture and which, consequently, could cause an acute coronary syndrome. Generally, lipid-rich plaques are considered to be more prone to rupture than fibrous plaques [10-12].

Several studies [13-15] reported various Hounsfield Unit (HU)-based criteria to distinguish lipid-rich from fibrous plaque, but the criteria have so far been discordant. Moreover, the HU values for distinguishing these two plaque types are overlapping, which makes distinction so far inaccurate. The main causes of the problem are the small size of plaques combined with the low CT contrast difference between lipid-rich plaque and fibrous plaque, and the suboptimal spatial resolution of CT. Those studies refer to other modalities (such as intravascular ultrasound and histology) to depict a certain plaque type and then find the corresponding plaque in CT [13-15]. However, the difference in spatial resolution between CT and those modalities makes 100% correct plaque type correspondence impossible. Other aspects, such as lumen contrast-enhancement and lipid-content percentage, have been reported to also affect the measured plaque CT number and the detectability of lipid-rich plaques [16, 17].

By using software simulation, this study aimed to evaluate and quantify the factors influencing non-calcified plaque visualization and differentiation in order to define guidelines on how to best perform non-calcified plaque differentiation on CT.

Material and methods

The simulation was conducted using open source CT simulation software, CTSim© 3.0 [18]. This software was also used in studies reported in previous publications, for general CT visualization research [19] and specifically for coronary and plaque visualization [20, 21]. The simulation was started by generating custom-made phantoms. Subsequently, x-ray projections of these phantoms were simulated and the resulting sinograms were reconstructed to obtain the final CT images.

Phantom generation

The phantoms depicted axial cross-sections of a coronary vessel, which were generated at 5 μm spatial resolution. Representative morphological features and dimensions of the vessel and realistic attenuation coefficient of the tissues and materials were applied,

derived from accepted standards and previously reported CT numbers of different non-calcified carotid plaque types [22-30]. CT numbers of carotid plaques were used, because carotid plaques are assumed to be large enough to be less influenced by partial volume effects and motion than coronary plaques. All three layers (intima, media, and adventitia) of a coronary vessel were incorporated into the design of the vessel phantom. (see figure 5-1 and table 5-1). The attenuation coefficients of different materials will be represented in HU for the rest of the article.

Table 5-1. Simulation parameters

Phantom:

1. Element size: 5 μm
2. Vessel morphology
 - a. Normal wall thickness: 1 mm (intima + media + adventitia); 0.5 mm (adventitia)^a
 - b. Normal lumen diameter: 4 mm^b
 - c. Atherosclerosis shape: eccentric plaque with circular lumen^c
3. Tissue CT numbers:
 - a. Air: -1024 HU
 - b. Blood: 50 HU^d
 - c. Epicardial fat: -100 HU^e
 - d. Contrast-enhanced lumen: 200/250/300/350/400 HU
 - e. Fibrous plaque: 65 HU^f
 - f. Lipid-rich plaque: 30 HU^g

Scanning / X-ray Projection: Detector size: 48 μm / 0.4 mm (MicroCT / 64-MDCT)

Noise addition: 6, 12, 19 HU

Reconstruction: Pixel size: 48 μm / 0.4 mm (MicroCT / 64-MDCT)

Note:

^a Normal coronary wall layers (for all three layers and for adventitia layer only)[25]

^b Normal lumen diameter.[22]

^c The most common coronary atherosclerosis shape.[22]

^d Arbitrarily chosen from the normal range for blood. [27]

^e Arbitrarily chosen from the normal range for epicardial fat.[24, 29]

^f Average of carotid fibrous plaque values [23, 26, 28, 30]

^g Average of carotid lipid-rich plaque values [23, 26, 30]

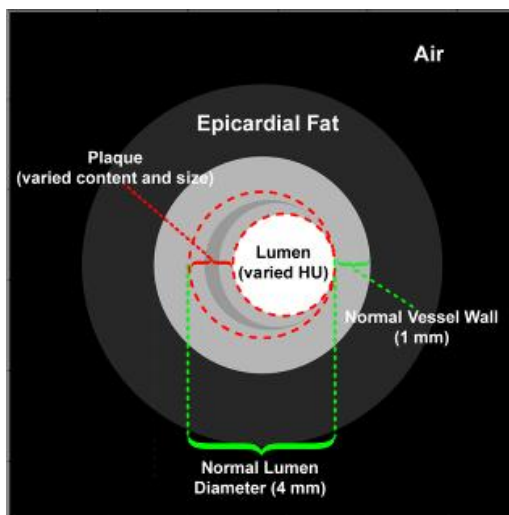


Figure 5-1. The constructed phantom morphology. The figure shows a typical example of the virtual vessel infested by a plaque containing 25% lipid-content which causes 75% stenosis.

The content and morphology of the lumen and the plaque were varied to investigate their influence on plaque-burdened vessel visualization, as follows:

1. Lumen HU value: The lumen was either non-contrast-enhanced (blood-filled at 50 HU) or contrast-enhanced (200 to 400 HU, with 50 HU increments).
2. Stenosis grade: The plaque was designed to increase in size in the intima area causing either a 50% or a 75% area stenosis (relative to the assumed normal lumen area).
3. Plaque composition: The plaque was fibrous with increasing lipid content (from 0% to 100%, with 25% increments, see figure 5-2).

A phantom was generated for each varied parameter resulting in 60 phantoms (6 lumen HU values x 2 stenosis grades x 5 plaque contents).

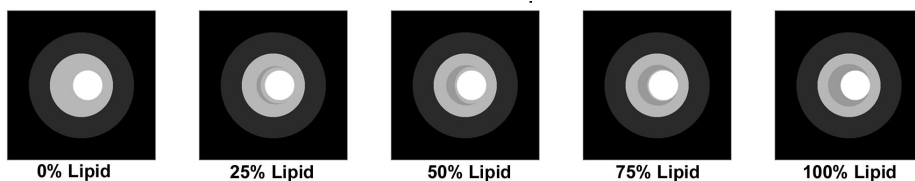


Figure 5-2. Different levels of lipid content of the plaque (from left to right: 0 to 100%, with 25% increment)

Scanning parameters

The simulation used identical scanning parameters as has been previously published elsewhere [20]. The parameters were chosen to mimic the scanning parameter of a 64-MDCT scanner for CT angiography (CTA), but with detector size set to mimic 64-MDCT and MicroCT spatial resolutions, i.e. 0.4 mm and 48 μm , respectively. The 64-MDCT scanner used for reference is a Somatom Sensation 64 (Siemens Medical Solution, Forchheim, Germany). This type of scanner was considered to be an appropriate representative of current clinical CT systems based on its properties and wide-spread use in cardiac imaging. Meanwhile, the MicroCT scanner used for reference is a Siemens MicroCAT II (Siemens Preclinical Solutions, Knoxville, TN).

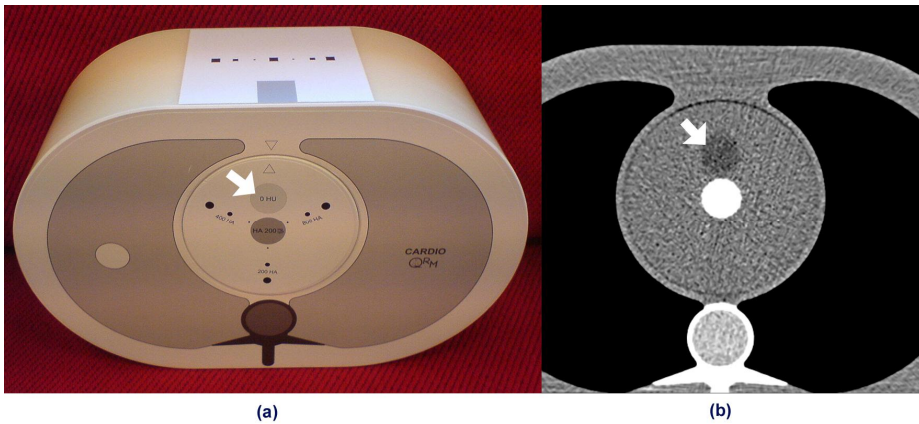


Figure 5-3. QRM Thorax phantom's photograph (a) and CT scan image (b). The arrow indicates the water equivalent insert with attenuation equivalent to water on which an ROI was placed for measuring the noise reference.

Noise addition

The tube current and the scanning environment inside the thorax, two other variables of clinical scans, were indirectly incorporated in the simulation. Both are known to be related to noise, affecting image quality. Artificial noise was incorporated into the simulation using a custom-made Matlab® (Mathworks Inc, Nattick, MA, USA) program according to the method described in a previous publication [31], matching the noise level at normal clinical CT images. The reference for normal clinical CT images was taken from a thorax phantom scan (QRM, Möhrendorf, Germany; figure 5-3) [32], scanned on a 64-MDCT scanner in spiral mode at 120 kV and 770 mAs; reconstructed using B25f kernel at 0.6/0.4 mm slice thickness/interval and 200 mm field of view. The reference noise was defined as the standard deviation inside a region of interest (ROI) over a homogenous area with attenuation equivalent to water (indicated by arrow in figure 5-3), measuring at approximately 19 HU. Several additional noise levels were also simulated to both

modalities, namely at 1/3 and 2/3 of the thorax phantom noise level. Thus, there are three noise levels simulated: 6 HU, 12 HU, and 19 HU, at both modalities. The same noise levels were simulated for both MicroCT and 64-MDCT images.

Reconstruction parameters

The simulation used identical reconstruction parameters as has been previously published elsewhere [20]. The reconstructed image pixel size was set to be 48 μm and 0.4 mm to match the spatial resolution of the MicroCT and 64-MDCT, respectively. The reconstructed images will be regarded as MicroCT and 64-MDCT images, respectively, in the rest of this paper (figure 5-4).

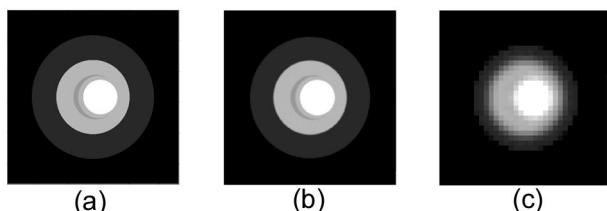


Figure 5-4. The phantom was at 5 μm resolution (a), and reconstructed at MicroCT resolution of 48 μm (b) and 64-MDCT resolution of 0.4mm (c)

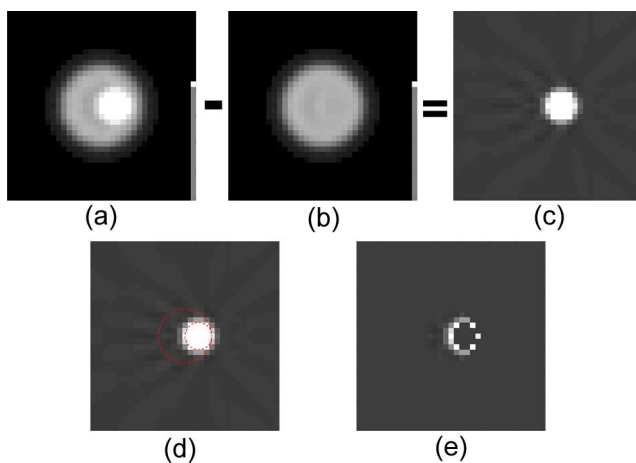


Figure 5-5. Pixel by pixel comparison between contrast-enhanced (a) and non-contrast-enhanced (b) image, resulting in a difference image (c). The same plaque ROI (red dotted lines) used to measure plaque HU-values were applied to the difference image (d), which extract the lumen contrast-enhancement influence on plaque area (e).

Analysis

Analyses were performed using a custom-made Matlab® program and Microsoft Excel 2003 (Microsoft Corp., Redmond, WA, USA). The plaques HU values (mean and standard deviation) were measured inside a region of interest (ROI) which exactly enclosed the plaque region (the crescent-shaped ROI in figure 5-1), as the region was already known from the phantom design. Influences of lumen contrast-enhancement and plaque composition on the plaque HU value were analyzed using linear regression analysis. Separate linear regression analyses for both modalities and stenosis grades were performed to investigate possible interactions of these two variables to the results of the linear regression analysis. The slopes for the two linear regression analysis were calculated,

$$m_1 = \frac{\Delta \text{plaque_mean_value}}{\Delta \text{lumen_mean_value}} \quad (\text{i.e. the change in plaque mean value for every 1 HU}$$

$$\text{change of the lumen mean value) and } m_2 = \frac{\Delta \text{plaque_mean_value}}{\Delta \% \text{lipid_content}} \quad (\text{i.e. the change}$$

in plaque mean value for every 1 % change of the plaque lipid content), for lumen HU values and plaque compositions influence analysis, respectively.

To study the influence of the lumen contrast-enhancement on the plaque HU value in detail, a pixel-by-pixel comparison was performed on the plaque on contrast-enhanced and non-contrast-enhanced images by subtracting the latter from the former, both for MicroCT and 64-MDCT (figure 5-5), resulting in a difference image which precisely extracts the lumen contrast-enhancement influence. As the position of the vessel was fixed during the simulations, the images were perfectly aligned to each other. Identical plaque ROI used to measure plaque HU values were used to delineate the plaque area on the difference image. The HU value of every pixel inside the ROI was extracted and plotted versus its distance from the lumen border. A simple exponential curve ($y = Ae^{-\lambda x} + c$) was fitted to the data points, where A , λ , x , and c indicated the amplitude, coefficient, distance from lumen border, and constant, respectively, using a custom-made Matlab® program which minimizes the squared error between the data points and the approximation curve. A linear regression analysis was also performed to investigate the relationship between the amplitudes and the mean lumen HU values; and between the constants and the mean lumen

$$\text{HU values, with the corresponding slopes: } m_3 = \frac{\Delta \text{Amplitudes}}{\Delta \text{lumen_mean_value}} \quad \text{and}$$

$$m_4 = \frac{\Delta \text{Const}}{\Delta \text{lumen_mean_value}}, \text{ respectively.}$$

All analyses were performed with and without noise incorporated.

Results

No noise

Factors influencing non-calcified plaque visualization

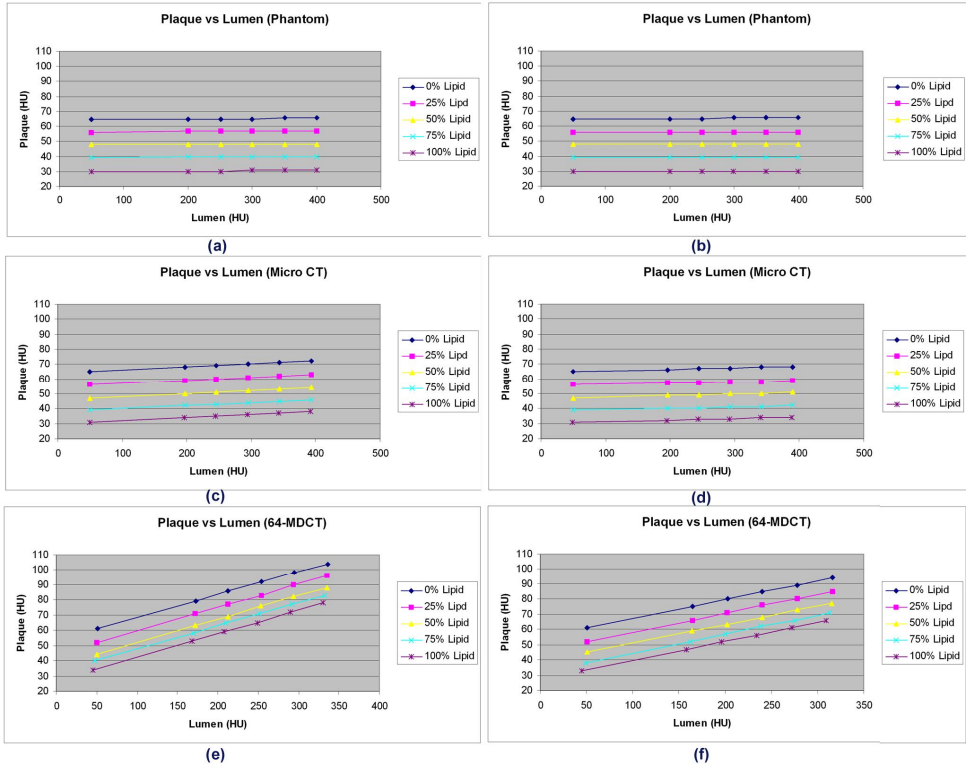


Figure 5-6. Effect of lumen HU values on the plaque HU values at 50% stenosis (a, c, and e) and 75% stenosis (b, d, and f), for phantom images (a and b), MicroCT (c and d), and 64-MDCT (e and f).

In figures 5-6(a) and 5-6(b), the mean HU values of each plaque type at the actual phantom images are shown, for 50% and 75% stenosis, respectively. Investigating the effect of lumen contrast-enhancement on plaque visualization, positive linear correlations ($0.92 < R^2 < 1$) were found between the lumen and the mean plaque HU values (figures 5-6(c) to 5-6(f)). The slopes (m_1) of these positive linear correlations were nearly identical for all plaque lipid contents, but varied slightly with stenosis grades (see table 5-2 – No Noise). Investigating the effect of plaque composition on plaque visualization, negative linear correlations ($0.98 < R^2 < 0.999$) were found between the plaque percentage (%) lipid content

Table 5-2. Linear relationship between plaque mean HU value, lumen mean HU values, and plaque percentage lipid content

Noise Level	uCT				64-MDCT			
	50% Stenosis		75% Stenosis		50% Stenosis		75% Stenosis	
	m_1	m_2	m_1	m_2	m_1	m_2	m_1	m_2
No Noise	0.02 ± 0.00	-0.34 ± 0.00	0.01 ± 0.00	-0.34 ± 0.00	0.15 ± 0.00	-0.26 ± 0.00	0.12 ± 0.00	-0.28 ± 0.01
6 HU Noise	0.02 ± 0.00	-0.34 ± 0.00	0.01 ± 0.00	-0.34 ± 0.00	0.15 ± 0.00	-0.26 ± 0.01	0.12 ± 0.00	-0.28 ± 0.01
12 HU Noise	0.02 ± 0.00	-0.34 ± 0.00	0.01 ± 0.00	-0.34 ± 0.00	0.16 ± 0.00	-0.26 ± 0.02	0.12 ± 0.01	-0.29 ± 0.01
19 HU Noise	0.02 ± 0.00	-0.34 ± 0.01	0.01 ± 0.00	-0.34 ± 0.00	0.16 ± 0.01	-0.29 ± 0.02	0.11 ± 0.00	-0.27 ± 0.01

Note:

1. m_1 : The slope of linear relationship between plaque mean HU value and lumen HU value
2. m_2 : The slope of linear relationship between plaque mean HU value and plaque percentage lipid content

Table 5-3. Lumen influence patterns parameters

Noise Level	MicroCT						64-MDCT					
	50% Stenosis			75% Stenosis			50% Stenosis			75% Stenosis		
	m_3	λ	m_4	m_3	λ	m_4	m_3	λ	m_4	m_3	λ	m_4
No Noise	0.56	1.60 ± 0.00	0.001	0.54	1.63 ± 0.00	0.001	0.62	1.22 ± 0.00	0.05	0.64	1.64 ± 0.00	0.01
6 HU Noise	0.56	1.61 ± 0.03	*	0.53	1.63 ± 0.03	*	0.63	1.14 ± 0.09	0.05^\dagger	0.65	1.71 ± 0.13	*
12 HU Noise	0.55	1.62 ± 0.06	*	0.55	1.63 ± 0.07	*	0.64	1.31 ± 0.17	*	0.67	1.73 ± 0.24	*
19 HU Noise	0.56	1.59 ± 0.1	*	0.54	1.57 ± 0.13	*	0.61	1.29 ± 0.25	*	0.72	1.71 ± 0.26	*

Note:

1. m_3 : The slope of linear relationship between amplitude parameter of the influence patterns and lumen HU value
2. m_4 : The slope of linear relationship between constant parameter of the influence patterns and lumen HU value

and mean HU value. The slopes (m_2) of these negative linear correlations were nearly identical for all lumen HU values (see table 5-2 – No Noise). On non-contrast-enhanced images, all plaques had similar mean HU values (≤ 4 HU difference) as plaques of the same lipid content at the actual phantom images, regardless of the stenosis grade and modality.

Lumen contrast-enhancement influence pattern

In figures 5-7(a) and 5-8(a) the typical results are shown of the pixel by pixel difference in plaques HU values on contrast-enhanced and non-contrast-enhanced MicroCT and 64-MDCT, respectively, versus their distance to the lumen border. In figures 5-7(b) and 5-8(b) the influence patterns at different lumen HU values and stenosis grades are shown. The influence patterns at different plaque lipid contents (with the same lumen HU value and stenosis grade) were identical. The lumen contrast-enhancement influence patterns were similar for the 50% and 75% stenotic plaque with the same lumen HU value (figures 5-7(b) and 5-8(b), for MicroCT and 64-MDCT, respectively). Positive linear correlations ($R^2 = 1$) were found between the amplitudes and lumen HU values (the slopes (m_3) for MicroCT and 64-MDCT are shown in table 5-3 – No Noise). All lambdas (λ) parameters from the influence patterns are closely similar (table 5-3 – No Noise), except for the 50% stenosis 64-MDCT. Positive linear correlations ($R^2 = 1$) were also found between the constants and lumen HU values (the slopes (m_4) for MicroCT and 64-MDCT are shown in table 5-3 – No Noise). However, the slopes were very small (≤ 0.01) for all data, except for the 50% stenosis 64-MDCT. Despite of this deviation, the shape of the lumen influence pattern matched the pattern from the rest of the data (figure 5-8(b)). At approximately 2-pixel radius from the lumen border, the influence patterns reached a relatively neutral level (0 - 7 HU). Outside a 2-pixels radius, the absolute mean difference in the plaque values for the contrast-enhanced (lumen 200-400 HU) versus the non-contrast-enhanced images (lumen 50 HU) was very low (table 5-4 – No Noise) indicating very low influence from the lumen.

Table 5-4. Absolute mean HU values difference of plaques outside 2 pixel radius from the lumen border between contrast-enhanced and non contrast-enhanced images

Noise Level	MicroCT			64CT		
	min	max	median	min	max	median
No Noise	0	0	0	0	5	1
6 HU Noise	0	0	0	0	7	1
12 HU Noise	0	1	0	0	13	3.5
19 HU Noise	0	1	0	0	19	2

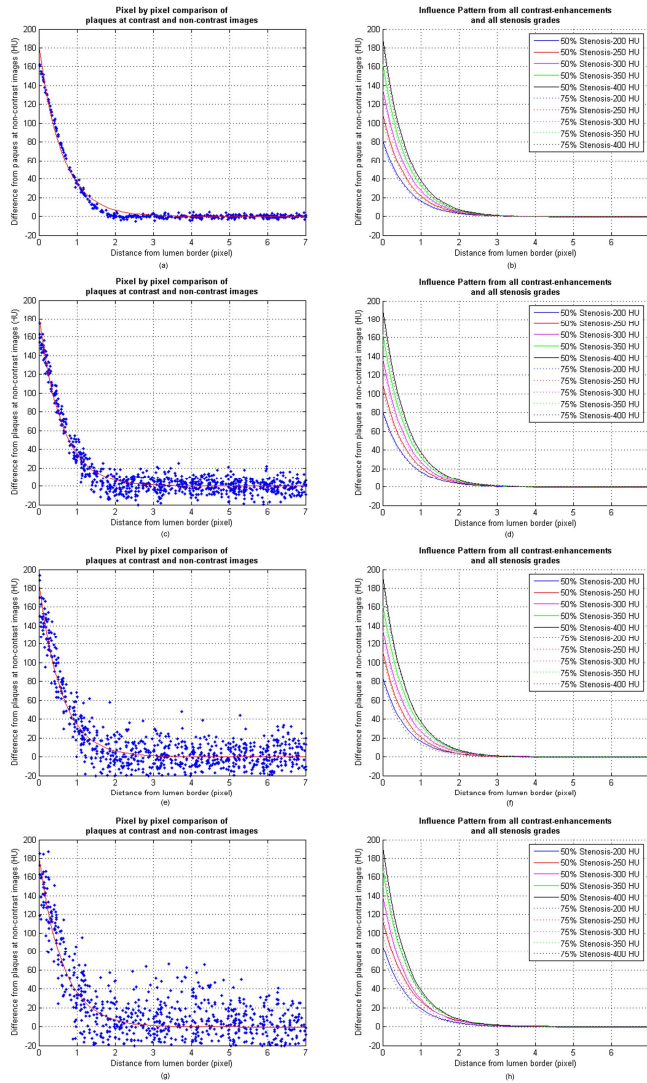


Figure 5-7. The typical lumen influence pattern (from 400 HU lumen in this case) at MicroCT images, which can be approximated with an exponential curve ($y = Ae^{-\lambda x} + C$) (a) and the approximation curves of the influence patterns from all lumen values (b). The pattern for 50% stenosis (solid lines) and 75% stenosis (dotted lines) are close to each other. The amplitudes (A) of the exponential curves were similar for all stenosis grades and modalities. The influence patterns for different plaque contents (with the same lumen HU value and stenosis grade) were almost identical and, therefore, not shown here. Introduction of noise affected the lumen influence patterns, but the patterns remained similar (c-d: 6 HU noise; e-f: 12 HU noise; g-h: 19 HU noise).

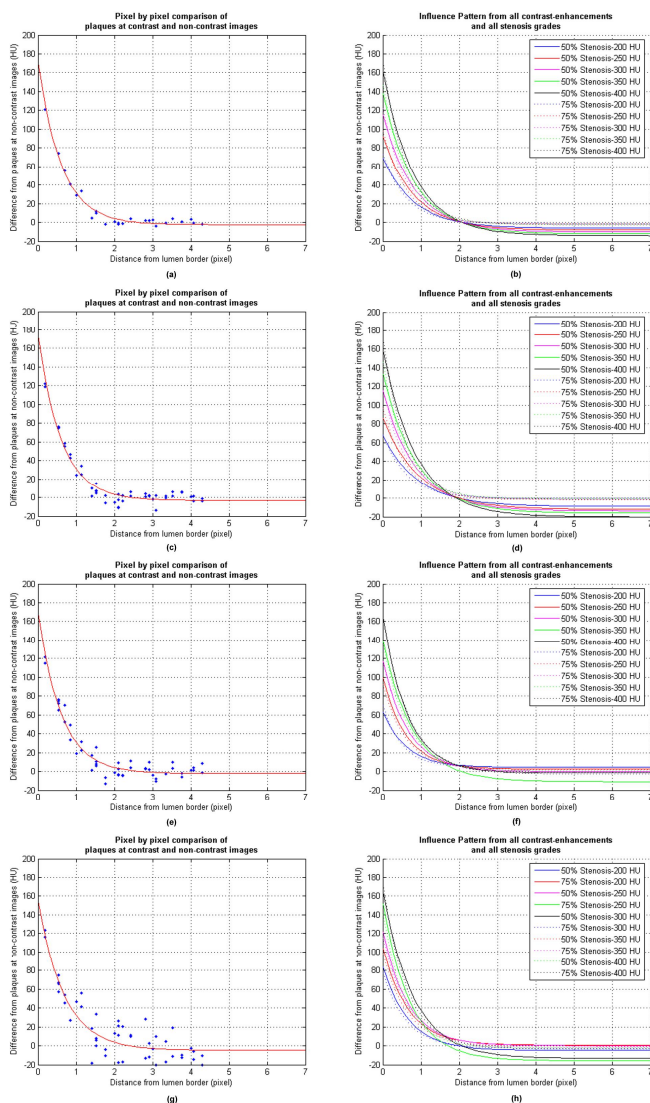


Figure 5-8. The typical lumen influence pattern (from 400 HU lumen in this case) at 64-MDCT images, which can be approximated with an exponential curve ($y = Ae^{-\lambda x} + C$) (a) and the approximation curves of the influence patterns from all lumen values (b). The pattern for 50% stenosis (solid lines) and 75% stenosis (dotted lines) are close to each other. The amplitudes (A) of the exponential curves were similar for all stenosis grades and modalities. The influence patterns for different plaque contents (with the same lumen HU value and stenosis grade) were almost identical and, therefore, not shown here. Introduction of noise affected the lumen influence patterns, but the patterns remained similar (c-d: 6 HU noise; e-f: 12 HU noise; g-h: 19 HU noise).

With noise

Introduction of noise imposed some effects on the non-calcified plaque visualization, but similar results were still found. Compared to when no noise present, slightly weaker positive linear correlations ($0.92 < R^2 < 1$) were found between the lumen and the mean plaque HU values (the slopes (m_1) are shown on table 5-2 – all noise levels). The same effect was also found on the negative linear correlations ($0.87 < R^2 < 0.999$) between the plaque percentage lipid content and mean HU values (the slopes (m_2) are shown on table 5-2 – all noise levels).

The influence patterns were also affected by the presence of noise. Slightly weaker positive linear correlations ($0.94 < r^2 < 0.999$) between the amplitudes and lumen HU values were found (the slopes (m_3) are shown on table 5-3 – all noise levels). The λ s were having more variations as the noise level increased (see the λ s on table 5-3 – all noise levels). Almost all linear correlations were lost between the constants and the lumen HU values. Only the constants from 50% stenosis 64-MDCT still retained small linear correlation ($R^2 = 0.45$). However, the patterns remained similar (figures 5-7(c) – 5-7(h) and figures 5-8(c) – 5-8(h), for MicroCT and 64-MDCT, respectively). Outside a 2-pixels radius, the absolute mean differences of the plaque values between the contrast-enhanced to the non-contrast-enhanced images were still small (see table 5-4 – all noise levels).

Discussion

Lumen contrast-enhancement influence on non-calcified plaque visualization

In this study, the lumen contrast-enhancement was shown to highly influence the non-calcified plaque HU value, similar to findings in earlier publications [16, 33-36]. The partial volume effects (induced by the limited spatial resolution of clinical CT) and the use of smooth reconstruction kernels are the most probable causes of this phenomenon. The proposed exponential decreasing curve was found to fit the lumen contrast-enhancement influence pattern very well. The curve corresponds to one-half of the exponential sigmoid curve. A previous publication has also used the exponential sigmoid curve to describe an image edge model [37]. The extent of the influence of lumen contrast-enhancement on plaque HU value was up to a 2-pixel radius. The observed influence patterns were valid for all investigated cases, regardless of the lumen HU value, stenosis grade, plaque content, and modality/spatial resolution. Small deviation found on 50% 64-MDCT's influence patterns are caused by the lack of pixel data for approximation. Addition of noise to the simulation data resulted in some variations in the found influence patterns. However, the patterns remained the same. The lost of linear correlations between the pattern's constants parameter and lumen HU value after noise introduction is understandable because the slopes were already small to begin with, so that a little amount of noise will already obscured the correlation. Outside a 2-pixel radius, the lumen influence was minimal. Pixel

size is dependent on the spatial resolution of the imaging modality, which means that plaque HU values have to be measured at least 0.8 mm away from the lumen border in case of the 0.4 mm spatial resolution of current clinical CT scanners. This range concurs with a previous report in which plaque measurements at 0.75 mm distance were no longer influenced by the lumen contrast-enhancement [36].

In clinical situations, the exact determination of lumen and outer vessel wall boundary remains challenging. One of the methods which can be used is the one proposed by Brodoefel *et al.* [38]. By using a fixed HU threshold to define the outer wall and the lumen border; and by peeling of 1 outer pixel (corresponds to the thickness of adventitia layer of the simulated vessel in this study), the plaque-burdened intimal area is obtained. Alternatively, a lumen contrast-enhancement dependent threshold may be used instead to determine lumen the border [39]. The size of the simulated vessel corresponded to the proximal part of the coronary tree. The 2-pixel lumen influence radius has been shown to be independent of the simulated lumen size. Moreover, the analysis was focused to the intimal part and excluding the outer layer of the plaque, which was affected by partial volume effect with the surrounding. As the vessel grows smaller to the distal part, the inner area of the plaque influenced by the lumen and the outer area blurred by partial volume effect with the surrounding became even more prominent, making it even harder to characterize the plaque. However, the distal part was less likely to contain rupture-prone plaque than the proximal part [40], which make it relatively less urgent for plaque characterization.

Lipid-content fraction effect on non-calcified plaque visualization

The strict binary classification of the plaque area inside the measurement ROI as either fibrous or lipid-rich might cause some problems due to the plaque heterogeneities inside the ROI [41]. Furthermore, Wintermark, *et al.* [30] stated that for carotid plaques a minimum size of 5 pixels is needed to ensure excellent detection of the lipid pool, which would be a relatively large size in the much smaller coronary arteries. The simulation result has shown that the mean HU value of the plaques was linearly correlated with their % lipid content. A recent study on coronary CT angiography scans of patients has also shown similar linear relationship, but with a rather weak correlation [42]. Plaque vulnerability is defined by its % necrotic core (lipid) [12], and thus direct determination of plaque % lipid-content based on its HU value might serve as an alternative for plaque characterization. However, this method is still inapplicable due to many inherent limitations. On the simulated non-contrast-enhanced images, the HU values of each lipid content were relatively stable regardless of the stenosis grade and modality. However, on the contrast-enhanced images, the plaques HU values were highly influenced by the contrast-enhancement. The simulation result has shown that the lumen influence is limited to 2-pixel radius from the lumen border. However, to entirely ignore the part of the plaque located inside the 2-pixels radius would be unwise as the vulnerable plaques might be located close

to lumen border, such as the thin-capped fibroatheroma [10]. Another limitation to this method is the possible presence of other plaque component besides fibrous and lipid, *e.g.* microcalcifications [43] and hemorrhage [30] that may affect the plaque HU value.

Limitation of the study

The limitation of this study lies in the nature of the simulation design. Despite the efforts to mimic actual CT scanning parameters, several aspects can only be approximated. Furthermore, images were stationary, while in clinical situations, not all CT scans will show motion-free depiction of the coronary arteries. Due to the limitation of the simulation software, beam hardening and x-ray scattering were not incorporated into the simulation. Both artifacts may introduce non-linear errors in the CT numbers. However, both the effects of beam hardening [44] and scattering [45] are mainly pronounced as a streak artifact in the path between two high attenuating objects. It has been shown that there is no or minimal streak artifact on the tissue next to contrast-enhanced cavity when there is no high attenuating object next to it [44]. Since there was no other object around the simulated vessel in this study, minimal effects to the results are thought to arise from these artifacts. The simulation software failed also to simulate a cone beam x-ray projections and the analysis was limited to two dimensional images. Scanning using a cone beam x-ray may introduce artifacts due to misregistration of projection data, especially to the off-axis object. However, the simulated vessel was located at the center of the image where there should have been minimal cone beam artifact. Meanwhile, vessel wall analysis is commonly performed based on cross sectional view of the coronary on CT angiography examinations [46]. The visualization of the simulated vessel was specifically chosen to show this representation. Despite the limitations, this software phantom study offers some unique advantages. Visualization in CTA datasets can be individually assessed by eliminating the interference motion artifacts; and by a controlled construction of the phantom, influencing factors in atherosclerotic plaque can be investigated.

Positive remodeling of coronary plaque has been associated with a lower attenuation value, indicating more lipid-rich content [47]. The simulated plaque-burdened vessels in this study did not explicitly take into account this relationship between plaque composition and type of remodeling. Instead, the vessels directly simulate different levels of lipid content of the plaque, which is the main interest for plaque classification. Moreover, this study showed that the lumen contrast-enhancement influence was only dependent on the distance from the lumen border, and thus independent of the morphology of the lumen, plaque, vessel and plaque compositions.

Future work

The finding that lumen contrast-enhancement influence follows a specific exponential pattern, which depends only to the lumen contrast-enhancement value and the distance to the lumen border, indicated that it might be feasible to construct a lumen

influence correction algorithm. Further validations are still needed in future studies involving hardware phantom studies, ex-vivo specimen, and finally clinical validation.

Conclusion

To avoid lumen contrast-enhancement influence, plaques must be measured outside 2-pixel radius from the lumen border, which corresponds to 0.8 mm for current clinical CT systems. Based on the patterns found, a lumen influence correction algorithm may be developed. HU-based plaque percentage lipid-content determination might serve as an alternative plaque characterization method. However, its applicability is still hindered by many inherent limitations.

Acknowledgement

The authors would like to acknowledge the contribution of Arjen van Hulzen, Hildebrand Dijkstra, and Wim Tukker for their advice and assistance regarding noise simulation; and Estelle Noach for providing extensive remarks on the manuscript.

References

- [1] Leber AW, Johnson T, Becker A, et al. Diagnostic accuracy of dual-source multi-slice CT-coronary angiography in patients with an intermediate pretest likelihood for coronary artery disease. *Eur Heart J* 2007; 28:2354-60
- [2] Nieman K, Oudkerk M, Rensing BJ, et al. Coronary angiography with multi-slice computed tomography. *The Lancet* 2001; 357:599-603
- [3] Agatston AS, Janowitz WR, Hildner FJ, et al. Quantification of coronary artery calcium using ultrafast computed tomography. *J Am Coll Cardiol* 1990; 15:827-32
- [4] Rumberger JA, Simons DB, Fitzpatrick LA, Sheedy PF, Schwartz RS. Coronary artery calcium area by electron-beam computed tomography and coronary atherosclerotic plaque area. A histopathologic correlative study. *Circulation* 1995; 92:2157-62
- [5] Oudkerk M, Stillman AE, Halliburton SS, et al. Coronary artery calcium screening: current status and recommendations from the European Society of Cardiac Radiology and North American Society for Cardiovascular Imaging. *Int J Cardiovasc Imaging* 2008; 24:645-71
- [6] Arad Y, Goodman KJ, Roth M, Newstein D, Guerci AD. Coronary calcification, coronary disease risk factors, C-reactive protein, and atherosclerotic cardiovascular disease events the St. Francis Heart Study. *J Am Coll Cardiol* 2005; 46:158-65

- [7] Greenland P, LaBree L, Azen SP, Doherty TM, Detrano RC. Coronary artery calcium score combined with Framingham score for risk prediction in asymptomatic individuals. *Jama* 2004; 291:210-5
- [8] Vliedenthart R, Oudkerk M, Hofman A, et al. Coronary calcification improves cardiovascular risk prediction in the elderly. *Circulation* 2005; 112:572
- [9] Rumberger JA, Schwartz RS, Simons DB, et al. Relation of coronary calcium determined by electron beam computed tomography and lumen narrowing determined by autopsy. *Am J Cardiol* 1994; 73:1169
- [10] Burke AP, Farb A, Malcom GT, et al. Coronary risk factors and plaque morphology in men with coronary disease who died suddenly. *N Engl J Med* 1997; 336:1276-82
- [11] Libby P. Molecular bases of the acute coronary syndromes. *Circulation* 1995; 91:2844
- [12] Virmani R, Burke AP, Farb A, Kolodgie FD. Pathology of the vulnerable plaque. *J Am Coll Cardiol* 2006; 47:13-8
- [13] Becker CR, Nikolaou K, Muders M, et al. Ex vivo coronary atherosclerotic plaque characterization with multi-detector-row CT. *Eur Radiol* 2003; 13:2094-8
- [14] Pohle K, Achenbach S, MacNeill B, et al. Characterization of non-calcified coronary atherosclerotic plaque by multi-detector row CT: Comparison to IVUS. *Atherosclerosis* 2007; 190:174-80
- [15] Schroeder S, Kuettner A, Wojak T, et al. Non-invasive evaluation of atherosclerosis with contrast enhanced 16 slice spiral computed tomography: results of ex vivo investigations. *Heart* 2004; 90:1471-5
- [16] Cademartiri F, Mollet NR, Runza G, et al. Influence of intracoronary attenuation on coronary plaque measurements using multislice computed tomography: observations in an ex vivo model of coronary computed tomography angiography. *Eur Radiol* 2005; 15:1426-31
- [17] Ferencik M, Chan RC, Achenbach S, et al. Arterial wall imaging: evaluation with 16-section multidetector CT in blood vessel phantoms and ex vivo coronary arteries. *Radiology* 2006; 240:708-16
- [18] Rosenberg K. CTSim-The Open Source Computed Tomography Simulator. URL <http://www.ctsim.org/> [accessed 14 May 2009] 2001;
- [19] Zbijewski W, Beekman FJ. Comparison of methods for suppressing edge and aliasing artefacts in iterative x-ray CT reconstruction. *Phys Med Biol* 2006; 51:1877
- [20] Kristanto W, Ooijen PMA, Groen JM, Vliedenthart R, Oudkerk M. Small calcified coronary atherosclerotic plaque simulation model: minimal size and attenuation detectable by 64-MDCT and MicroCT. *Int J Cardiovasc Imaging* 2012; 28:843-53
- [21] Olszewski ME, Wahle A, Khullar D, Subramanyan K, Sonka M. A study investigating automated quantitative analyses of coronary multidetector computed tomography images. *Proceedings of SPIE* 2005; 5746:214

- [22] Berglund H, Luo H, Nishioka T, et al. Highly localized arterial remodeling in patients with coronary atherosclerosis: an intravascular ultrasound study. *Circulation* 1997; 96:1470-6
- [23] de Weert TT, Ouhlous M, Meijering E, et al. In vivo characterization and quantification of atherosclerotic carotid plaque components with multidetector computed tomography and histopathological correlation. *Arterioscler Thromb Vasc Biol* 2006; 26:2366-72
- [24] Gorter PM, van Lindert ASR, de Vos AM, et al. Quantification of epicardial and peri-coronary fat using cardiac computed tomography; reproducibility and relation with obesity and metabolic syndrome in patients suspected of coronary artery disease. *Atherosclerosis* 2008; 197:896-903
- [25] Gradus-Pizlo I, Bigelow B, Mahomed Y, et al. Left anterior descending coronary artery wall thickness measured by high-frequency transthoracic and epicardial echocardiography includes adventitia. *Am J Cardiol* 2003; 91:27-32
- [26] Haraguchi K, Houkin K, Koyanagi I, Nonaka T, Baba T. Evaluation of carotid plaque composition by computed tomographic angiography and black blood magnetic resonance images. *Minim Invasive Neurosurg* 2008; 51:91-4
- [27] Noguchi K, Seto H, Kamisaki Y, et al. Comparison of fluid-attenuated inversion-recovery MR imaging with CT in a simulated model of acute subarachnoid hemorrhage. *Am J Neuroradiol* 2000; 21:923-7
- [28] Walker LJ, Ismail A, McMeekin W, et al. Computed tomography angiography for the evaluation of carotid atherosclerotic plaque: correlation with histopathology of endarterectomy specimens. *Stroke* 2002; 33:977-81
- [29] Wheeler GL, Shi R, Beck SR, et al. Pericardial and Visceral Adipose Tissues Measured Volumetrically With Computed Tomography Are Highly Associated in Type 2 Diabetic Families. *Invest Radiol* 2005; 40:97
- [30] Wintermark M, Jawadi SS, Rapp JH, et al. High-resolution CT imaging of carotid artery atherosclerotic plaques. *Am J Neuroradiol* 2008; 29:875-82
- [31] Joemai RMS, Geleijns J, Veldkamp WJH. Development and validation of a low dose simulator for computed tomography. *Eur Radiol* 2010; 20:958-66
- [32] Wirth S, Korner M, Treitl M, et al. Computed tomography during cardiopulmonary resuscitation using automated chest compression devices - an initial study. *Eur Radiol* 2009; 19:1857-66
- [33] Fei X, Du X, Yang Q, et al. 64-MDCT Coronary Angiography: Phantom Study of Effects of Vascular Attenuation on Detection of Coronary Stenosis. *Am J Roentgenol* 2008; 191:43-9
- [34] Halliburton SS, Schoenhagen P, Nair A, et al. Contrast enhancement of coronary atherosclerotic plaque: a high-resolution, multidetector-row computed tomography study of pressure-perfused, human ex-vivo coronary arteries. *Coron Artery Dis* 2006; 17:553-60

- [35] Horiguchi J, Fujioka C, Kiguchi M, et al. Soft and intermediate plaques in coronary arteries: how accurately can we measure CT attenuation using 64-MDCT? *Am J Roentgenol* 2007; 189:981-8
- [36] Suzuki S, Furui S, Kuwahara S, et al. Accuracy of attenuation measurement of vascular wall in vitro on computed tomography angiography: Effect of wall thickness, density of contrast medium, and measurement point. *Invest Radiol* 2006; 41:510-5
- [37] Olsen S, Gooch B *Image Simplifications and Vectorization*. In: Spencer SN (ed) *Non-Photorealistic Animation and Rendering* 2011. New York: ACM, (2011): pp 65-74
- [38] Brodoefel H, Burgstahler C, Sabir A, et al. Coronary Plaque Quantification by Voxel Analysis: Dual-Source MDCT Angiography Versus Intravascular Sonography. *Am J Roentgenol* 2009; 192:84-9
- [39] Shimamoto R, Suzuki J, Yamazaki T, et al. A new method for measuring coronary artery diameters with CT spatial profile curves. *Radiography* 2007; 13:44-50
- [40] Valgimigli M, Rodriguez-Granillo GA, Garcia-Garcia HM, et al. Plaque Composition in the Left Main Stem Mimics the Distal But Not the Proximal Tract of the Left Coronary Artery. *J Am Coll Cardiol* 2007; 49:23-31
- [41] Foster G, Shah H, Sarraf G, Ahmadi N, Budoff M. Detection of noncalcified and mixed plaque by multirow detector computed tomography. *Expert Rev Cardiovasc Ther* 2009; 7:57-64
- [42] Utsunomiya H, Hara H, Moroi M, Sugi K, Nakamura Y. Relationship between tissue characterization with 40MHz intravascular ultrasound imaging and 64-slice computed tomography. *J Cardiol* 2011; 57:297-302
- [43] Vengrenyuk Y, Carlier S, Xanthos S, et al. A hypothesis for vulnerable plaque rupture due to stress-induced debonding around cellular microcalcifications in thin fibrous caps. *Proc Natl Acad Sci U S A* 2006; 103:14678-83
- [44] Kitagawa K, George RT, Arbab-Zadeh A, Lima JAC, Lardo AC. Characterization and Correction of Beam-hardening Artifacts during Dynamic Volume CT Assessment of Myocardial Perfusion. *Radiology* 2010; 256:111-8
- [45] Joseph PM, Spital RD. The effects of scatter in x-ray computed tomography. *Med Phys* 1982; 9:464-72
- [46] Achenbach S, Ropers D, Hoffmann U, et al. Assessment of coronary remodeling in stenotic and nonstenotic coronary atherosclerotic lesions by multidetector spiral computed tomography. *Journal of the American College of Cardiology* 2004; 43:842-7
- [47] Schmid M, Pfloderer T, Jang IK, et al. Relationship between degree of remodeling and CT attenuation of plaque in coronary atherosclerotic lesions: An in-vivo analysis by multi-detector computed tomography. *Atherosclerosis* 2008; 197:457-64

Chapter 6

**Non-calcified coronary atherosclerotic
plaque visualization on CT:
Correction of lumen contrast-enhancement
influence**

Manuscript in preparation

W. Kristanto, P.M.A. van Ooijen, R. Vliegenthart, and M. Oudkerk

Abstract

Lumen contrast-enhancement influences non-calcified atherosclerotic plaque Hounsfield-Unit (HU) values in computed tomography (CT). This study aimed to construct and validate an algorithm to correct for this influence. Three coronary vessel phantoms with 1, 2, and 4mm circular hollow lumina; with normal and plaque-infested walls were scanned simultaneously in oil using a dual-source CT scanner. Scanning was repeated as the lumina were alternately filled with water and 4 contrast solutions (100-400HU, at 100HU interval). Images were reconstructed at 0.4mm x-y pixel size. The HU-values for wall and lumen were positively linearly correlated, with approximately the same gradients for both normal and plaque-infested walls. Pixel-by-pixel comparisons of contrast-enhanced and non-contrast-enhanced images confirmed exponential declining patterns in lumen contrast-enhancement influence on wall HU-values from the lumen border ($y=Ae^{-\lambda x}+c$). The median difference of the inside and outside 2-pixel radius part of the wall to the reference (non-contrast-enhanced images) was 45HU and 2HU, respectively. Based on the lumen contrast-enhancement influence patterns, a generalized correction algorithm was formulated. Application of the generalized correction algorithm to the inside 2-pixel radius part of the wall reduced the median difference to the reference to 4HU. With this correction, a more accurate determination of vessel wall composition can be made.

Introduction

In coronary artery disease (CAD) is), atherosclerotic plaque develops in the wall of the coronary artery, potentially leading to significant narrowing of the lumen and/or occlusion, hindering the blood supply of the heart muscle. An acute coronary syndrome (ACS) as a result of CAD is currently the leading cause of death in the western world [1]. Early detection of CAD is essential in order to start treatment timely and prevent or delay the progress of the disease. Previous publications demonstrated that coronary stenosis [2, 3] and calcified plaque burden [4-6], two main parameters for estimating CAD event risk, can be quantified reliably by multi detector-row computed tomography (MDCT).

Quantification of non-calcified plaques is of increasing interest in diagnosis and clinical workup as plaques with large lipid-rich components are considered to be more rupture prone and subsequently are more likely to cause an ACS [7]. MDCT can reportedly characterize non-calcified plaques by virtue of their specific CT density in Hounsfield Units (HU) [8-11]. However, to use a generalized HU-criterion is not yet possible as the reported HU-values vary considerably. Many factors have been reported to influence non-calcified coronary plaque HU values, one of the most prominent being the lumen contrast-enhancement [12-16]. In a preliminary software phantom simulation study, the lumen contrast-enhancement was shown to influence the surrounding coronary wall with a specific pattern [17]. This vessel phantom study aimed to construct and validate an algorithm to correct for the lumen contrast-enhancement influence in order to obtain the correct HU values for the characterization of non-calcified plaques.

Material and methods

Phantom experiment

Three coronary vessel phantoms with 1, 2, and 4 mm diameter circular hollow lumina were used in the experiment. The vessel wall was designed to be 35 HU in CT density and 3 mm in thickness, and part of each vessel phantom was infested with an artificial plaque of -10 HU in CT density, 2 mm in thickness, and 5 mm in length (figure 6-1A, these 2 different segments of the wall will be referred to as normal and plaque-infested wall, respectively, for the remainder of the article).

The phantoms were scanned simultaneously while submerged in sun flower oil with a dual-source computed tomography scanner (Siemens Definition, Siemens Medical Solution, Forchheim, Germany) at 120kV, 300mAs/rot, and 64x0.6mm (figure 6-1B). Scanning was performed five times with the lumen alternately filled with water and 4 contrast solutions of approximately 100, 200, 300, and 400 HU. Images were reconstructed at 0.6 mm slice thickness with 0.4 mm increment.

In total, 30 datasets were obtained with the following properties: 3 lumen sizes (1, 2, and 4 mm diameter) x 2 wall types (normal and plaque-infested wall) x 5 lumen contents (water or 1 of the 4 different contrast solutions).

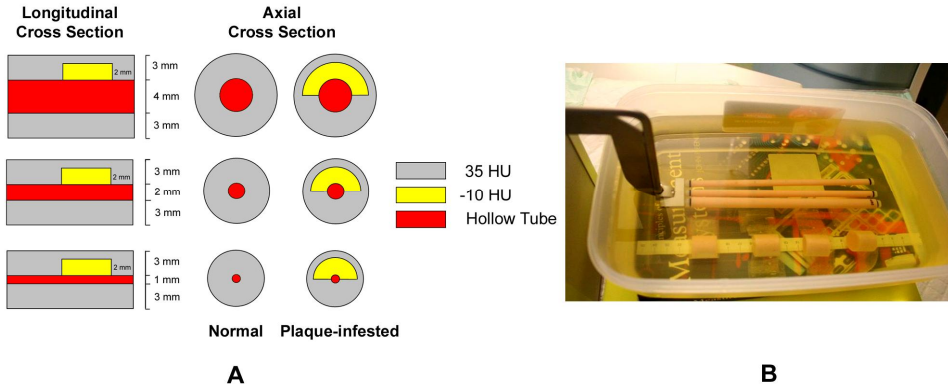


Figure 6-1. The phantom diagram (A) and experimental setup (B).

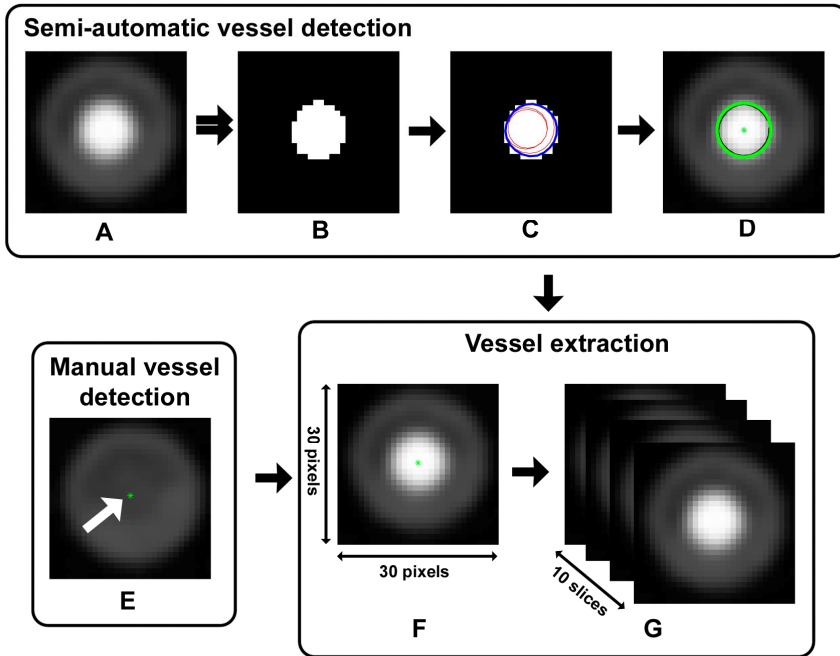


Figure 6-2. Vessel segmentation algorithm. The semi-automatic algorithm was performed by selecting the original image (A), thresholding [28] the image (B), applying a gradient vector flow snake algorithm [29] (red and blue lines) to segment the lumen contour (C), and finally fitting a circle (green circle, centered at the green asterisk) to the obtained contour (D). The manual vessel segmentation (E) was started by selecting the approximate center of the vessel (green asterisk). The vessel was segmented inside an ROI of 30 by 30 pixels (F) around the center (green asterisks on D and E) of the vessels and the process was repeated to the next slice for in total 10 times (G).

Analysis

The images were analyzed using a custom-made software tool written in Matlab® (Mathworks Inc, USA). The following analyses were performed.

1. Vessel segmentation

The vessel was first detected semi-automatically using an algorithm used in a previous publication [18]. The algorithm was finalized by fitting the lumen boundary with a circle of its designed true size, obtaining the center of the vessel (figure 6-2A-D). When the semi-automatic detection was not possible, detection was performed by manually selecting the approximate center of the vessel (figure 6-2E). The vessel was segmented inside a square region of interest (ROI) of 30 by 30 pixels around the center of the vessel (figure 6-2F).

Each plaque was visible on 12 to 13 axial image slices, from which the middle 10 slices were selected to construct a plaque-infested vessel dataset (figure 6-2G). A normal vessel dataset was also constructed similarly by obtaining 10 consecutive slices from the normal part of the same vessel (figure 6-2G).

A training set was constructed by averaging the 10 selected slices for every dataset in order to minimize noise. This training set was then used to study the correlation between HU values of wall and lumen; and to extract the lumen contrast-enhancement influence pattern.

Additionally, a validation set was constructed by arbitrarily selecting one of the 10 slices in each dataset. The validation set was used to apply and test the formulated lumen contrast-enhancement influence correction algorithm (see Validation section).

2. Wall and lumen HU value measurement

Lumen and wall (normal and plaque-infested) HU-values were measured inside ROIs that matched the designed morphology. Since the vessel images underwent preprocessing steps (averaging and alignment), the lumen needed to be segmented again, using the same method as described in the previous step. Manual adjustments were performed when necessary. The wall ROI was defined as the area between the lumen circular ROI and a larger circle with the same axis and a diameter conforming to the designed plaque thickness. The wall ROI left out the outer part of the wall which is blurred by the partial volume averaging with the surrounding. The relation between wall and lumen HU-values was investigated using linear regression analysis. The squared correlation coefficient (r^2) and gradient of the relation were obtained.

3. Lumen contrast-enhancement influence pattern

Pixel by pixel comparisons were performed between contrast-enhanced images (of lumen CT density: 100, 200, 300, and 400 HU) and non-contrast-enhanced images (of lumen CT density: 0 HU) by first aligning both images based on their outer vessel contour (obtained by 0 HU threshold [19]) and then subtracting the latter from the former (figure 6-3). The comparisons resulted in difference images containing only the contribution of the contrast to the image (figure 6-3C). The wall ROI from the previous step was used to delineate the wall area of the difference image (figure 6-3D) and extract the contribution of the contrast to the wall area (figure 6-3E). The value of every pixel inside this ROI was plotted against its distance from the lumen border. An exponential line ($y = Ae^{-\lambda x} + c$) was fitted through the data points, with A , λ , x , and c indicating the amplitude, coefficient, distance from lumen border, and constant, respectively, using a custom made Matlab® program which minimizes the squared error between the data points and the approximation line.

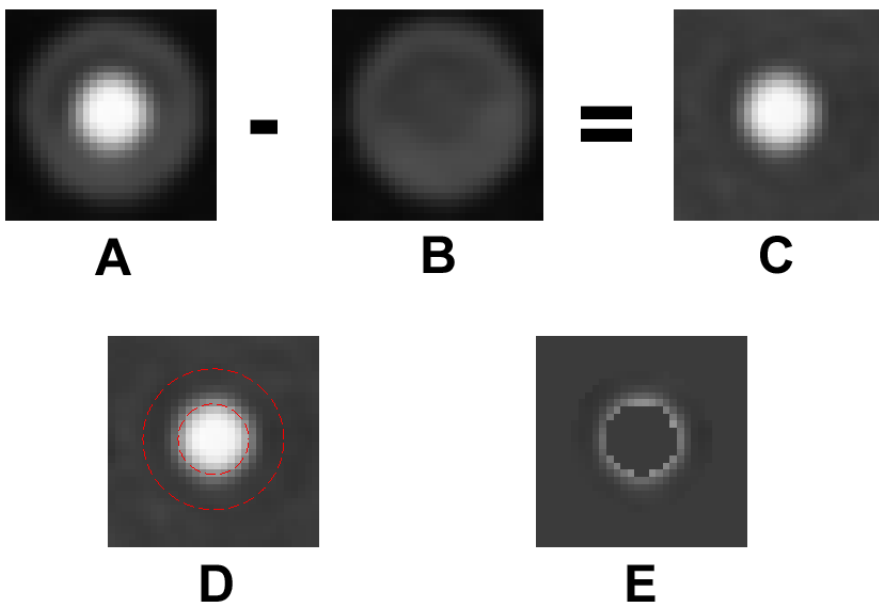


Figure 6-3. Pixel by pixel comparison between contrast-enhanced image (A) and non-contrast-enhanced image (B) by subtracting the latter from the former, resulting in a difference image (C). The wall ROI (striped red line) was overlaid onto the difference image (D), from which the lumen contrast-enhancement influence on the wall was extracted (E).

Validation

In a previous study using software phantoms, it was demonstrated that the lumen contrast-enhancement influences the surrounding wall HU values up to a 2-pixel radius from the lumen border. [17] Therefore, the obtained lumen contrast-enhancement influence lines were applied to the contrast-enhanced image to correct for the lumen contrast-enhancement influence on the surrounding wall up to a 2-pixel radius from the lumen border.

Non-contrast enhanced images of each vessel and wall type were defined as the reference images. The wall HU-values outside the 2-pixel radius were compared between contrast-enhanced images and the reference to check the validity of selecting only inside the 2-pixel radius for applying the correction algorithm. Subsequently, the wall HU-values for the inside 2-pixel radius and for the whole plaque, were compared to the reference, before and after correction.

Results

Wall and lumen HU value measurement

Positive linear correlations between HU values of wall and lumen were found. The gradients were similar for both normal and plaque-infested walls (figure 6-4).

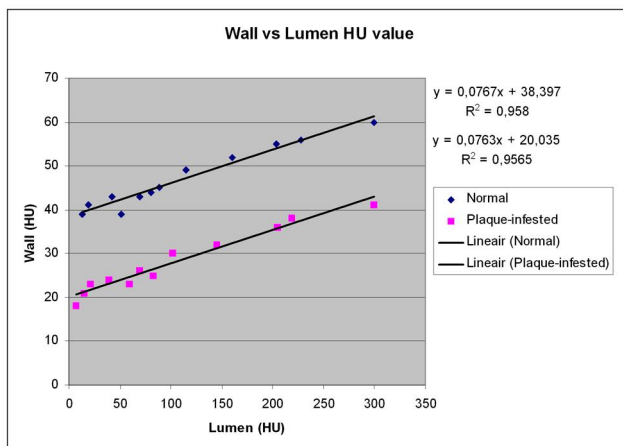


Figure 6-4. The correlation between the wall and lumen mean HU values.

Lumen contrast-enhancement influence pattern

An exponential line ($y = Ae^{-\lambda x} + c$) approximated the lumen contrast-enhancement influence on the surrounding wall (figure 6-5). The lumen contrast-enhancement influence patterns for the two types of wall were similar for each vessel type, except for the smallest vessel (figure 6-6).

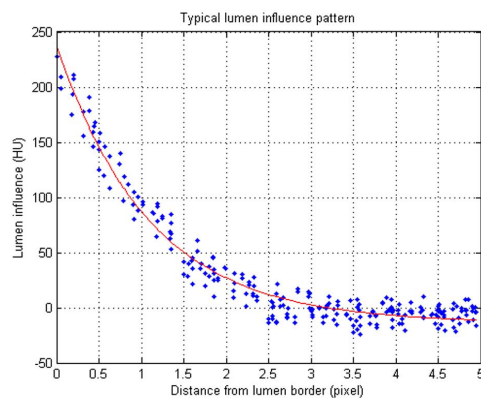


Figure 6-5. Typical lumen contrast-enhancement influence on the surrounding wall, plotted against the distance to the lumen border (blue dots), which was approximated by an exponential line (red line).

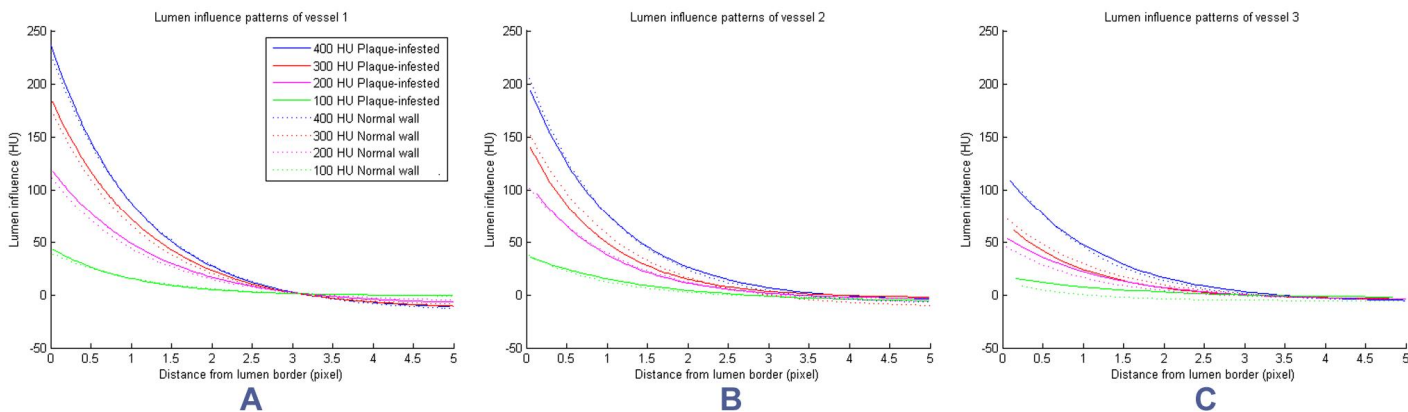


Figure 6-6. The lumen contrast-enhancement influence patterns for large (A), medium (B), and small (C) vessels.

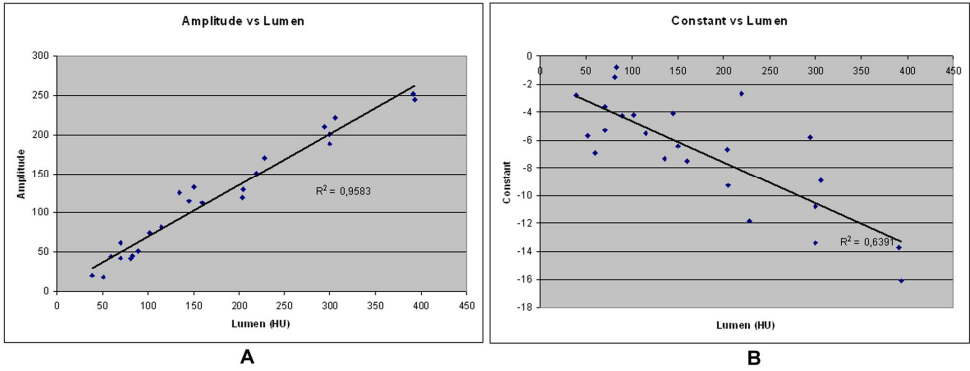


Figure 6-7. The correlation between the amplitudes (A) and the lumen mean HU values and between the constants (B) and the lumen mean HU values

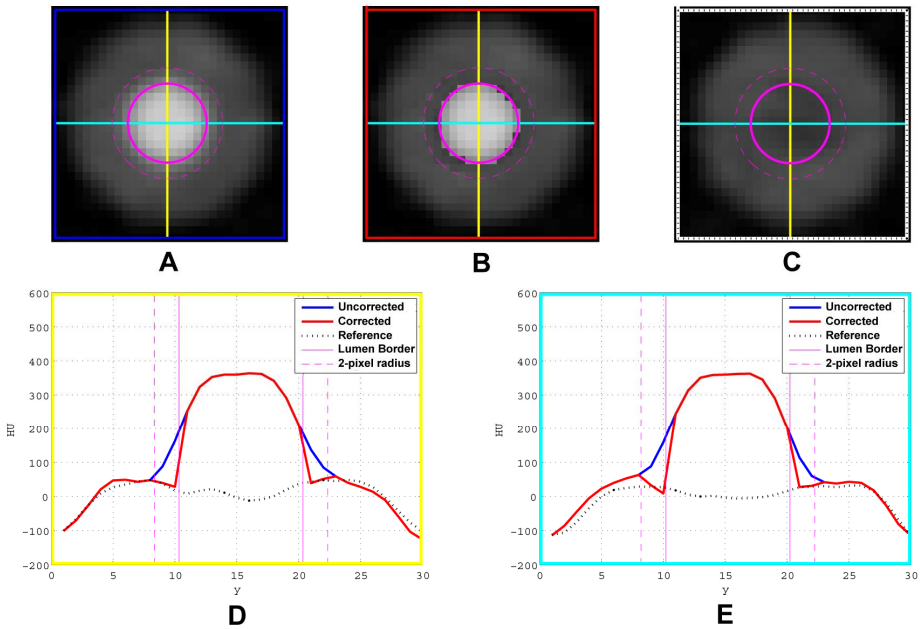


Figure 6-8. The effect of the formulated correction algorithm on the normal wall. This figure shows the uncorrected contrast-enhanced image (A), the corrected contrast-enhanced image (B), and the non-contrast-enhanced reference image (C). The lumen border is shown by the solid magenta circle, and the 2-pixel radius by the striped magenta circle. The HU profiles along the vertical (yellow lines) and horizontal (cyan lines) directions of the three images are plotted on top of each other in image D and E, respectively.

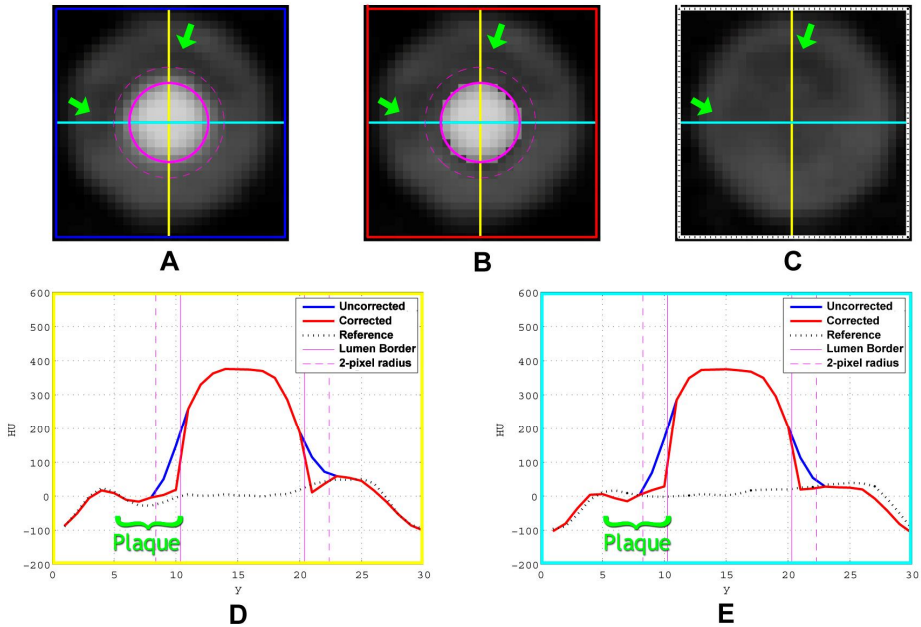


Figure 6-9. The effect of the formulated correction algorithm on the plaque-infested wall.

This figure shows the uncorrected contrast-enhanced image (A), the corrected contrast-enhanced image (B), and the non-contrast-enhanced reference image (C). The lumen border is shown by the solid magenta circle, and the 2-pixel radius by the striped magenta circle. The HU profiles along the vertical (yellow lines) and horizontal (cyan lines) directions of the three images are plotted on top of each other in image D and E, respectively. The range of the plaque infestation is marked by the green arrows on image A, B, and C; and by the green text in image D and E.

The obtained influence patterns (figure 6-6) were applied to the training set to correct for the lumen contrast-enhancement influence. The difference between the mean HU-values of the wall to the reference, before and after correction, can be seen at table 6-1 (training set).

Generalized lumen contrast-enhancement influence pattern

To enhance the applicability of the lumen contrast-enhancement influence pattern, a generalized form of the correction algorithm was formulated. Combining all the parameters of the exponential lines from all vessels and all types of wall, the amplitudes (A) were found to be linearly correlated to the mean lumen HU-values ($r^2 = 0.96$), following a linear equation: $A = 0.66 * Lumen_HU + 4$ (figure 6-7A). Meanwhile, the coefficients (λ) were similar: 0.9 ± 0.1 , and the constants (c) were linearly correlated to the

mean lumen HU values ($r^2 = 0.64$), following a linear equation: $c = -0.03 * Lumen_HU - 2$ (figure 6-7B).

The generalized correction algorithms were applied to the validation set to correct for the lumen contrast-enhancement influence (figure 6-8 and 6-9). The differences of the walls mean HU-values to the reference, before and after correction, can be seen at table 6-1 (validation set).

Table 6-1. The difference of walls mean HU-values to the reference

Set	Part of the wall Measured	Difference to Reference	
		No Correction	Correction
Training	Outside 2-pixel radius	0-7 HU (2 HU)	NC
	Inside 2-pixel radius	0-95 HU (44 HU)	0-6 HU (1 HU)
	Whole wall	1-30 HU (11 HU)	0-4 HU (1 HU)
Validation	Outside 2-pixel radius	0-8 (2 HU)	NC
	Inside 2-pixel radius	4-98 HU (45 HU)	0-15 HU (4 HU)
	Whole wall	1-30 HU (10 HU)	0-8 HU (2 HU)

Note:

1. The values on Difference to Reference columns indicate the range with the median in the bracket
2. NC: no correction performed

Discussion

The increasing interest to characterize non-calcified plaque content originates from the assumption that plaques with a large lipid-rich component are more likely to rupture which in turn causes an ACS [7]. One of the most common and most validated methods to identify and quantify lipid-rich plaque is intravascular ultrasound [20, 21]. However, identification of lipid-rich plaque using MDCT is highly preferable because of its non-invasive nature.

Many studies have reported that types of non-calcified plaques can be distinguished based on CT attenuation [11, 22-24]. However many factors have been reported that influence the HU values of plaques [12, 25, 26], with lumen contrast-enhancement being the most prominent one. Previous studies showed that the influence was dependent on the location of plaque relative to lumen [15, 16], with stronger influence on CT attenuation of non-calcified plaque close to the lumen. Confirming the findings initially shown in software simulations [17] the exact pattern of the lumen contrast-enhancement influence was reproduced and validated in this study as being most severe close to the lumen border and decreasing following a specific exponential pattern until a 2-pixel radius from the lumen border. The amplitudes determine the magnitude of the exponential pattern. The strong positive linear correlation to the lumen HU values can be explained by the fact

that CT is a linear system. The lambda coefficients express the range of the exponential pattern. The fact that they are relatively stable confirms that the influence range is mostly dependent on the spatial resolution of the CT system. The negative linear correlation between the constants and the lumen HU-values may first seem counter intuitive as this will decrease the influence as the lumen HU values increase. This finding may be due to the Gibbs phenomenon, commonly associated with discontinuities in images [27]. However, the relatively weak correlation and small values indicate that this effect is not prominent. The close similarity of the influence patterns between all types of wall indicates the independency of wall types. The slight dissimilarity in the influence patterns between the two wall types of the small vessels (figure 6-6C – influence from 100 and 200 HU lumen value) was caused by the difficulty to correctly segment the boundary of the small (approximately 2 pixels diameter) and low attenuation lumina.

The proposed correction algorithm managed to correct for the lumen contrast-enhancement influence on the most affected wall region, which is within a 2-pixel radius from the lumen border, reducing the median difference of 45 HU to a median difference of 4 HU, with reference to non contrast-enhanced vessel. When the whole wall region was measured, the median difference decreased from 10 HU to 2 HU.

A limitation of the study is that the HU values of the vessel wall (either the normal or the plaque-infested wall) do not specifically refer to any of the published plaque-specific HU values. The sheer amount of variations in the reported HU values makes a single correct selection of a particular plaque type impossible. However this limitation would not interfere with the result as has been shown in this study that the pattern of the lumen contrast-enhancement influence is independent to the wall types. The only variables that determined the pattern are the mean lumen HU-values and the spatial resolution of the CT system.

Another shortcoming is the fact that the coronary phantoms were scanned stationary and thus, the effect of coronary motion was not taken into account in this study. Future studies should be conducted to validate our correction algorithm using moving phantoms. However, the current correction algorithm could already be applied to other types of vessels where cardiac motion plays no role such as the carotids or peripheral vessels.

Conclusion

Lumen contrast-enhancement influence on the vessel wall can be defined by an exponential approximation, allowing correction of the CT density of the vessel wall closest to the lumen. After this correction, a more accurate determination of the composition of the vessel wall plaques can be made.

References

- [1] Heron MP, Smith BL. Deaths: leading causes for 2003. *Natl Vital Stat Rep* 2007; 55:1-92
- [2] Korosoglou G, Mueller D, Lehrke S, et al. Quantitative assessment of stenosis severity and atherosclerotic plaque composition using 256-slice computed tomography. *Eur Radiol* 2010; 20:1841-50
- [3] Leber AW, Johnson T, Becker A, et al. Diagnostic accuracy of dual-source multislice CT-coronary angiography in patients with an intermediate pretest likelihood for coronary artery disease. *Eur Heart J* 2007; 28:2354-60
- [4] Agatston AS, Janowitz WR, Hildner FJ, et al. Quantification of coronary artery calcium using ultrafast computed tomography. *J Am Coll Cardiol* 1990; 15:827-32
- [5] Oudkerk M, Stillman AE, Halliburton SS, et al. Coronary artery calcium screening: current status and recommendations from the European Society of Cardiac Radiology and North American Society for Cardiovascular Imaging. *Int J Cardiovasc Imaging* 2008; 24:645-71
- [6] Oudkerk M, Stillman AE, Halliburton SS, et al. Coronary artery calcium screening: current status and recommendations from the European Society of Cardiac Radiology and North American Society for Cardiovascular Imaging. *Eur Radiol* 2008; 18:2785-807
- [7] Virmani R, Burke AP, Farb A, Kolodgie FD. Pathology of the vulnerable plaque. *J Am Coll Cardiol* 2006; 47:13-8
- [8] Brodoefel H, Reimann A, Heuschmid M, et al. Characterization of coronary atherosclerosis by dual-source computed tomography and HU-based color mapping: a pilot study. *Eur Radiol* 2008; 18:2466-74
- [9] Leber AW, Knez A, Becker A, et al. Accuracy of multidetector spiral computed tomography in identifying and differentiating the composition of coronary atherosclerotic plaques A comparative study with intracoronary ultrasound. *J Am Coll Cardiol* 2004; 43:1241-7
- [10] Motoyama S, Kondo T, Anno H, et al. Atherosclerotic Plaque Characterization by 0.5-mm-Slice Multislice Computed Tomographic Imaging: Comparison With Intravascular Ultrasound. *Circ J* 2007; 71:363-6
- [11] Schroeder S, Kopp AF, Baumbach A, et al. Noninvasive detection and evaluation of atherosclerotic coronary plaques with multislice computed tomography. *J Am Coll Cardiol* 2001; 37:1430-5
- [12] Cademartiri F, Mollet NR, Runza G, et al. Influence of intracoronary attenuation on coronary plaque measurements using multislice computed tomography: observations in an ex vivo model of coronary computed tomography angiography. *Eur Radiol* 2005; 15:1426-31

- [13] Ferencik M, Chan RC, Achenbach S, et al. Arterial wall imaging: evaluation with 16-section multidetector CT in blood vessel phantoms and ex vivo coronary arteries. *Radiology* 2006; 240:708-16
- [14] Halliburton SS, Schoenhagen P, Nair A, et al. Contrast enhancement of coronary atherosclerotic plaque: a high-resolution, multidetector-row computed tomography study of pressure-perfused, human ex-vivo coronary arteries. *Coron Artery Dis* 2006; 17:553-60
- [15] Horiguchi J, Fujioka C, Kiguchi M, et al. Soft and intermediate plaques in coronary arteries: how accurately can we measure CT attenuation using 64-MDCT? *Am J Roentgenol* 2007; 189:981-8
- [16] Suzuki S, Furui S, Kuwahara S, et al. Accuracy of attenuation measurement of vascular wall in vitro on computed tomography angiography: Effect of wall thickness, density of contrast medium, and measurement point. *Invest Radiol* 2006; 41:510-5
- [17] Kristanto W, van Ooijen P, Groen JM, Vliegenthart R, Oudkerk M Non-calcified coronary atherosclerotic plaque visualization on CT part 1: effects of contrast-enhancement and lipid-content fractions. (2011):
- [18] Kristanto W, van Ooijen PM, Dijkers R, et al. Quantitative image analysis for the detection of motion artefacts in coronary artery computed tomography. *Int J Cardiovasc Imaging* 2010; 26:77-87
- [19] Brodoefel H, Burgstahler C, Sabir A, et al. Coronary Plaque Quantification by Voxel Analysis: Dual-Source MDCT Angiography Versus Intravascular Sonography. *Am J Roentgenol* 2009; 192:84-9
- [20] Nasu K, Tsuchikane E, Katoh O, et al. Accuracy of in vivo coronary plaque morphology assessment: a validation study of in vivo virtual histology compared with in vitro histopathology. *J Am Coll Cardiol* 2006; 47:2405-12
- [21] Nishimura RA, Edwards WD, Warnes CA, et al. Intravascular ultrasound imaging: in vitro validation and pathologic correlation. *J Am Coll Cardiol* 1990; 16:145-54
- [22] Kitagawa T, Yamamoto H, Ohhashi N, et al. Comprehensive evaluation of noncalcified coronary plaque characteristics detected using 64-slice computed tomography in patients with proven or suspected coronary artery disease. *Am Heart J* 2007; 154:1191-8
- [23] Nikolaou K, Becker CR, Muders M, et al. Multidetector-row computed tomography and magnetic resonance imaging of atherosclerotic lesions in human ex vivo coronary arteries. *Atherosclerosis* 2004; 174:243-52
- [24] Sun J, Zhang Z, Lu B, et al. Identification and quantification of coronary atherosclerotic plaques: a comparison of 64-MDCT and intravascular ultrasound. *Am J Roentgenol* 2008; 190:748-54

- [25] Achenbach S, Boehmer K, Pflederer T, et al. Influence of Slice Thickness and Reconstruction Kernel on the CT Attenuation of Coronary Atherosclerotic Plaque. *J Cardiovasc Comput Tomogr* 2010; 4:110-5
- [26] Cademartiri F, La Grutta L, Runza G, et al. Influence of convolution filtering on coronary plaque attenuation values: observations in an ex vivo model of multislice computed tomography coronary angiography. *Eur Radiol* 2007; 17:1842-9
- [27] Zeng GL, Allred RJ. Partitioned Image Filtering for Reduction of the Gibbs Phenomenon. *Journal of nuclear medicine technology* 2009; 37:96-100
- [28] Shimamoto R, Suzuki J, Yamazaki T, et al. A new method for measuring coronary artery diameters with CT spatial profile curves. *Radiography* 2007; 13:44-50
- [29] Xu C, Prince JL. Snakes, Shapes, and Gradient Vector Flow. *IEEE Trans on Image Process* 1998; 7:359-69

Chapter 7

Summary

Non-invasive coronary imaging has the potential to replace invasive coronary angiography as the common technique for detection of coronary heart disease, if the key-morphology to diagnose coronary artery disease (CAD) can be determined by CT acquisition, processing, and postprocessing techniques. Both the vessel' width (lumen opening) and wall morphology are important characteristics in disease detection. In chapter 1, an overview is given on the clinical representation and significance of CAD. Accurate and reliable visualization and quantifications are needed to determine the proper treatment of CAD. Two major characteristics determining the reliability of a coronary artery are its lumen opening and its wall morphology. Early imaging modalities, such as x-ray angiography and intravascular ultrasound, provide a good assessment of these features. However, they also experience several limitations, most notably due to their invasiveness. In chapter 1, the steady rise of multi detector-row computed tomography (MDCT) to be the preferred non-invasive modality to assess CAD is discussed. With MDCT, the whole coronary tree and its lumen can be adequately visualized with reported specificity for determination of obstructive coronary disease of up to 100%. Also, an MDCT-based quantification of the calcified portion of the coronary wall has been so reliable that it is regarded as a strong predictor of coronary events. Despite of these positive reports, MDCT still has its limitations in visualizing the fast moving coronaries and small components of coronary atherosclerotic plaque. The aim of the research described in this thesis is to evaluate and improve the determination of coronary disease using MDCT with focus on stenotic lesions of the lumen and small calcified and soft plaques in the coronary artery wall.

In Chapter 2, the ability to visualize the coronary lumen opening with MDCT is discussed, especially the effect of motion artefacts and how these could be recognized in post-processing. Despite the already high temporal resolution of the latest generation of MDCT scanners, the desired temporal resolution to image small fast moving objects such as coronary arteries always artefact free can not be achieved yet. A systematic investigation on the effect of motion artefacts on coronary visualization was performed by scanning an anthropomorphic moving heart phantom in a 64-row MDCT (64-MDCT) scanner and a dual-source CT (DSCT) scanner. A 64-MDCT scanner has a gantry rotation speed of 0.33 ms / rotation. A DSCT scanner has the same gantry rotation speed but twice the temporal resolution due to the presence of two x-ray source-detector pairs rotating simultaneously. The results of the study showed that, the higher temporal resolution of DSCT indeed provides a better image quality when compared to 64-MDCT. Further analysis of the effect of motion artefacts on coronary stenosis evaluation showed that up to 30% of the detected stenoses can be artificial, caused by motion artefacts. A quantification method was developed base on these findings, which contributes to the diagnostic accuracy by ruling out these false diagnoses, thus improving the diagnostic value of a qualitative analysis.

The early onset of calcification in a coronary plaque may indicate early progression of coronary disease and increased coronary risk in a patient. The presence of

very small calcified plaques (microcalcifications) in the thin fibrous cap covering a large atheromatous plaque was hypothesized to be able to destabilize the cap to the point of rupture-prone, potentially exposing the thrombogenic material underneath to the blood. In Chapter 3, the ability to visualize these very small calcified plaques (microcalcifications) with MDCT is discussed. MDCT is known to be highly sensitive for the detection of coronary calcification because of the distinctively high attenuation values of calcified plaques. Furthermore, calcium scoring, a quantification of coronary calcification as detected by MDCT, is proven to be a strong predictor of future coronary events. However, an inherent limitation of MDCT, namely the limited spatial resolution of up to 0.4 mm, still hinders the visualization of microcalcifications. It was shown using a software simulation that the smallest calcification that can be visualized by a typical 64-MDCT scanner has a diameter of approximately 200 μm . This indicates that the early onset of calcification in coronary plaque will go undetected when using current clinical CT systems; and a zero calcium score can not absolutely exclude the presence of coronary calcification.

In Chapters 4 to 6, the ability to visualize non-calcified plaques with MDCT is discussed. Several studies have reported the ability to characterize non-calcified plaques based on their Hounsfield Unit (HU) value with MDCT, providing HU-criteria or even HU cut-off values to distinguish between lipid-rich and fibrous plaques. However, there appears to be no concordance between the different reports, most probably since the small size of the plaques (relative to the resolution of the scan) cause partial volume effects.

In Chapter 4, all published HU-based criteria to characterize non-calcified plaque into fibrous and lipid-rich plaques were systematically analyzed. Considerable variations in the published HU criteria were found. However, there were specific relationships found between the HU-criteria and the reporting studies' characteristics, in terms of: examination type (in-vivo versus ex-vivo study), vessel type (coronary versus other artery), CT-system brand, detector-rows, voltage-setting, and collimation-width. In order to investigate these relationships more deeply, the HU-criteria were hierarchically classified based on these characteristics and visualized in diagrams. As a result, 21 and 22 distinct HU-criteria were obtained for lipid-rich and fibrous plaques, respectively. Significant differences were found between most of these hierarchically classified HU-criteria, indicating limited applicability when HU-criteria of certain study characteristics are used for studies with non-matching characteristics. To overcome this problem, the diagrams that are presented, can be consulted in a clinical setting to find the closest suitable HU-criteria for one specific situation by matching the characteristics in the diagrams as much as possible to the local situation.

In Chapter 5, this topic is further discussed by investigating the factors that influence non-calcified plaque visualization on a coronary MDCT angiography dataset. The limitation in spatial resolution of MDCT has made it difficult to identify a single component of a non-calcified plaque. The partial volume effect, either from different plaque components or from the lumen contrast-enhancement, strongly affects non-calcified

plaque visualization and hence, its attenuation value. Using a software simulation which incorporates realistic scanning parameters, it was shown that plaque's attenuation value and percentage lipid-rich content is linearly correlated. The linear correlation between the plaque lipid-rich content and its HU-value indicates the possibility to characterize the plaque lipid-rich content based on its HU value instead of strict depiction of individual components. However, inherent limitations still severely hinder the applicability of this method. Lumen contrast-enhancement was found to highly influence the plaque's attenuation value, following a specific exponential pattern until 2-pixel radius from the lumen border. This pattern is dependent only on the lumen contrast-enhancement level and the distance from the lumen border, and not on stenosis grade, plaque content and modality/spatial resolution. This finding indicates the possibility to construct an algorithm to correct for lumen contrast-enhancement influence.

In Chapter 6, the validation and application of the contrast-enhancement influence as described in chapter 5 were studied using a physical experimental setup. This setup involved a hardware coronary vessel phantom, with a hollow lumen and plaque-infested wall. The linear correlation between lumen contrast-enhancement and plaque attenuation value, and the specific exponential patterns of lumen contrast-enhancement were confirmed. Based on the specific influence patterns, a generalized correction algorithm was constructed. Early validation of this correction algorithm showed a promising reduction of lumen contrast-enhancement influence from a median plaque HU-value deviation from the non-contrast-enhanced reference of 45 HU to 4 HU. After this correction, a more accurate determination of the composition of the vessel wall plaques could be made.

In conclusion, MDCT scanning, in combination with advanced post-processing techniques, is a powerful tool to non-invasively investigate coronary artery disease but still leaves room for improvement. The studies performed in this thesis with hardware and software phantoms identified some drawbacks of MDCT in assessing coronary artery disease. Some drawbacks are yet to be solved due to inherent limitations of the current MDCT technology (*i.e.* the spatial resolution limitation to visualize microcalcifications), others are to be avoided by exercising caution when conducting the examinations (*i.e.* the false artificial stenosis induced by motion artefacts). However, it is shown that some of the artefacts and interpretation problems can be reduced and managed using advanced post-processing techniques such as the lumen contrast-enhancement correction. The advance in knowledge provided by these findings will help to improve coronary artery disease determination using MDCT.

Chapter 8

Samenvatting

De huidige, invasieve, standaardtechniek voor het afbeelden van de kransslagaderen, de coronair angiografie, zou mogelijkerwijs vervangen kunnen worden door niet-invasieve CT-acquisitie, verwerkings- en bewerkingstechnieken, mits hiermee de morfologie van coronaire hartziekten goed kan worden vastgelegd. Belangrijke kenmerken hierbij zijn de vaatwijdte (het lumen) en de vaatwandsamenstelling. In hoofdstuk 1 wordt een overzicht gegeven van de klinische presentatie en significantie van coronaire hartziekten (Coronary Artery Disease – CAD). Voor het bepalen van de juiste behandeling van CAD zijn accurate en betrouwbare visualisatie en kwantificering essentieel.

De twee belangrijkste karakteristieken, die de betrouwbaarheid van een kransslagader bepalen, zijn de opening van het lumen en de morfologie van de vaatwand. Beeldvormende technieken als de coronair angiografie en intravasculaire ultrasound bieden de mogelijkheid om deze karakteristieken te visualiseren en te evalueren. Deze technieken hebben echter ook een aantal tekortkomingen, waarvan de belangrijkste is dat het onderzoek invasief is. In hoofdstuk 1 wordt de opkomst van Multi Detector Computer Tomografie (MDCT) als voorkeurstechneik voor het niet-invasief beoordelen van CAD beschreven. Met behulp van MDCT kunnen zowel het lumen als de vaatwand van de gehele kransslagaderen gevisualiseerd worden met een in de literatuur beschreven specificiteit voor het vaststellen van obstructieve vernauwing oplopend tot 100%. Daarnaast is het detecteren en meten van calcificaties in de vaatwand met MDCT dusdanig betrouwbaar dat het beschouwd wordt als een sterke voorspeller van hartfalen. Ondanks deze positieve ontwikkelingen heeft MDCT nog steeds tekortkomingen bij het in beeld brengen van de snel bewegende kransslagaderen en de zeer kleine componenten van atherosclerotische plaques. In dit proefschrift wordt naar oplossingen gezocht voor de huidige beperkingen van MDCT bij de identificatie en kwantificering van het afbeelden van de kransslagaderen. Hierbij wordt de nadruk gelegd op de visualisatie van vernauwingen van het lumen en kleine kalk- en soft-plaques in de vaatwand.

In hoofdstuk 2 wordt het in beeld brengen van de lumenopening van de kransslagaderen met behulp van MDCT beschreven en dan met name het effect van bewegingsartefacten en hoe deze kunnen worden onderkend door middel van nabewerking (post-processing) van de beelden. Ondanks de hoge temporele resolutie van de meest recente generatie MDCT scanners zijn deze nog niet in staat om bij elke patiënt de snel bewegende kransslagaderen zonder artefacten in beeld te brengen. Gebruik makend van een antropomorfisch bewegend hartfantoom is systematisch onderzoek gedaan naar het effect van deze bewegingsartefacten op de visualisatie van de kransslagaderen. Hierbij is gebruik gemaakt van een 64-rij MDCT (64-MDCT) met een rotatie snelheid van 0.33 ms per rotatie en een dual-source CT (DSCT) met dezelfde rotatiesnelheid maar dubbele temporele resolutie door het gelijktijdig gebruik van twee röntgenbron en -detectorparen. De resultaten tonen aan dat de hogere temporele resolutie van de DSCT inderdaad leidt tot een betere beeldkwaliteit in vergelijking met 64-MDCT. Verdere analyse van de effecten van bewegingsartefacten op de beoordeling van de kransslagaderen toonde aan dat tot 30% van

de gevonden vernauwingen kunstmatig kan zijn, veroorzaakt door bewegingsartefacten. Op basis van deze bevindingen is een kwantificeringsmethode ontwikkeld die, door het detecteren van deze kunstmatige vernauwingen, een bijdrage levert aan de diagnostische waarde van een kwantitatieve beoordeling.

Het vroege ontstaan van calcificaties in een plaque in de kransslagaderen kan een aanwijzing zijn voor progressie van vaatziekten en daarmee een verhoogd risico hierop geven voor de patiënt. Er is een vermoeden dat de aanwezigheid van zeer kleine calcificaties (micro-calcificaties) in het dunne fibreuze kapsel, dat over een grote atheromateuse plaque ligt, dit vlies destabiliseert tot het scheurt (ruptuur), waardoor het thrombogene materiaal van de plaque in contact kan komen met het bloed. In hoofdstuk 3 wordt de mogelijkheid besproken om deze zeer kleine calcificaties (micro-calcificaties) te bekijken met MDCT. Het is bekend dat de detectie van calcificaties in de kransslagaderen zeer goed uitgevoerd kan worden met behulp van MDCT door de onderscheidende hoge röntgen absorptie waarde (in HU) van gecalcificeerde plaques. Tevens is de kalkscore berekend op basis van MDCT een bewezen sterke voorspeller voor toekomstig hartfalen. Een inherente tekortkoming van MDCT die de visualisatiemogelijkheden van micro-calcificaties beperkt is echter de beperkte spatiële (ruimtelijke) resolutie van maximaal 0.4mm. Door een softwaresimulatie is aangetoond dat de kleinste calcificaties, die zichtbaar gemaakt kunnen worden met een typische 64-MDCT scanner, een diameter van ongeveer 200 μm hebben. Dit is een aanwijzing dat het vroege ontstaan van calcificaties met de huidige generatie klinische CT systemen niet zal worden ontdekt en dat een kalkscore van nul de aanwezigheid van kalk in de vaatwand niet absoluut kan uitsluiten.

In de hoofdstukken 4 tot en met 6 worden de mogelijkheden van MDCT voor het visualiseren van zachte plaques (zonder kalk) behandeld. In meerdere studies is de mogelijkheid beschreven om niet gecalcificeerde plaques met MDCT te karakteriseren op basis van hun Hounsfield Unit (HU). Deze studies stellen HU-criteria of zelfs HU afkapwaarden voor om onderscheid te maken tussen lipide (vet) rijke en fibrotische (bindweefsel-achtige) plaques. Er lijkt echter geen overeenstemming te zijn tussen de resultaten van de verschillende publicaties, waarschijnlijk omdat de relatief kleine omvang van de plaques ten opzichte van de spatiële resolutie van de scan partial volume effects veroorzaakt.

Hoofdstuk 4 beschrijft een systematische analyse van alle gepubliceerde HU gebaseerde criteria voor de karakterisering van zachte plaques in lipiderijke en fibrotische plaques. Er zijn aanzienlijke verschillen gevonden in de gepubliceerde criteria. Wel zijn er specifieke relaties gevonden tussen de HU criteria en de karakteristieken van de bijbehorende studies op basis van: soort onderzoek (in-vivo versus ex-vivo), vaatype (kransslagaders versus andere vaten), merk van het CT system, aantal detector rijen, instelling van het voltage, en breedte van de collimatie. Om deze relaties beter te onderzoeken zijn de HU criteria hiërarchisch geëvalueerd op basis van deze karakteristieken en samengevat in een aantal diagrammen. Dit leidt voor lipiderijke plaques

tot 21 en voor fibrotische plaques 22 afzonderlijke HU criteria. Na verdere analyse bleek dat de toepassing van HU gebaseerde criteria beperkt is, daar de meeste van deze hiërarchisch geclassificeerde HU criteria significant verschilden. Hierdoor is gebruik van een willekeurige set van HU criteria niet geschikt voor studies, die uitgevoerd worden met andere karakteristieken dan die gebruikt om de HU criteria te bepalen. Om dit probleem te voorkomen is het mogelijk om uit de gepresenteerde diagrammen die HU criteria te kiezen die gebaseerd zijn op een situatie waarin de genoemde karakteristieken zo goed mogelijk overeen komen met de eigen klinische situatie.

Dit onderwerp wordt verder behandeld in hoofdstuk 5 door de factoren te onderzoeken, die de visualisatie van niet-gecalcificeerde plaques met behulp van MDCT beïnvloeden. De identificatie van de verschillende plaque componenten wordt bemoeilijkt door de beperkingen in spatiële resolutie van MDCT. Op basis van het partial volume effect wordt de gemeten röntgen absorptie waarde sterk beïnvloed door de omgeving (verschillende plaque componenten of contrastmiddel in het lumen). Op basis van een softwaresimulatie met realistische scan eigenschappen is aangetoond dat de correlatie tussen de röntgen absorptie waarde van een plaque en het percentage lipiderijke componenten lineair is. Deze lineaire correlatie tussen de lipiderijke component en de HU waarde van de gehele plaque biedt mogelijkheden om de lipiderijke component te bepalen op basis van de HU waarde in plaats van een strikte scheiding van individuele componenten. Praktische toepassing van deze methode wordt echter bemoeilijkt door een aantal fundamentele tekortkomingen. De röntgen absorptie waarde van een plaque wordt sterk beïnvloed door het contrastmiddel dat zich in het lumen bevindt op basis van een exponentieel patroon tot een 2-pixel afstand van de lumen begrenzing. Dit patroon is alleen afhankelijk van het niveau van contrastaankleuring van het lumen en de afstand tot de lumenbegrenzing en niet van de mate van de vernauwing, samenstelling van de plaque of modaliteit/spatiële resolutie. Op basis van deze bevinding is het mogelijk om een algoritme te ontwikkelen dat corrigeert voor de invloed van de contrastaankleuring.

In hoofdstuk 6 zijn de invloeden en effecten van contrastaankleuring, die beschreven staan in hoofdstuk 5, gevalideerd en toegepast binnen een fysieke experimentele opstelling. Deze opstelling bestond uit een fysiek kransslagader fantoom met een hol lumen en plaques in de vaatwand. De lineaire correlatie tussen lumen contrastaankleuring en de röntgen absorptie waarde van de plaques, die ook met de softwaresimulatie waren gevonden, zijn bevestigd in deze opstelling. Vervolgens is op basis van de gevonden patronen een algemeen correctie-algoritme ontwikkeld. Een eerste validatie van dit correctie-algoritme liet een veelbelovende afname van de invloed van de contrastaankleuring zien. De mediaan van de afwijkingen van de HU-waarde van de plaque ten opzicht van de werkelijke waarde zonder contrast nam na correctie af van 45HU naar 4HU. Op basis van deze resultaten is een nauwkeurigere beoordeling van de plaquesamenstelling in de kransslagaderen mogelijk.

Concluderend kan worden vastgesteld dat, in combinatie met geavanceerde beeldbewerkingstechnieken, MDCT een krachtig middel is voor het niet-invasief onderzoeken van de kransslagaderen maar dat er nog ruimte voor verbetering is. De in dit proefschrift op basis van software en hardware fantomen beschreven onderzoeken tonen een aantal van de tekortkomingen van MDCT aan. Enige hiervan moeten opgelost kunnen worden door de continue verbetering van de MDCT technologie (bijv. de beperking in de visualisatie van microcalcificaties door de beperkte spatiële resolutie), of door het zorgvuldig werken bij het uitvoeren van het onderzoek (bijv. introductie van kunstmatige stenoses veroorzaakt door bewegingsartefacten). Het is echter aangetoond dat een aantal van de artefacten en interpretatieproblemen verminderd en geregeld kan worden door geavanceerde beeldbewerkingstechnieken zoals de lumen contrastaankleuringcorrectie en de hiërarchische classificatie van HU criteria. De kennisvermeerdering, die door deze bevindingen is verkregen, zal bijdragen tot verbetering van de vroegtijdige, niet-invasieve, opsporing van coronaire hartziekten met behulp van MDCT.

Chapter 9

Acknowledgement

There are many people whom I want to acknowledge on their contribution, both directly and indirectly, to the success of finishing this PhD thesis. Without them, it certainly would have been impossible for me to reach the current state of my PhD.

The first person that I want to express my gratitude to is my promotor, Prof. Oudkerk. Thank you for the opportunity given to me to perform research in the Department of Radiology and also for all the arrangements that have made the finishing of this PhD training possible. The second person that I want to express my gratitude to is my co-promotor, Peter van Ooijen. From the start of my PhD project onwards, and even before that, during my master thesis project, you have been my most important mentor. You stood by me during my up and mostly during my down moments. You have been my inspiration, both in my career and my life, and I suspect that you will always be. I really enjoyed working with you and hope there will come a chance in the future to do so again. The next person that is indispensable is Stella Noach. With your smile and wisdom, you patiently guide us, the foreign students. You call yourself a mother goose and I say you rightfully earn that title. Thank you for all the advices.

Thank you for all my co-authors: Marcel, Rozemarijn, Martine, Jaap, Prof. Zijlstra, and Riksta. Your input in my manuscripts has really been useful to improve their scientific content. Especially Riksta, I still remember the good time we had during our trip to Siemens headquarter, along with those coronaries. Thank you to dr. Bart de Smet for all the discussion regarding IVUS. Thank you Prof. Anne Paans for the permission to use the MicroCT, and Johan de Jong for the assistance during the experiments. Thank you to dr. Wilfred den Dunnen for providing the specimens and the expertise to analyze them.

The next two persons that I would like to express my gratitude to are my two great paranymphs, Astri and Volkan. Thank you for the arrangements during the preparation of the defense day and the support along the way. For my G2 colleagues, Hildebrand, Gonda, Yingru, Ying, Dongming, Xie, Anne, Daniel, Marjolein, Mienke, Alain, Petra, Martijn, Andre, Yota, Pandji, thank you for the good times when I was working there. I really enjoyed visiting the conferences with such cool colleagues as you are. Special thanks to Wim for accompanying me during the late night scanning on the dual-source CT and all the technical enlightments that you have given.

This acknowledgement would not be complete without mentioning my Indonesian friends and arguably my Indonesian family in Groningen. *Pak* Tri and family, *Pak* Ketut, Poppy-Henk, Buana-Rina, Asaf-Tresna, Henky-Dita, Bima, Mahesa, Pandoe, the 7 penyamun Groningen, Fesia-Vincent, thank you for making my first days in Groningen felt like I was among family. To *Mbak* Tina and family, Santi, Christin, *Mbak* Tita, CB, *Kak* Ika, the Widoyono family, thank you for being such good friends. And to many more persons who,, if I would write all their names here, would require me to write another book just to say thanks to them.

Special acknowledgement I would like to give to my family. Thank you to my mother for her caring and unconditional support since I was born until now. Thank you to

my brother, for giving me wise advices and being my role model. To my late father, thank you for teaching me to be the man I am now. A special thank you to my wife, Yuli, for her never ending trust, support, caring and love. With you, everything seems to fall in the right place. I love you so much, dear. And to my beloved son, Joshua, who in his own way, always managed to cheer me up during those tough time. I love you all.

Last, but certainly not least, thank you Jesus.

Chapter 10

Curriculum vitae

Wisnumurti Kristanto was born on May 5th, 1979 in Surabaya, Indonesia. There he spent his youth with his mother, father, and older brother until he finished high school. He came to Bandung, Indonesia in 1997 to do his bachelor study at Institut Teknologi Bandung, majoring in Electrical Engineering with sub-major in Biomedical Engineering. He continued his study in 2002 at the same institution, pursuing a master degree, also in the same major and sub-major. At the same time, he worked also as a system engineer for almost a year at a start-up medical software company, Mitra Medika, in Bandung, Indonesia. In 2004, he went to perform his master thesis project at University of Groningen, Groningen, The Netherlands, specifically at the Department of Radiology, University Medical Center Groningen, Groningen, The Netherlands. In 2005, he received double master degrees from both institutions, a Master of Engineering from Insitut Teknologi Bandung and a Master of Science from University of Groningen.

In 2006, he started his PhD training at Faculty of Medical Sciences, University of Groningen, specifically at the Department of Radiology, University Medical Center Groningen, which resulted in this thesis. During his PhD training, he managed to visit multiple international institutions, i.e.: Siemens Medical System's headquarter in Erlangen, Germany; Mevis Medical Solutions AG's headquarter in Bremen, Germany; University of Tuebingen, Tuebingen, Germany; and Technical University of Eindhoven, Eindhoven, The Netherlands. He also managed to present his research results in multiple international conferences, i.e.: European Society of Cardiac Radiology (ESCR), European Congress of Radiology (ECR), Radiological Society of North America (RSNA) and Computer Aided Radiology Society (CARS); and a national conference, i.e.: the Dutch Biomedical Engineering.

In 2012, he continued to pursue his passion in cardiovascular image analysis field in a new position as a software developer at Pie Medical Imaging BV, Maastricht, The Netherlands, a company which produces cardiovascular image analysis software.

Chapter 11

List of publications

List of publications

- [1] Kristanto W, van Ooijen PMA, The B, Duifhuis H, Mengko TR, Oudkerk M. Design and Implementation of Gradient Vector Flow Snake to Detect a Reference Object in Pelvic X-Rays for Preoperative Total Hip Arthroplasty Planning Application. *J Digit Imaging* 2007; 20:373-80
- [2] Dijkers R, Greuter MJ, Kristanto W, van Ooijen PM, Sijens PE, Willems TP, Oudkerk M. Assessment of image quality of 64-row Dual Source versus Single Source CT coronary angiography on heart rate: A phantom study. *Eur J Radiol* 2008; 70:61-8
- [3] Edens MA, van Ooijen PMA, Post WJ, Haagmans MJF, Kristanto W, Sijens PE, van der Jagt EJ, Stolk RP. Ultrasonography to Quantify Hepatic Fat Content: Validation by 1H Magnetic Resonance Spectroscopy. *Obesity* 2009; 17:2239-44
- [4] van Ooijen PMA, Kristanto W, Jonge GJ, Kuehnel C, Hennemuth A, Boskamp T, Groen JM, Broekema A. Multi-Dimensional Computed Cardiac Visualization. *Coronary Radiology* 2nd edition. Berlin Heidelberg: Springer-Verlag. 2009: pp 297-338
- [5] van Ooijen PMA, de Jonge GJ, Kristanto W, Handayani A, Tuncay V, Oudkerk M. Optimal postprocessing of images following cardiac examination using CT and MRI. *Imaging Med* 2010; 2:459-74
- [6] Kristanto W, van Ooijen PM, Dijkers R, Greuter MJ, Zijlstra F, Oudkerk M. Quantitative image analysis for the detection of motion artefacts in coronary artery computed tomography. *Int J Cardiovasc Imaging* 2010; 26:77-87
- [7] Kristanto W, Ooijen PMA, Groen JM, Vliegenthart R, Oudkerk M. Small calcified coronary atherosclerotic plaque simulation model: minimal size and attenuation detectable by 64-MDCT and MicroCT. *Int J Cardiovasc Imaging* 2011; 28: 843-853
- [8] van Abbema JK, van der Schaaf A, Kristanto W, Groen JM, Greuter MJ. Feasibility and accuracy of tissue characterization with dual source computed tomography. *Phys Med* 2012; 28:25-32